Synthesis, structure and properties of zirconium-based binary alloy thin films

DISSERTATION

zur Erlangung des Grades des
Doktors der Ingenieurwissenschaften
der Naturwissenschaftlich-
Technischen Fakultät der Universität
des Saarlandes

UNIVERSITÄT DES SAARLANDES

Von
Alejandro Borroto Ramírez
Saarbrücken / Nancy – 2019

Tag des Kolloquiums: 07. Juni 2019

Dekan: Prof. Dr. Guido Kickelbick

Berichterstatter: Prof. Dr.-Ing. Frank MÜCKLICH

Prof. Dr.-Ing. Dirk BÄHRE

Prof. Dr. David HORWAT

Vorsitz: Prof. Dr. Grégory ABADIAS

Weitere Mitglieder: Prof. Dr. Albano CAVALEIRO

Dr. Anne-Lise THOMANN

Prof. Dr. Zoe BARBER

Dr. Stéphanie BRUYERE

Abstract

In this thesis, we demonstrate that original nanostructures can be obtained by working around the crystalline-to-amorphous transition in sputter-deposited thin films. In particular, we study two systems, Zr-Mo and Zr-W, in which such transition occurs. By decreasing the Mo content in the Zr-Mo system, a structural transition from a nanocrystalline solid solution of Zr in the bcc lattice of Mo to an amorphous structure can be achieved around 60 at% Mo. The films obtained present high hardness *H*, low Young's modulus *E* and, consequently, high *H/E* ratio compared with bulk Zr and Mo. Furthermore, we demonstrate that a self-separation of the nanocrystalline and the amorphous phases occurs at the composition intermediate to those necessary to form single-phased amorphous and nanocrystalline films. The particular geometry in which the nanocrystalline phase grows in competition with the amorphous phase is exploited to achieve a thickness-controlled surface morphology which allows to tune the film reflectance. A model was developed to describe the kinetics of the competitive growth between the nanocrystalline and the amorphous phases. Furthermore, it allows to construct a thickness-composition phase diagram evidencing that the nanocrystalline/amorphous competitive growth is easily hidden experimentally. Finally, we demonstrate that massive monocrystalline grains with lateral size larger than 1 μm can be obtained by working at low Ar pressure if the composition of the films approaches to the edge of the amorphous transition. Our results suggest that the phenomena reported here for Zr-Mo and Zr-W can be extended to other systems.

Zusammenfassung

In dieser Arbeit zeigen wir, dass originelle Nanostrukturen durch Umgehen des Übergangs von kristallin zu amorph in aufgesputterten dünnen Schichten erhalten werden können. Insbesondere untersuchen wir zwei Systeme in denen ein solcher Übergang stattfindet, Zr-Mo und Zr-W. Durch Verringerung des Mo-Gehalts im Zr-Mo-System kann ein struktureller Übergang von einer nanokristallinen festen Lösung von Zr im bcc-Gitter von Mo zu einer amorphen Struktur um 60 Atom-% Mo erreicht werden. Die erhaltenen Filme zeigen eine hohe Härte H, einen niedrigen Elastizitätsmodul E und folglich ein hohes H/E-Verhältnis im Vergleich zu massiven Zr und Mo. Des Weiteren zeigen wir, dass eine Selbsttrennung der nanokristallinen und der amorphen Phase bei einer bestimmten Zusammensetzung auftritt. Die besondere Geometrie, in der die nanokristalline Phase im Wettbewerb mit der amorphen Phase wächst, wird ausgenutzt, um eine dickengesteuerte Oberflächenmorphologie zu erreichen, die es erlaubt, die Filmreflexion einzustellen. Ein Modell wurde entwickelt, um die Kinetik des kompetitiven Wachstums zwischen der nanokristallinen und der amorphen Phase zu beschreiben. Schließlich zeigen wir, dass massive einkristalline Körner mit einer lateralen Größe von mehr als 1 µm bei niedrigem Ar-Druck bei einer Filmzusammensetzung am Rand des amorphen Übergangs erhalten werden können. Unsere Ergebnisse legen nahe, dass die hier beschriebenen Phänomene für Zr-Mo und Zr-W auf andere Systeme ausgedehnt werden können.

Résumé

Dans cette thèse, nous démontrons que des nanostructures originales peuvent être obtenues en travaillant autour de la transition cristallin/amorphe dans des films minces déposés par pulvérisation cathodique. En particulier, nous étudions deux systèmes, Zr-Mo et Zr-W, dans lesquels une telle transition se produit. Dans ce système, lorsque la teneur en Mo est réduite, une transition structurale d'une solution solide nanocristalline de Zr dans le réseau bbc de Mo à une structure amorphe peut être obtenue autour de 60 at % de Mo. Les films obtenus présentent une dureté H élevée, un faible module de Young E et, par conséquent, un ratio H/E élevé par rapport à celui de Zr et Mo. Par ailleurs, nous démontrons qu'une auto-séparation des phases nanocristalline et amorphe se produit à une composition spécifique. La géométrie particulière dans laquelle la phase nanocristalline se développe en concurrence avec la phase amorphe est exploitée pour contrôler la morphologie de surface et, par conséquent, la réflectance par l'intermédiaire de l'épaisseur. Un modèle a été développé pour décrire la cinétique de la croissance compétitive entre les phases nanocristalline et amorphe. De plus, cela permet de construire un diagramme de phase épaisseur-composition qui montre que la croissance compétitive nanocristalline/amorphe est facilement dissimulée expérimentalement. Finalement, nous démontrons que des grains monocristallins massifs de taille latérale supérieure à 1 µm peuvent être obtenus en travaillant à basse pression d'Ar si la composition des films se rapproche du bord de la transition amorphe. Nos résultats suggèrent que les phénomènes observés pour les systèmes Zr-Mo et Zr-W peuvent être étendus à d'autres systèmes.

Acknowledgements

A special thanks to *los meninos*, Alexis and Mariana for the funny moments we have spent together and those that remain to come. I like to thank Vitalis and Magali, for the nice Friday nights, and for their friendship.

I would like to thank my family for their support and specially my parents in law, second parents for me in these last years.

Specially, I would like to thank my parents, who always care for me, for they love and support throughout my life.

Finally, I would like to thank my wife, my life partner, my love, this thesis is dedicated to her.

Contents

Introduction

New nanostructured materials are highly sought from both fundamental and functional point of views. Among them, nanocrystalline and amorphous metallic alloys are interesting because they can exhibit improved properties compared to their microcrystalline counterpart. Within this class of materials, sputter-deposited Zr-based binary alloys are prone to form amorphous and nanocrystalline structures [1–4], which can be used as a way of improving the mechanical properties of the alloys. In particular, Zr-Mo alloys are promising candidates as hard metallic coatings due to the intrinsic high hardness of Mo [5] and the high cohesive energy of Mo and Zr [6] among the transition metals.

The vapor-to-solid transition occurring in sputter-deposited metallic alloys can prevent the crystallization in many systems. In consequence, a composition-driven transition from an amorphous to a crystalline structure is frequently observed in metallic alloys thin films obtained by sputtering. In particular, such a transition has been reported in sputter-deposited Zr-Mo [1] and Zr-W [3,7,8] thin films . However, its nature has not been addressed. For example, in the Zr-W system, it appears as a singularity in the optical properties of the films within the studied compositions and a similar situation has been observed in other systems. This suggests that a general process could be in action, detectable only with very precise variation of the chemical composition.

The aim of this thesis is to investigate the microstructure of Zr-based binary thin film alloys in order to control and modify their functional properties. We demonstrate that original nanostructures can be obtained by working around the crystalline-to-amorphous transition in sputter-deposited thin films. The manuscript is organized in six Chapters and a General conclusions section:

In Chapter 1 a short bibliographic review of the literature available on the Zr-Mo system is presented. We start by discussing the main features of the phase diagram of the Zr-Mo system, followed by a presentation of the properties and potential applications that have been explored

over the years in this system. In addition, the structural and mechanical properties of sputter-deposited Zr-W thin films, a system that complements the Zr-Mo system, are discussed.

In Chapter 2 technical and fundamental aspects of the growth and characterization techniques used throughout this thesis are described.

Chapter 3 provides a first assessment of the Zr-Mo system. Using a combinatorial approach, Zr-Mo thin films were synthesized in a wide composition range by co-sputtering zirconium and molybdenum targets. The films obtained exhibit improved mechanical properties compared with the bulk of Zr and Mo: high hardness (*H*) while keeping a Young's modulus (*E*) in the range of metals, high *H/E* ratio and low friction coefficient values. At the structural level, sputter-deposited Zr-Mo thin films exhibit a transition from X-ray amorphous to nanocrystalline structures at a composition around 60 at% Mo. Investigating the nature of this transition is the purpose of Chapters 4, 5 and 6.

In Chapter 4 a detailed study the amorphous-to-nanocrystalline structural transition (at approximately 60 at% Mo) in the Zr-Mo system is presented. It is demonstrated that a self-separation of a nanocrystalline and an amorphous phases occurs in sputter-deposited Zr-Mo thin films obtained at compositions intermediate to those necessary to form single-phased amorphous and nanocrystalline films. The possibility of achieving a thickness-controlled surface morphology in these films due to the competitive growth between the two phases enables tuning the film optical reflectance. It is shown that the self-separation of phases as presented here can be extended to other systems.

In Chapter 5 a model capable of describing the kinetics of the competitive growth phenomenon showed in Chapter 4 is developed. The model is applied to fit experimental data of the density of nanocrystalline nuclei and surface coverage in sputter-deposited Zr-W thin film alloys. Based on the outcomes of the proposed model, a schematic thickness-composition phase diagram is proposed which highlights that despite nanocrystalline/amorphous competitive growth occurs in a wide range of compositions, it is easily hidden experimentally.

In Chapter 6 the consequences of decreasing the working pressure (a parameter acting directly on the mobility of the adatoms) on the microstructure of Zr-Mo thin films around the amorphous-to-crystalline transition are investigated. First, it is shown that the geometrical

shape of the crystalline phase growing in competition with the amorphous one can be changed. Second, it is shown that massive monocrystalline grains with lateral size larger than 1 µm can be obtained near the crystalline-to-amorphous transition.

Finally, general conclusions, discussions and perspectives to the main findings of the thesis are given.

Chapter 1

Background on Zr-Mo and Zr-W systems

ABSTRACT: In this chapter, we present an overview of the state of the art of Zr-Mo alloys. In a first part, the basic structural features of Zr and Mo are described together with the phase diagram of the Zr-Mo system. In a second part, are presented the properties explored through the years, such as superconductivity, biocompatibility and mechanical properties, together with the potential application of these alloys. Finally, the structural and mechanical properties of Zr-W (a complementary system to Zr-Mo) are discussed.

Contents

1.1 Zr-Mo system

Zr and Mo are refractory metals with melting point values of 2128 and 2896 K, respectively. At room temperature, Zr crystallizes in the hexagonal close-packed (hcp) structure, α-Zr (space group: P6₃/mmc), with lattice parameters $a = b = 3.216$ Å and $c = 5.154$ Å (ICDD 04-015-6227). At 1136 K, it transforms to a body-centered cubic (bcc) crystal structure, β-Zr (space group: Im$\bar{3}$m), with lattice parameter $a = 3.568$ Å (ICDD 01-071-3958). The β-phase is retained until the melting point. On the other hand, at room temperature, Mo crystallize in the bcc structure (space group: Im$\bar{3}$m) with lattice parameter $a = 3.146$Å (ICDD 04-014-7435), and retains the bcc structure until the melting point.

1.1.1 Phase diagram

Several reports exists in the literature regarding the phase diagram of the Zr-Mo binary system [9–12]. In [12], the most up-to-date of these studies, a thermodynamic assessment of the Zr-Mo phase diagram was presented. In Figure 1.1(a) is shown the phase diagram reported in [12], which is also consistent with the experimental data available in the literature. It can be seen that the only intermetallic compound in the system is ZrMo₂ identified as Laves_c15 (space group: Fd$\bar{3}$m). In this phase, Zr atoms are located on the sites of a diamond structure and
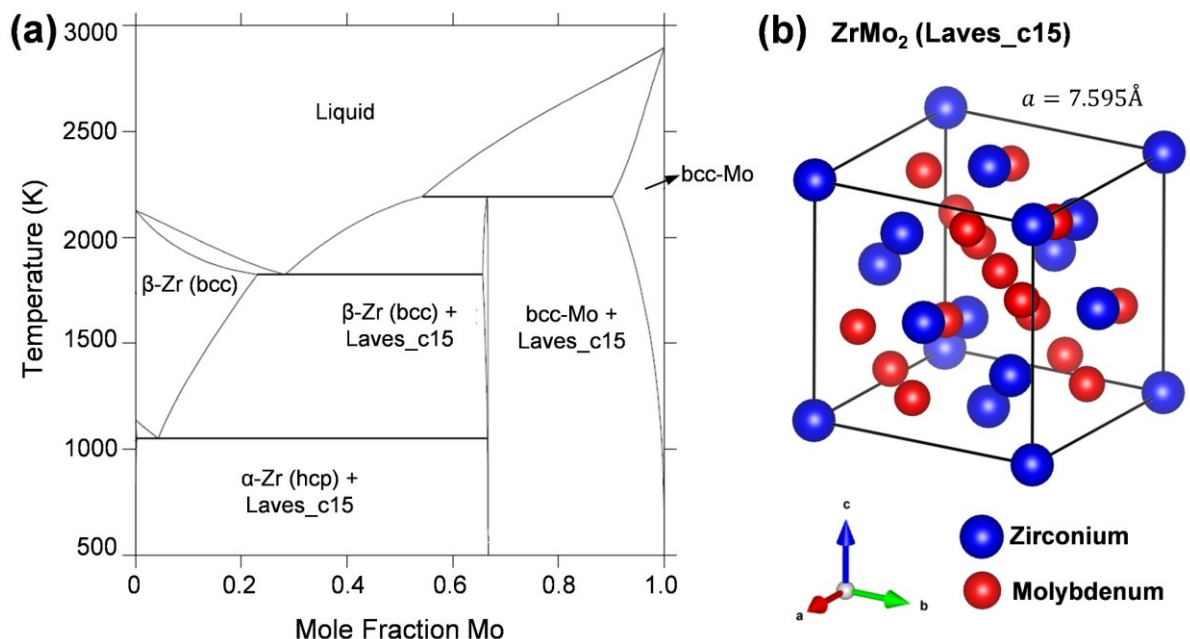
Figure 1.1. (a) Zr-Mo phase diagram [12]. (b) Crystal structure of the ZrMo₂ intermetallic phase (Laves_c15).

Mo atoms form tetrahedra around Zr atoms. In Figure 1.1(b), a schematic of the crystal structure of Laves_c15 phase is shown. The phase diagram in Figure 1.1(a) shows that the Zr-Mo system presents three invariant reactions. The first one is the peritectic formation of the Laves_c15 phase, the second one is the eutectic decomposition of the melt into β-Zr and Laves_c15 and the third invariant reaction is the eutectoid decomposition of β-Zr into α-Zr and Laves_c15.

Table 1.1. Elastic constants of the intermetallic compound $ZrMo_2$.

E (GPa)	B (GPa)	G (GPa)	B/G	v	Ref.
157.4	187.9	57.8	3.25	0.36	[13]
156.6	196.5	57.3	3.43	0.37	[14]
158.9	188.9	58.4	3.26	0.36	[15]

The properties of the Laves_c15 phase has been investigated by several authors [13–15]. They studied the structural and mechanical properties of $ZrMo_2$ from first principle calculations. The isotropic elastic properties of $ZrMo_2$ polycrystalline aggregates, such as Young's modulus (E), bulk modulus (B), shear modulus (G) and Poisson's ratio (v) reported in these papers are shown in Table 1.1. The parameter B/G is useful to describe the ductility of a material, high values (>1.75) indicates good ductility and low values mean that the material is brittle [16]. As can be seen, the intermetallic compound $ZrMo_2$ shows a B/G value higher than 3 indicating that this phase presents good ductility.

1.1.2 Superconductivity

The earliest works dedicated to study the properties of the Zr-Mo system were devoted to investigate the presence of superconductivity in this system [17–20]. This is not a coincidence as, in the 50s, two major advances in the understanding of the superconductivity were achieved: the phenomenological Ginzburg-Landau theory [21] in 1950 (published in Russian, an English version can be found in [22]), and the first microscopic theory of superconductivity proposed by Bardeen, Cooper and Schrieffer (BCS theory) [23] in 1957. The first report of superconductivity in the Zr-Mo system appears in 1965 [17]. At that time, it was already known that the Zr-Mo system presented the intermetallic compound $ZrMo_2$ with a Laves_c15 type
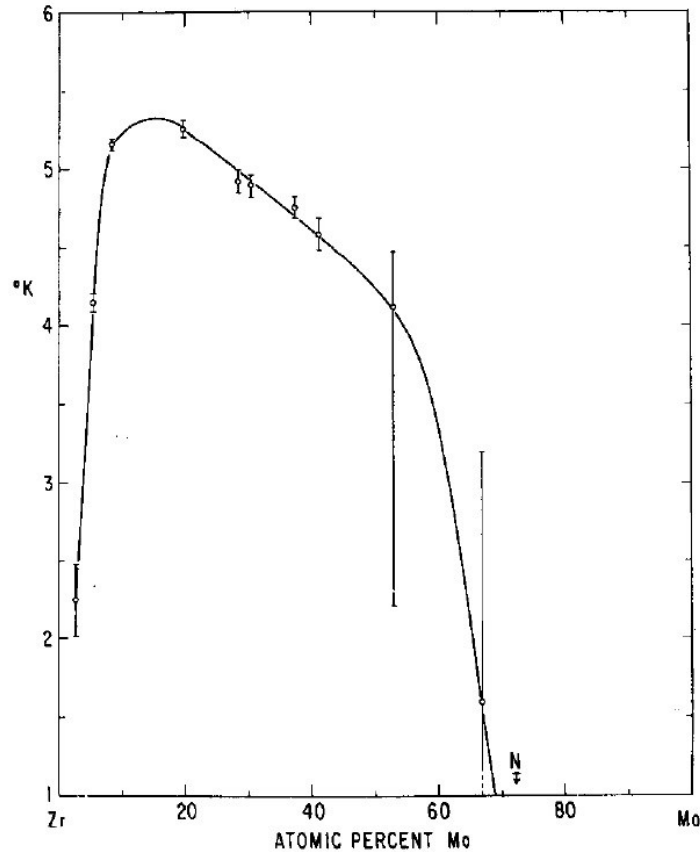
Figure 1.2. Evolution of the superconducting transition temperature in the Zr-Mo system [18].

structure. Furthermore, this compound was considered as favorable for the occurrence of superconductivity since it had been found that a large number of compounds with the same structure were superconducting [24]. Thus, in [17], the authors studied the intermetallic compound $ZrMo_2$ and reported a superconducting transition temperature (T_c) of 4.75 K.

Later on, Ö. Rapp [18] studied the superconducting behavior in the bcc phase of the Zr-Mo system in a wide range of compositions. To retain the bcc phase of Zr (β-Zr), the samples were obtained by fast quenching from the melt (see details in [18]). The evolution of T_c with composition reported in [18] is shown in Figure 1.2. In this figure is shown that when approaching the composition of the Laves_c15 phase, the superconducting transition temperature decreases. In a different study, Ö. Rapp *et al.* [20] reported that the critical temperature of the Laves_c15 phase is $T_c = 0.12$ K, too much lower compared to the value reported in [17]. Such difference in the reported values of critical temperature of the intermetallic phase $ZrMo_2$ was explained in [18] as due to the presence of a bcc phase (of higher critical temperature as shown in Figure 1.2) in addition to the Laves_c15 phase in the samples

8

used in [17]. Critical temperature values similar to those shown in Figure 1.2 were reported in [19]. In this case, the authors focused on the compositions close to pure Zr and showed that a small addition of Mo into the bcc phase of Zr increases the critical temperature of this phase, in line with the results presented in Figure 1.2.

1.1.3 Biocompatibility

In recent years, Zr-Mo alloys obtained by different metallurgical methods have been investigated for biomedical applications [25–30] due to the low cytotoxicity [31] and magnetic susceptibility [32] of both Zr and Mo. Metallic materials are required for medical implants and devices due to their good mechanical properties. Nowadays, magnetic resonance imaging (MRI) is a powerful diagnostic tool widely used in orthopedics and brain surgery. However, the use of metallic implants can interfere with MRI, affecting diagnostic. Therefore, the use of medical devices based on low magnetic susceptibility materials is required.

Zr-Mo alloys have proven to exhibit low magnetic susceptibility that made this system compatible with MRI [25–27]. In [25], the magnetic susceptibility was measured on Zr-rich Zr-Mo alloys, by varying the Mo content up to 15 wt%. In Figure 1.3 is shown the dependency of
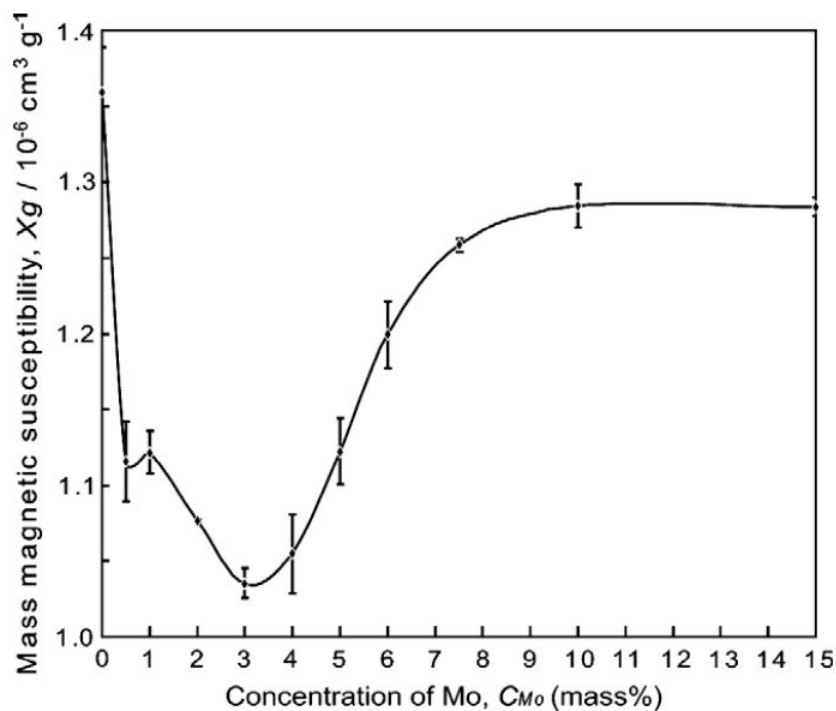
Figure 1.3. Magnetic susceptibility of Zr-Mo alloys [25].

the magnetic susceptibility with the wt% Mo reported in [25]. The authors related the evolution of the magnetic susceptibility with the phase constitution of the system. They showed that, when the minimum of magnetic susceptibility is achieved (at 3 wt% of Mo), the ω phase is favored (this is a metastable phase with simple hexagonal structure [33]). However, as shown in [26], Zr-Mo alloys presenting the ω phase were found brittle by tensile tests. Therefore, a compromise need to be achieved between good mechanical properties and low magnetic susceptibility in the Zr-Mo system. As shown in [27], the alloy with 1 wt% Mo, in which the ω phase was not present, exhibited higher hardness and bending strength than other Zr-Mo alloys and still presents low magnetic susceptibility. Therefore, it is preferred for medical devices used under MRI.

1.1.4 Mechanical properties

Beside superconductivity and biocompatibility, the mechanical properties of the Zr-Mo system have also been explored through the years [34–37]. In [34], time-temperature-transformation (TTT) curves for different compositions, based on resistometric technique were reported. In addition, the mechanical properties of these alloys were evaluated through tensile tests. The mechanical properties of Zr-Mo alloys have also been studied in [35] (where tensile-strain curves at high temperatures, from 900 to 1000 °C, were performed), and more recently in [36] and [37]. In these last two papers, the effect of alloying Zr to Mo were studied. In [36], the authors showed that the tensile strength of Mo–Zr alloys is much higher than that of pure Mo and the optimal tensile strength is obtained with the addition of 0.1 wt% of Zr. In [37], the mechanical properties of three Mo-based alloys, Mo-5X (X=Zr, Ti, V), were studied by microhardness measurements using Vickers indentation method. The three alloys presented higher hardness than pure Mo, Mo-5Zr being the alloy presenting the highest hardness. This was associated to the fact that Mo-5Zr alloy presented the $ZrMo_2$ phase additionally to the solid solution whereas Mo-5V and Mo-5Ti were single-phase solid solutions.

1.1.5   Zr-Mo thin films

The papers presented so far on the structure and properties of the Zr-Mo system deal with samples in their bulk form. In all of them, the samples were obtained by different metallurgical methods in which a liquid-to-solid transition occurs. To date, there exist few reports [1,38,39] on the structure and properties of Zr-Mo alloys in their thin film form, obtained by vapor-to-solid transition methods. In [1], the authors deposited Zr-Mo thin films in a wide range of compositions by magnetron sputtering method. The goal of this paper was to study the corrosion behavior of the alloys. The sputtered-deposited films showed lower corrosion rates in 12 M HCl solution at 30 °C, at atmospheric pressure conditions, compared to pure Zr and pure Mo films. The authors claim that the presence of an amorphous structure is fundamental for the corrosion resistance of the films. In Figure 1.4 are shown the X-ray difractograms of Zr-Mo alloys at different composition reported in [1]. It can be seen that a transition from an amorphous to a crystalline structure occurs around 60 at% Mo. The structural transition at this composition for sputter-deposited Zr-Mo thin films is in line with the results that will be shown in this thesis.
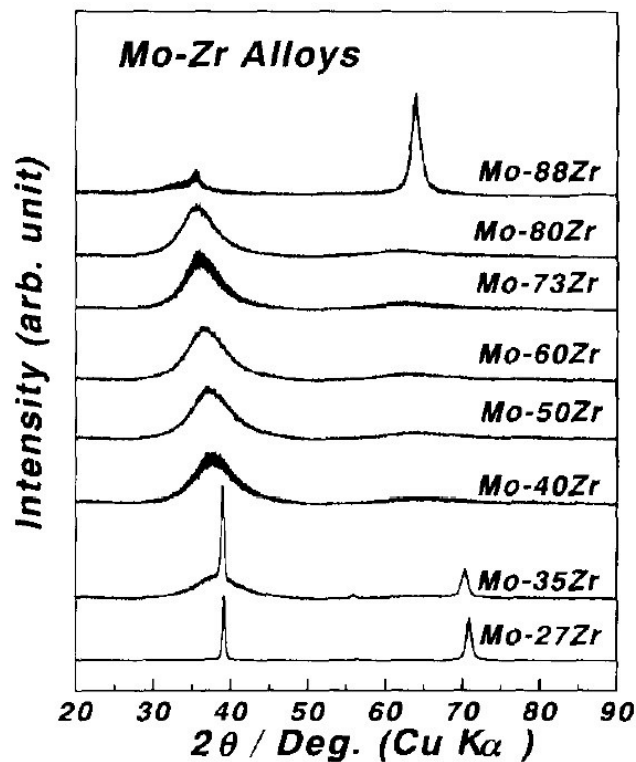
Figure 1.4. X-ray diffractograms of sputter-deposited Zr-Mo alloys [1].
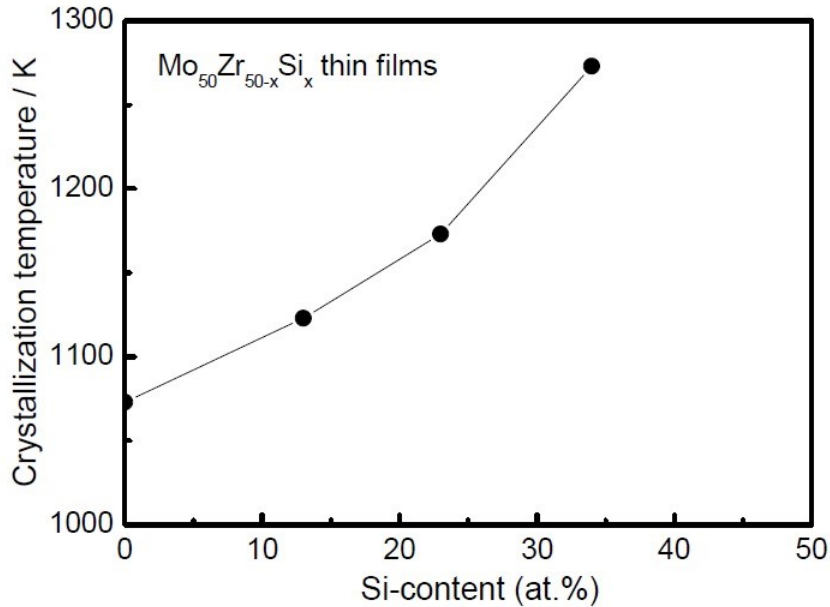
Figure 1.5. Crystallization temperature in $Mo_{50}Zr_{50-x}Si_x$ system [38].

In [38], the authors studied the influence of Si or Al incorporation in Mo-Zr alloys deposited by RF magnetron sputtering. In this paper, the crystallization temperature of the alloys as a function of the Si content was studied (see Figure 1.5). Interestingly, the authors measured a crystallization temperature of 1073 K for $Zr_{50}Mo_{50}$ (without Si addition) which constitutes the only experimental report of the crystallization temperature in Zr-Mo thin films alloys. Ref. [39] reports on part of the results obtained within this thesis and that are discussed in Chapter 3.

1.2 Zr-W system

Similar to Zr and Mo, W is a refractory metals with the highest melting point of all the elements (melting point of 3695 K). At room temperature, W presents a bcc structure (space group: $Im\bar{3}m$) with lattice parameter $a = 3.165$Å (ICDD 00-004-0806), and retains the bcc structure until the melting point. In Figure 1.6 is presented the phase diagram of the Zr-W system [40]. As can be seen, the phase diagram of both systems, Zr-W and Zr-Mo show similar characteristics. First, as in the case of Zr-Mo, in Zr-W there is only one intermetallic compound ZrW_2, identified as Laves_c15. Secondly, there exist just three invariant reactions for this system: the peritectic formation of the intermetallic compound ZrW_2, the eutectic formation of β-Zr and ZrW_2 and the eutectoid decomposition of β-Zr into α-Zr and ZrW_2.

12
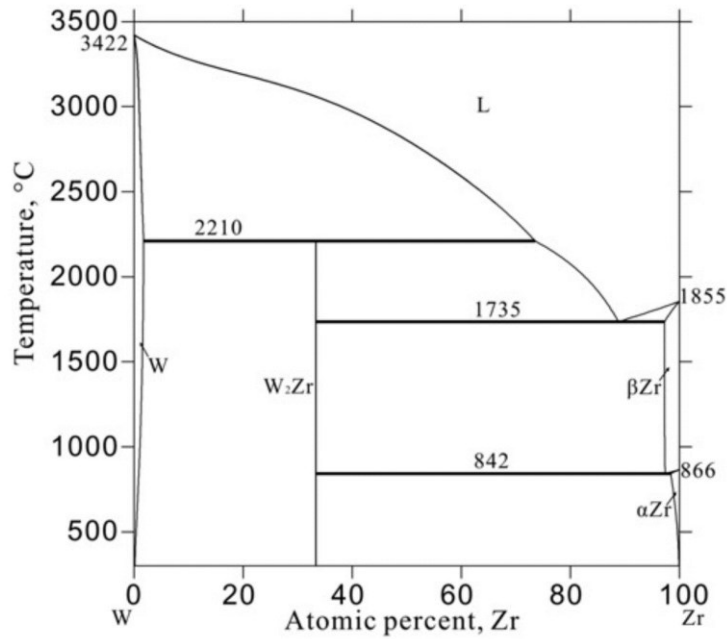
Figure 1.6. Zr-W phase diagram [40].

There are few reports on the structure and properties of alloys in the Zr-W system in their thin film form [3,7,8]. In [7] the structure and corrosion behavior of sputtered-deposited Zr-W alloys was studied. The authors reported on a transition from an amorphous to a crystalline structure in this system. This is evidenced in the X-ray diffractograms of Figure 1.7, where the transition is observed around 80 at% W. Alloys in amorphous and crystalline forms showed higher corrosion resistance in 12 M HCl at 30 °C than pure Zr and W [7].
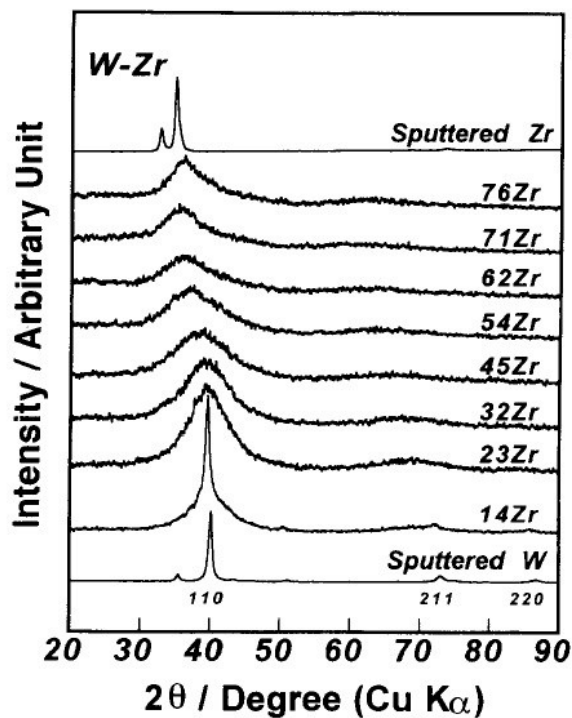
Figure 1.7. X-ray diffractograms of sputter-deposited Zr-W thin films [7].
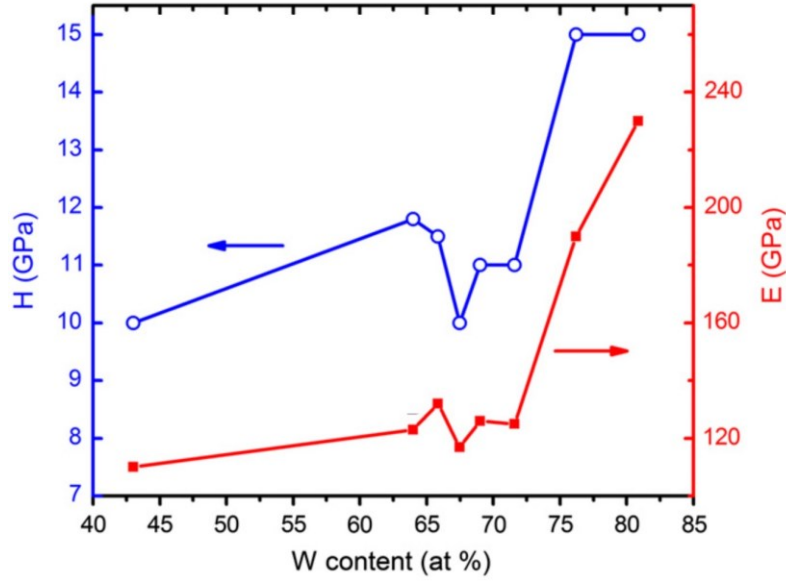
Figure 1.8. Evolutions of Hardness H and Young's modulus E with W content of sputter-deposited Zr-W thin films [8].

In our group, Zr-W thin films obtained by magnetron sputtering have been already investigated [3,8]. In a first study [3], Zr-W alloys were deposited in a wide range of compositions (from 0 to 81 at% W). The X-ray diffractograms showed a transition from an amorphous to a crystalline structure similar to that reported in [7], but at a lower composition of 70 at% W. In addition, in this paper the presence of the Laves phase ZrW_2 was reported around the transition, which was not observed in [7]. In a second study, Zr-W thin films were deposited by co-sputtering in order to study their mechanical properties [8]. High hardness H above 10 GPa and low Young's modulus E below 230 GPa were obtained, as can be seen in Figure 1.8. In consequence, high H/E ratios up to 0.09 were achieved. The friction coefficient of the films were also measured against a diamond tip, giving low values between 0.08 and 0.15.

Zr-Mo and Zr-W systems present several structural similarities, either when obtained in stable equilibrium conditions (see phase diagrams in Figure 1.1 and Figure 1.6) or in out-of-stable equilibrium conditions (see X-ray diffractograms in Figure 1.4 and Figure 1.7). For this reason, the Zr-W system will be employed in this thesis as a complement to extend the results obtained for Zr-Mo. Effectively, we will show that the phenomena occurring in sputter-deposited Zr-Mo alloys for compositions around the amorphous to crystalline transition, can be extrapolated to the Zr-W system.

14

Chapter 2

Sputter deposition process, thin film growth and characterization methods

ABSTRACT: In this chapter, we describe the magnetron sputtering technique used throughout this thesis for the growth of Zr-Mo and Zr-W thin films. Some aspects related to the growth mechanisms of thin films and the main features of the characterization methods used in this thesis are also presented. In addition, we show the specific parameters used for the growth and characterization of the samples.

Contents

2.1 Introduction

In this chapter, we describe the general features of the growth and characterization techniques used throughout this thesis. Some aspects related to the basic growth modes of a thin film and the structure zone models are discussed. Zr-Mo and Zr-W thin films have been synthesized by magnetron sputtering. X-ray diffraction (XRD), scanning electron microscopy (SEM), energy dispersive spectroscopy (EDS) and transmission electron microscopy (TEM) have been employed to study the structure and the microstructure of the films. In-plane residual stress was determined, based on the curvature method, using a white light interferometer. Roughness and height distribution functions of the surface of the films were determined using atomic force microscopy (AFM). Optical reflectance measurements were performed in the 350-900 nm range using a spectrophotometer. The mechanical properties of the films were measured by nanoindentation.

2.2 Magnetron sputtering deposition process

2.2.1 Sputtering: Basic principles

Physical vapor deposition (PVD) methods encompass a wide variety of techniques used for the synthesis of thin films. All of them are characterized by the physical generation of a vapor from the source material, usually named as target, which is then condensed as a thin film on the surface of the desired substrate. The difference between the PVD methods relies on the way that the vapor is generated from the source material.

One of the most used PVD methods is sputtering. In this technique, a negative potential is applied to the target in the presence of a rarefied atmosphere of an inert gas (usually Ar), while the walls of the reactor chamber are connected to ground. This establishes an electrical discharge between the target (cathode) and the walls of the reactor chamber (anode). The positive ions (usually Ar^+) derived from the electrical discharge are accelerated towards the target. The bombardment of these ions onto the target causes the ejection of target atoms by momentum transfer, which then condensate on a substrate to form a film of the target material. A schematic of this process is shown in Figure 2.1(a). Besides the ejection of target atoms (1), the impact of the target by the ions can also lead to the implantation of the incident ion into the
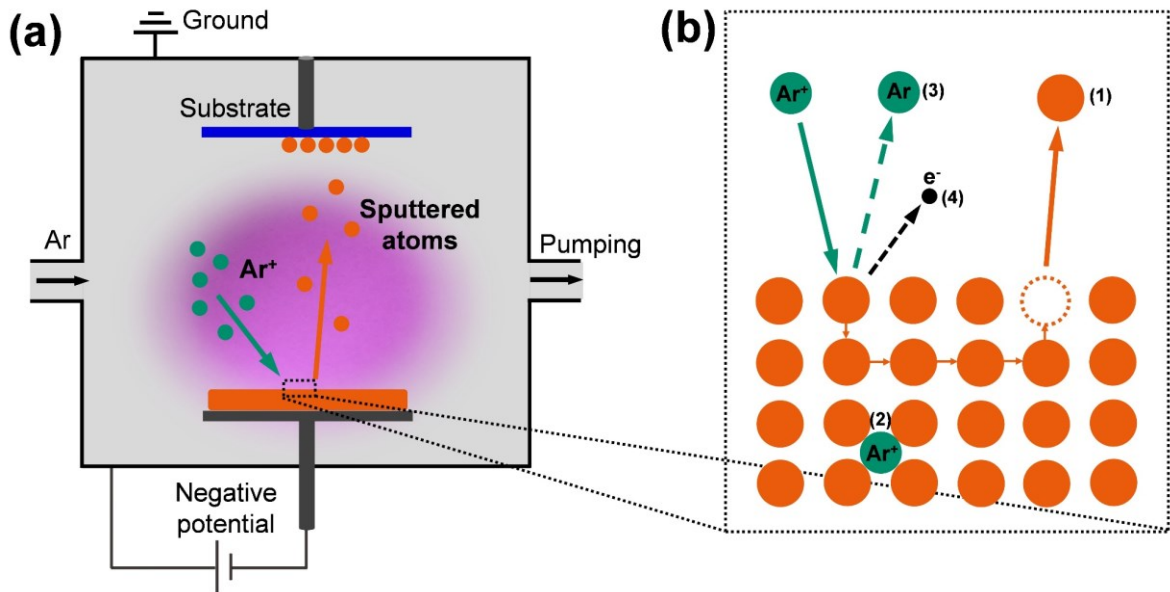
Figure 2.1. Schematic of the sputtering process (a) and main mechanisms resulting from the interaction of an Ar^+ ion and the target atoms (b).

target after its neutralization (2), the reflection of the incident ion neutralized by charge transfer (3) or the emission of secondary electrons (4). All these process are illustrated in Figure 2.1(b). In order to obtain sputtering as an useful thin film deposition process, it is important to satisfy some conditions. Firstly, the kinetic energy of the ions impacting on the target must be high enough to eject atoms from the material, i.e. it has to be higher than the binding energy of the material. Secondly, ejected atoms must be able to reach the substrate, i.e. the sputtered atoms must not be thermalized consecutively to repeated collisions with atoms of the background gas. For these reasons, low pressures are required in a sputtering process: on the one hand, it helps to maintain high ion energies and on the other, it prevents too many sputtered atom-background gas atom collisions after the ejection from the target.

Two important parameters in the sputtering process are the number of sputtered atoms per incident ion, i.e. the sputtering yield (Y), and the number of emitted electrons per incident ion, i.e. the secondary electron emission coefficient of the target material (γ). In Table 2.1 are presented sputtering yield data for some elements as a function of Ar^+ ion energy [41,42]. We highlight the values for the three elements that will be used in this thesis: Zr, Mo, and W. For most of metals, γ is around 0.1 when working with Ar^+ ions [43].

Table 2.1. Sputtering yield for some elements as a function of Ar^+ ion energy.

Target	Incident Ion Energy: Ar^+			
	100 (eV)	200 (eV)	300 (eV)	600 (eV)
Be	0.074	0.18	0.29	0.80
Al	0.11	0.35	0.65	1.24
Si	0.07	0.18	0.31	0.53
Ti	0.081	0.22	0.33	0.58
V	0.11	0.31	0.41	0.70
Cr	0.30	0.67	0.87	1.30
Fe	0.20	0.53	0.76	1.26
Co	0.15	0.57	0.81	1.36
Ni	0.28	0.66	0.95	1.52
Cu	0.48	1.10	1.59	2.30
Ge	0.22	0.50	0.74	1.22
Zr	0.12	0.28	0.41	0.75
Nb	0.068	0.25	0.40	0.65
Mo	0.13	0.40	0.58	0.93
Ru	0.14	0.41	0.68	1.30
Rh	0.19	0.55	0.86	1.46
Pd	0.42	1.00	1.41	2.39
Ag	0.63	1.58	2.20	3.40
Hf	0.16	0.35	0.48	0.83
Ta	0.10	0.28	0.41	0.62
W	0.068	0.29	0.40	0.62
Re	0.10	0.37	0.56	0.91
Os	0.057	0.36	0.56	0.95
Ir	0.12	0.43	0.70	1.17
Pt	0.20	0.63	0.95	1.56
Au	0.32	1.07	1.65	2.43(500)
Th	0.097	0.27	0.42	0.66
U	0.14	0.35	0.59	0.97

2.2.2 Balanced and unbalanced magnetron sputtering

The basic sputtering process described so far is limited by the low ionization efficiencies in the plasma, which leads to low deposition rates. This limitation has been overcome by the development of magnetron sputtering [44–47]. Effectively, the incorporation of a magnetron device formed by two concentric magnets of inverted polarities, as shown in Figure 2.2, can constrain the secondary electron motion to the vicinity of the target. In this way, their probability of experiencing an ionizing collision with an atom of the background gas is

increased substantially and, consequently, the ionization efficiency also increases. With the increase of the ionization efficiency, a dense plasma is created near the target region, which increases the ion bombardment of the target, leads to higher sputtering rates and, therefore, higher deposition rates.
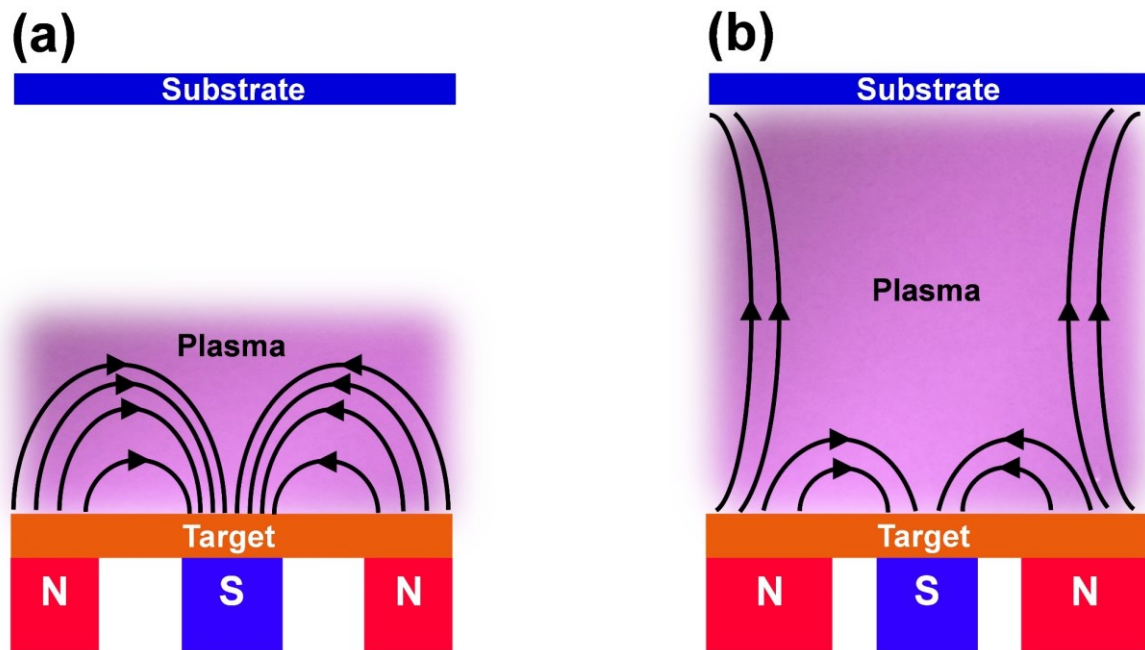
Figure 2.2. Schematic of the magnetic configuration and plasma confinement in balanced (a) and unbalanced (b) magnetrons.

Depending on the degree of confinement of the plasma, magnetrons can be divided into balanced and unbalanced magnetrons. In a balanced magnetron, the inner and outer magnets are configured in such a way that the magnetic lines coming out from the outer magnet enter into the inner magnet, i.e. the magnetic lines are closed between the inner and outer poles. Thus, the plasma is confined to the target region, as shown in Figure 2.2(a). In an unbalanced magnetron, the outer magnet is intensified as compared to the inner magnet and, consequently, several of the magnetic lines exiting the outer magnet are directed towards the substrate. In this way, the fast moving secondary electrons that escape from the target surface can be directed to the substrate, increasing ionizing collisions with neutral gas atoms far away from the target surface. Thus, the plasma is no longer confined to the target region, as is illustrated in Figure 2.2(b). The advantage of unbalanced magnetron sputtering with respect to balanced magnetron

sputtering is the considerable increase of the ion bombardment to the substrate, which results in an increase in the quality of the film.

In this thesis, two sputtering chambers were used: in chamber 1, the magnetrons were unbalanced and in chamber 2, the magnetrons were balanced (see section 2.2.4 for details of the chambers).

2.2.3 Electrical control of the discharge

The electrical parameters of the discharge can be regulated by controlling one of them, i.e. the electrical current, the voltage or the power. During a sputtering deposition, these parameters are changing over time due to several effects. First, the target is progressively etched in an inhomogeneous way because sputtering is more intense in the area, named as target racetrack, between the inner and outer magnets. As the target is getting thinner in the racetrack, the efficiency of trapping electrons by the magnetron increases. Moreover, in the meantime the target surface evolves from flat towards eroded profile. Thereby, the developed surface area increases, leading to lower current densities for a given average discharge current. Finally, the temperature of the target surface increases at the beginning of a deposition run, modifying both Y and γ. Thus, special attention must be paid to the parameter used to control the discharge, especially for long deposition runs. A typical voltage-current curve of a discharge is shown in
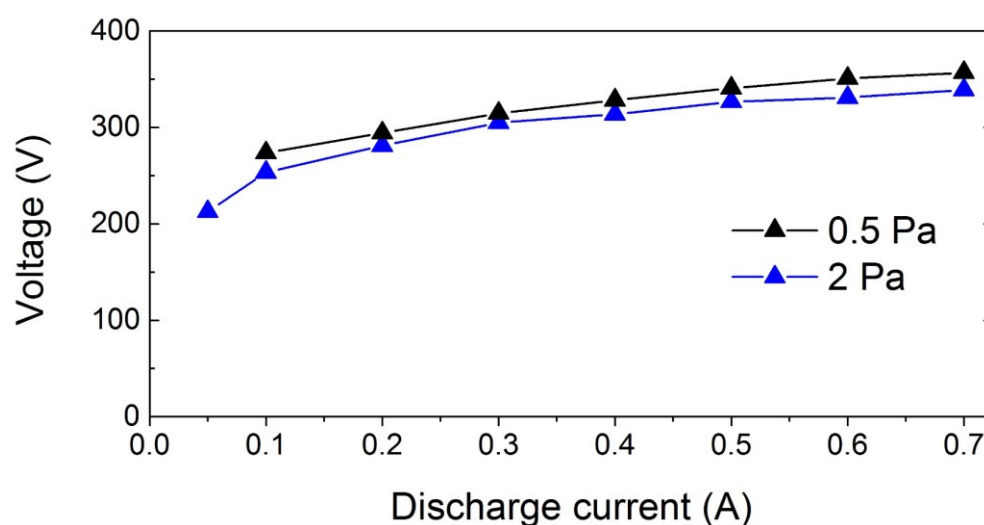
Figure 2.3. Voltage-current characteristic of a magnetron discharge from a Mo target in argon atmosphere at 0.5 and 2 Pa.

Figure 2.3. From the figure, it follows that small fluctuation of the discharge current cause minor modifications in voltage, while small fluctuation of the discharge voltage cause a more pronounced increase in the discharge current. Because of this, the best option to prevent strong evolutions of the sputtering conditions with time is to control the deposition by regulating the discharge current.

2.2.4 Composition and growth conditions of Zr-Mo and Zr-W thin films

Throughout this thesis, the influence of the chemical composition on the structure, microstructure and properties of Zr-Mo and Zr-W thin films will be investigated. Thus, in order to control the composition, two different approaches were employed:

First approach (chamber 1): The films were deposited using a combinatorial approach (see Figure 2.4(a)). To that end, a reactor chamber, called here chamber 1, was used. This chamber can be pumped down via a mechanical and a turbo-molecular pumps allowing a base vacuum of 10^{-4} Pa. It is equipped with two targets with their axes parallel and separated from each other by 14 cm. In this configuration, the substrate is placed along the line connecting the target axes. In this way, keeping the substrate holder in a fixed position and applying a constant discharge
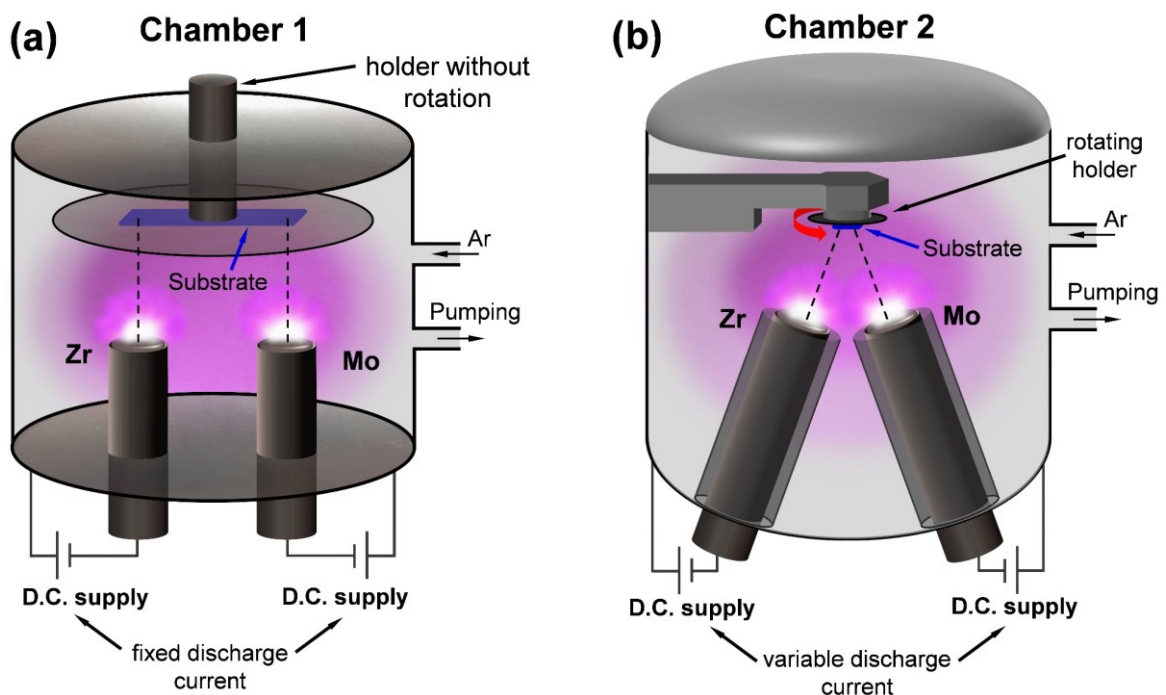
Figure 2.4. Schematic of the sputtering chambers used to synthesize films employing approach 1 (a) and approach 2 (b).

current to the targets, the composition of the film deposited on the substrate changes as we move along the substrate. The advantage of this approach is that it is possible to obtain a wide range of compositions in just one deposition. It is a good way to start the study of a system and it will be used in Chapter 3 of this thesis. The disadvantage of this approach is precisely the inhomogeneity in composition along the substrate. Therefore, if we want to synthesize a homogeneous film with a specific composition, the second approach is preferable.

Second approach (chamber 2): The films were deposited with the cathodes mounted in a confocal configuration and with the substrate holder in rotation mode (see Figure 2.4(b)). To that end, another reactor chamber, called here chamber 2, was used. This chamber can be pumped down via a mechanical and a turbo-molecular pumps allowing a base vacuum of 10^{-6} Pa. Note that the base vacuum in chamber 2 is better than in chamber 1. Using this approach, the composition of the films is changed by varying the discharge current applied to the targets. In this way, homogeneous films with a specific composition can be obtained. This will be the approach used in Chapters 4, 5 and 6 of this thesis.

In Table 2.2 we present the general growth conditions used for the synthesis of the films obtained throughout this thesis.

Table 2.2. Growth conditions of the films obtained in this thesis.

Substrate	Glass or (110) silicon
Targets-to-substrate distance	5-9 cm
Argon pressure	0.5, 1, 2, and 3 Pa
Discharge current (Zr target)	0.3 A
Discharge current (Mo target)	0-0.7 A
Discharge current (W target)	0.4, 0.5 and 0.55 A
Deposition temperature	Not intentional heating. Self-established temperature lower than 50 °C.

2.3 Thin film growth

2.3.1 Basic growth modes

There are three basic modes of thin film growth as schematically represented in Figure 2.5. Volmer-Weber mode occurs when the adatoms are more strongly bonding among them than with the substrate (high interfacial energy), which results in the growth of 3D islands. This growth mode is typically observed when metallic films grow on insulators [48]. Frank-van der Merwe growth occurs when the bonding energy between adatoms is equal or lower than the bonding energy with the substrate (low interfacial energy). This results in the 2D layer-by-layer growth, which is the growth mechanism of homoepitaxial layers and have also been observed in heteroepitaxial metal on metal and semiconductor on semiconductor growth. Stranski-Krastanov growth is a combination of the previous two growth modes. The film starts to growth in a 2D layer-by-layer manner but as the thickness increases this type of growth becomes energetically unfavorable and island starts to form on top of the initial layers. One of the effects that can induce the transition from a 2D to a 3D island growth mode is the elastic strain energy accumulated in the film due to the lattice mismatch between film and substrate.
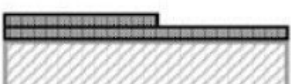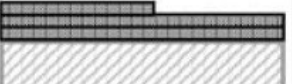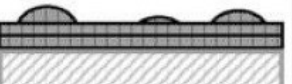
Coverage / Mechanism	$\theta < 1$ ML	$1 < \theta < 2$ ML	$\theta > 2$ ML
3D island growth			
2D layer growth			
S-K growth			

Figure 2.5. Schematic showing the different mechanisms of thin films growth: Volmer-Weber, Frank-van der Merwe and Stranski-Krastanov (from top to bottom) [48].

2.3.2 Structure zone models

The film microstructure is highly dependent on the deposition parameters such as substrate temperature and working pressure. With the aim of describing the dependence of film microstructure with these parameters, structure zone models have been developed. The first of these models was establish by Movchan and Demchishin [49]. They proposed that depending on the homologous temperature (T_h, defined as the ratio between the substrate temperature and the melting temperature of the material), the film morphology can be divided in three zones. Zone I occurs for $T_h < 0.3$, in this region the adatoms mobility is low and the films grow in a porous columnar structure and, consequently, the density of the film is lower than the bulk. Zone II occurs for $0.3 < T_h < 0.5$. In this region, the mobility of adatoms is higher and the growth is dominated by surface diffusion. In consequence, a columnar structure with uniform straight columns is formed through the entire film. In zone III, for $T_h > 0.5$ the high mobility of the adatoms allows bulk diffusion, resulting in a dense film structure. Large equiaxed grains in zone III replace the columnar structure of zone II.

Thornton [51] extended the structure zone model of Movchan and Demchishin to include the effect of the deposition pressure on the film microstructure. Furthermore, Thornton
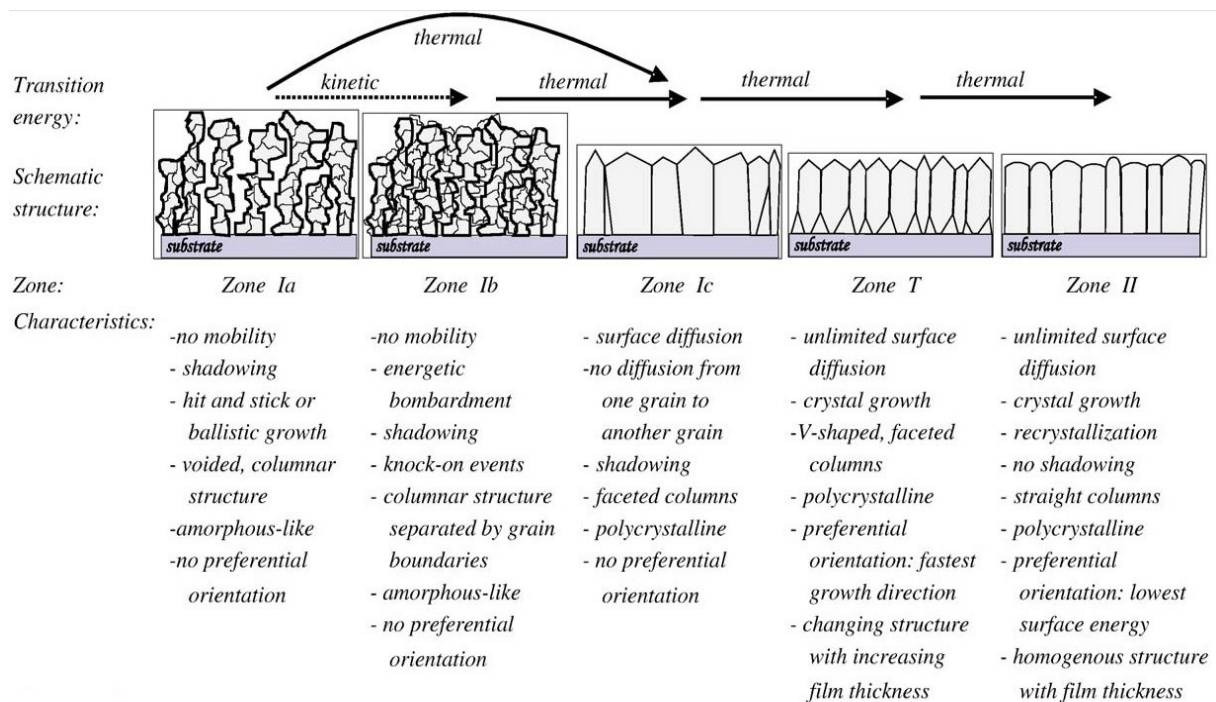
Figure 2.6. Schematic of the structure zone model proposed by Mahieu *et al.* [50].

24

introduced a new zone, called zone T, between I and II, in which the film morphology consists of dense fibrous grains.

An extended version of the structure zone model was proposed by Mahieu *et al.*[50], in which the diffusion of adatoms at the grain surface and between different grains are considered. A schematic of the different zones proposed by Mahieu *et al.* is depicted in Figure 2.6. As can be seen, zone I is divided in three (Ia, Ib and Ic). In particular, in zone Ic the adatoms have enough mobility to allow surface diffusion on a grain (self-diffusion) but diffusion from one grain to another is not allowed, which results in a faceted columnar structure (see Figure 2.6). When temperature is further increased, allowing to reach zone T, diffusion between grains become available and a competitive growth mechanism appears, in which the grains with the geometrically faster growing direction overgrow the other grains, resulting in a preferential orientation of the film.

Anders [52] proposed a further extended structure zone diagram by taking into consideration the effect of the ion flux in the growth of the film. Anders introduced a generalized temperature T^* to replace T_h that also considers the potential energy of the atoms arriving to the substrate. In addition, Anders replaced the working pressure in the Thornton diagram by a term called normalized energy E^*, that takes into consideration the kinetic energy of the incoming particles. Finally, Anders incorporated a third axis (thickness) which considers the effect of densification and sputtering etching on the film microstructure. This new structure zone diagram is adapted to growth using ionized physical vapor desposition methods.

2.4 Thin film characterization

2.4.1 X-ray diffraction

X-ray diffraction (XRD) is one of the most widespread and important characterization tools in material science. It is based on the interference resulting from the interaction between monochromatic X-rays and a crystalline solid. When an incident X-ray beam interacts with a crystalline solid, it is scattered by the atoms forming the solid. The resulting scattering waves can produce constructive or destructive interference, creating a diffraction pattern. Constructive

interference of diffracted X-ray beams occur when Bragg's law is satisfied [53] (see Figure 2.7(a)):

$$2d_{hkl}\sin\theta = n\lambda, \qquad (2.1)$$

where d_{hkl} is the distance between crystallographic planes with Miller indices h, k and l (also called interplanar spacing), θ is the scattering angle, λ is the wavelength of the incident radiation and n is an integer which determines the order of reflection.

Different geometrical configurations can be used to measure X-ray diffractograms. Bragg-Brentano (or θ-2θ) geometry is one of the most commonly used. In this configuration (see Figure 2.7(b)), the X-ray source is fixed while the sample and the detector scan angular regions at $\dot{\theta}$ and $2\dot{\theta}$ rates, respectively. In this way, only the diffraction peaks corresponding with the crystallographic planes parallel to the sample surface are observed. A typical X-ray diffractogram is shown in the bottom panel of Figure 2.7(c) for a Mo film grown on Si substrate.

The three components describing the peaks in a diffractogram: position, intensity and shape (see upper panel in Figure 2.7(c)), contain information on the structure and microstructure of the sample. Each of these components will be used in this thesis as follows:

Peaks position: From the peak position, the interplanar spacing d_{hkl} can be directly determined using Bragg's law (eq. (2.1)). This will be exploited in Chapter 3.

Peaks intensity: From the peaks intensity, information on the preferred crystallographic orientation can be extracted. Thus, the volume fraction of grains with specific (hkl) planes parallel to the substrate can be calculated as [54,50]:

$$F = \frac{(I_{hkl}/I'_{hkl})}{\sum_i(I_{hkl}/I'_{hkl})}, \qquad (2.2)$$

where i goes over all observed diffraction peaks, I_{hkl} is the measured area under the (hkl) reflection and I'_{hkl} is the standard diffracted intensity for a randomly-oriented polycrystalline sample of the material under study. This will be exploited in Chapter 6.

Peaks shape: From the peak shape, microstructural information of the samples such as microstrain or crystallite (coherently scattering domains) size can be determined. The crystallite size D (measured in the direction perpendicular to the sample surface in the case of Bragg-Brentano configuration) can be estimated using Scherrer's formula [55]:
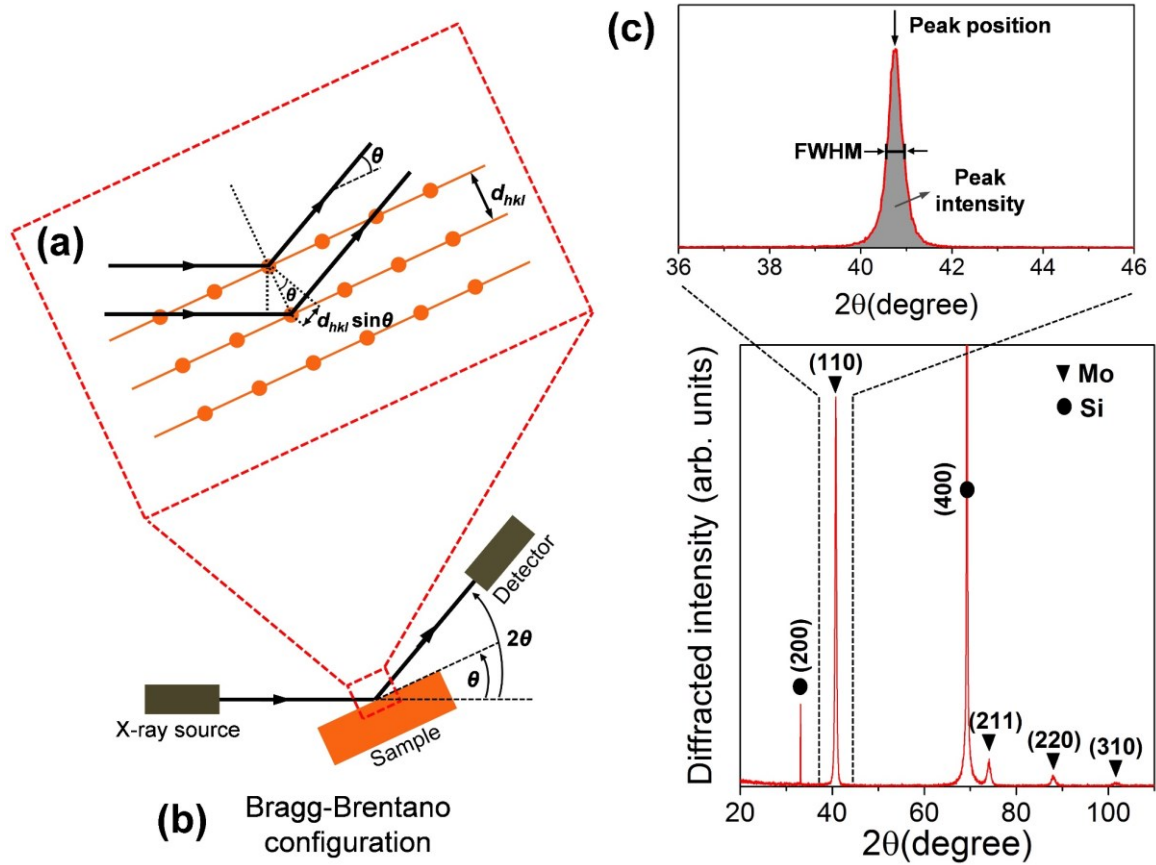
Figure 2.7. (a) Schematic representation of Bragg's law. (b) Schematic of the Bragg-Brentano configuration. (c) X-ray diffractogram of a film of Mo grown on Si substrate (bottom panel) and zoom of the first Bragg reflection of the Mo film showing the three components used to describe the peak (upper panel).

$$D = \frac{K\,\lambda}{\beta\,\cos\theta},\qquad(2.3)$$

where λ is the wavelength of the radiation, θ is the Bragg angle, β is the broadening (in radians) of the diffraction peak measured here as the full width at half maximum (FWHM), and K is the Scherrer's constant. The value of this constant depends on the definition of broadening used (FWHM in our case) and the crystallite shape. Here we will assume spherical crystallites for which $K = 0.829$ should be used [55]. A part of the peak broadening is due to microstrain in the sample. In this thesis, we obtain the crystallite size using Scherrer's formula considering that the entire peak broadening was due to size effects, therefore the values we obtain here are a lower boundary for the crystallite size. Scherrer's formula will be employed in Chapter 3.

In this thesis, XRD measurements were conducted in the Bragg-Brentano configuration with KαCu radiation (λ=1.5406 Å) using an AXS Bruker D8 Advance diffractometer.

2.4.2 Scanning electron microscopy and energy dispersive spectroscopy

Scanning electron microscopy (SEM) is a technique employed to obtain topographical images of the sample under analysis. A high-energy electron beam (accelerated by a voltage of a few kV) is used to scan the sample surface. As a result of the interaction between the electron beam and the sample, different signals are generated such as: secondary electrons, back scattered electrons, characteristic X-rays, among others, as can be seen in Figure 2.8. Secondary electrons, produced because of the inelastic interaction between the electron beam and the sample, are collected to acquire a high-resolution micrograph of the sample. Typical top-view and cross-sectional SEM images of a Zr-Mo thin film are shown in Figure 2.9(a)-(b). By the cross-sectional SEM images the thickness of the films can be determined.

Chemical analysis can be performed at the SEM through an energy dispersive spectroscopy (EDS) system. In this case, instead of the secondary electron, the X-ray emitted by the sample are detected and analyzed. X-rays are produced as a result of the interaction between the primary electron beam and the atoms of the sample. The electron beam excites the atoms of the sample producing the emission of X-ray, which allows to determine the chemical composition of the sample. A typical EDS spectrum performed to the film shown in Figure 2.9(a)-(b) is presented in Figure 2.9(c). Note that, besides Zr and Mo, a small amound of O is also detected, which is a general feature when highly reactive elements such as Zr and Mo are considered.
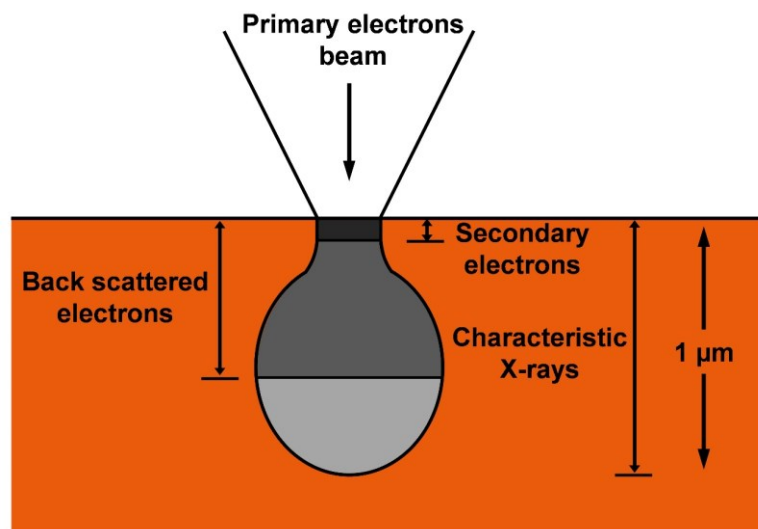
Figure 2.8. Schematic showing some of the signals generated as a result of the interaction between the electron beam and the sample surface.
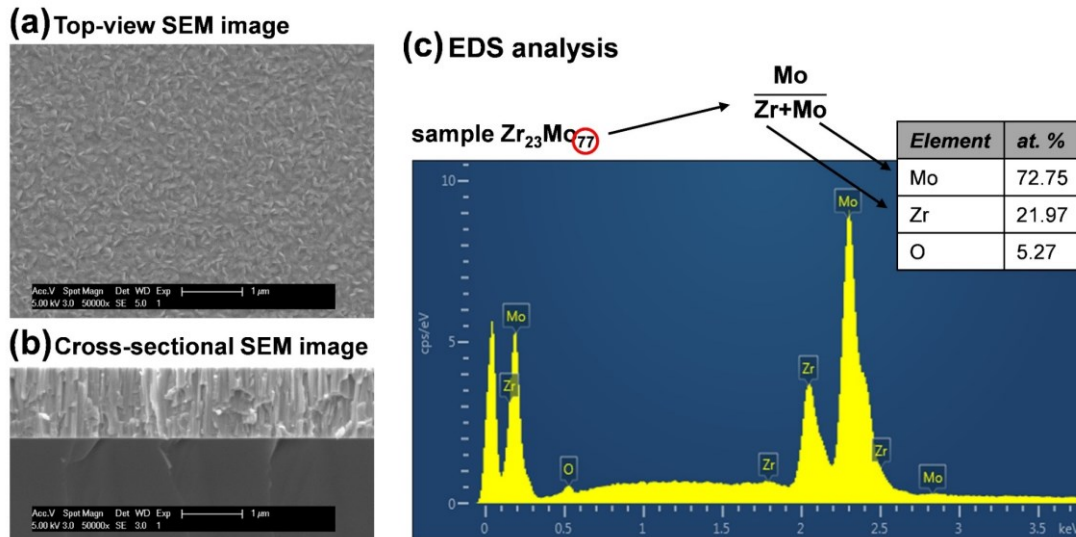
Figure 2.9. Top-view (a) and cross-sectional (b) images of Zr-Mo thin film. (c) EDS spectrum of film shown in (a) and (b).

EDS is known to generally overestimate the oxygen content. For this reason, the film composition reported in this thesis will be calculated as shown in Figure 2.9(c). Thus, the film presented in Figure 2.9 contains 77 at% Mo if oxygen is neglected, which was calculated by the ratio Mo/(Mo+Zr).

In this thesis, a Philips XL-30 S-FEG scanning electron microscope (SEM) was used to analyze the morphology of the samples. Cross-section SEM samples of films were prepared by breaking the sample after scratching the back side with a diamond tip.

2.4.3 Transmission electron microscopy

Transmission electron microscopy (TEM) is a powerful characterization technique that allows obtaining structural and microstructural information about the synthesized films. A high-energy electron beam ($\sim$ 200 kV) is accelerated onto an ultra-thin sample ($\sim$ 50 nm) and the transmitted electrons are collected. This signal is magnified allowing to form a 2D high-resolution image of the sample.

There are two basic modes of operation in a TEM: diffraction mode and image modes [56] (see schematic in Figure 2.10). When the TEM is operated in diffraction mode, the back-focal plane of the objective lens is projected onto the screen, and a diffraction pattern is obtained, that provides information about the crystalline structure of the sample. A pattern of spots is

obtained for single crystals, and each spot corresponds with a specific crystallographic plane in the direct space. Polycrystalline and amorphous materials give rise to a series of rings that are diffuse and wider in the case of amorphous materials. The same information can be obtained by performing a fast Fourier transformed (FFT) to a high-resolution TEM (HR-TEM) image. When operating in diffraction mode it is convenient to insert an aperture in the image plane to reduce the area of the sample under analysis allowing to reduce the intensity of the direct beam
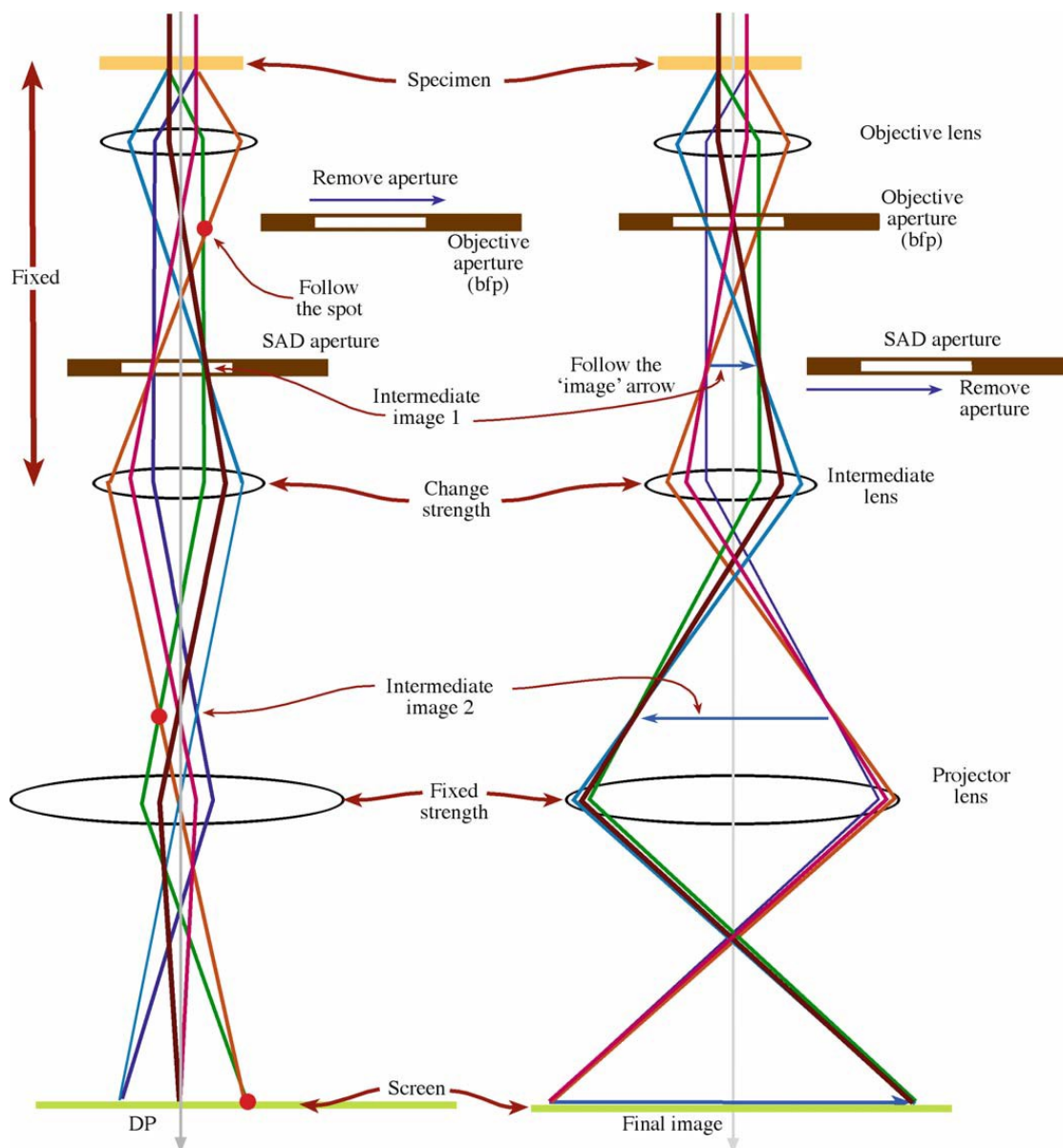
Figure 2.10. Schematic of the two basic modes of operations in a TEM. In diffraction mode (left) the diffraction pattern (DP) is projected onto the screen and in image mode (right) the image is projected onto the screen [56].
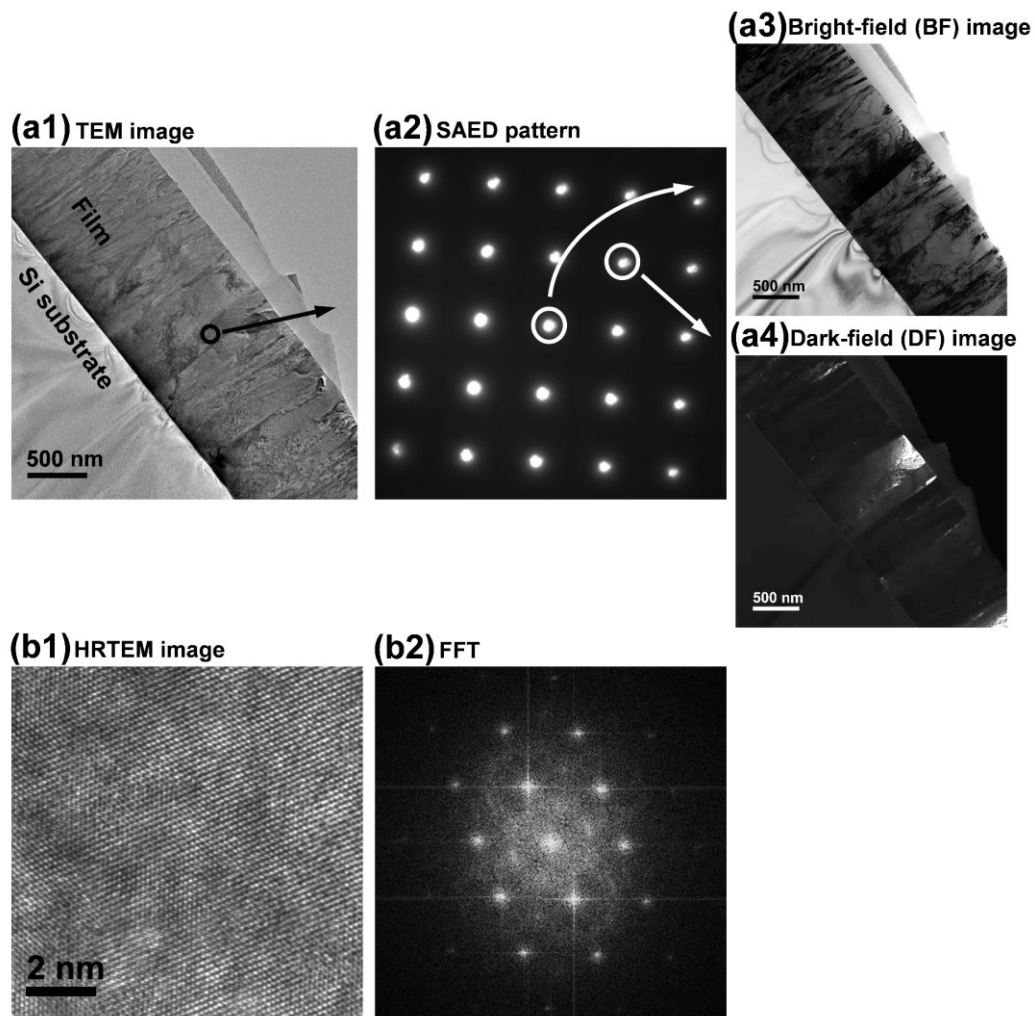
Figure 2.11. TEM analysis performed in a Zr-Mo film. (a1) TEM image showing the selected region (black circle) from which the SAED pattern (a2) was done. In the SAED pattern is shown with white circles the spots from which the BF (a3) and DF (a4) images were taken. HRTEM image (b1) and corresponding FFT pattern (b2).

and to obtain information of a localized region of the sample. This operation is called selected-area electron diffraction (SAED). A typical TEM analysis performed on a Zr-Mo film is shown in Figure 2.11. In Figure 2.11(a2) is shown the SAED pattern taken from the region marked with a black circle in Figure 2.11(a1). In Figure 2.11(b2) is shown the FFT pattern corresponding to the HRTEM of Figure 2.11(b1).

When the TEM is operated in image mode, the image plane of the objective lens is projected onto the screen, and an image of the samples is obtained. There are two basic imaging operations: bright-field (BF) and dark-field (DF). BF images are constructed from the direct beam. Therefore, brighter areas correspond to the presence of lighter elements, whereas darker

areas correspond to the presence of heavy elements, crystalline regions that are under diffraction condition or thicker regions of the sample. DF images are formed by selecting a specific diffracted beam instead of the direct beam. In this case, brighter areas correspond to crystalline regions under diffraction condition. BF and DF images of a Zr-Mo film are shown in Figure 2.11(a3) and Figure 2.11(a4), respectively.

TEM investigations were performed using a cold FEG JEOL ARM200 microscope. For this analysis, cross-section TEM samples of films were prepared using a focused ion beam (FIB)-scanning electron microscope (SEM) dual beam system (FEI Helios 600). The samples were obtained with the lift-out technique. The foil were prepared and thinned using an acceleration voltage of 30 kV. Nevertheless, an acceleration voltage of 5kV was used in the last step of the thinning, in order to minimize any possible artifact like amorphization or ion implantation.

2.4.4 In-plane residual stress

One of the approaches to measure the in-plane residual stress in a thin film is depositing it on a flat substrate. Then, by measuring the curvature of the substrate after deposition, the stress in the film can be determined using the Stoney equation [57]. In the case of elastically anisotropic substrates (as single crystal Si substrates), the modified Stoney equation is the following [58]:

$$\sigma = \frac{M_s}{6} \frac{h_s^2}{h_f} \left(\frac{1}{R} - \frac{1}{R_0} \right), \tag{2.4}$$

where h_f is the film thickness, h_s is the substrate thickness, M_s is the biaxial modulus of the substrate, R_0 is the curvature radius of the substrate before the film deposition and R is the curvature radius after the film deposition. In our case we used (100) Si substrates (M_s =180.3 GPa) with a thickness of 200 μm.

The curvature radii were measured by white light interferometry (WLI) using a Zygo NewView 7300 surface analyzer. In this technique, a white light beam is split in two parts, one is directed to a reference mirror and the other to the sample surface. The different optical path lengths of both beams produce an interference pattern that is used to reconstruct the topography of the sample surface (see Figure 2.12(a)). This method allows collecting surface height profiles
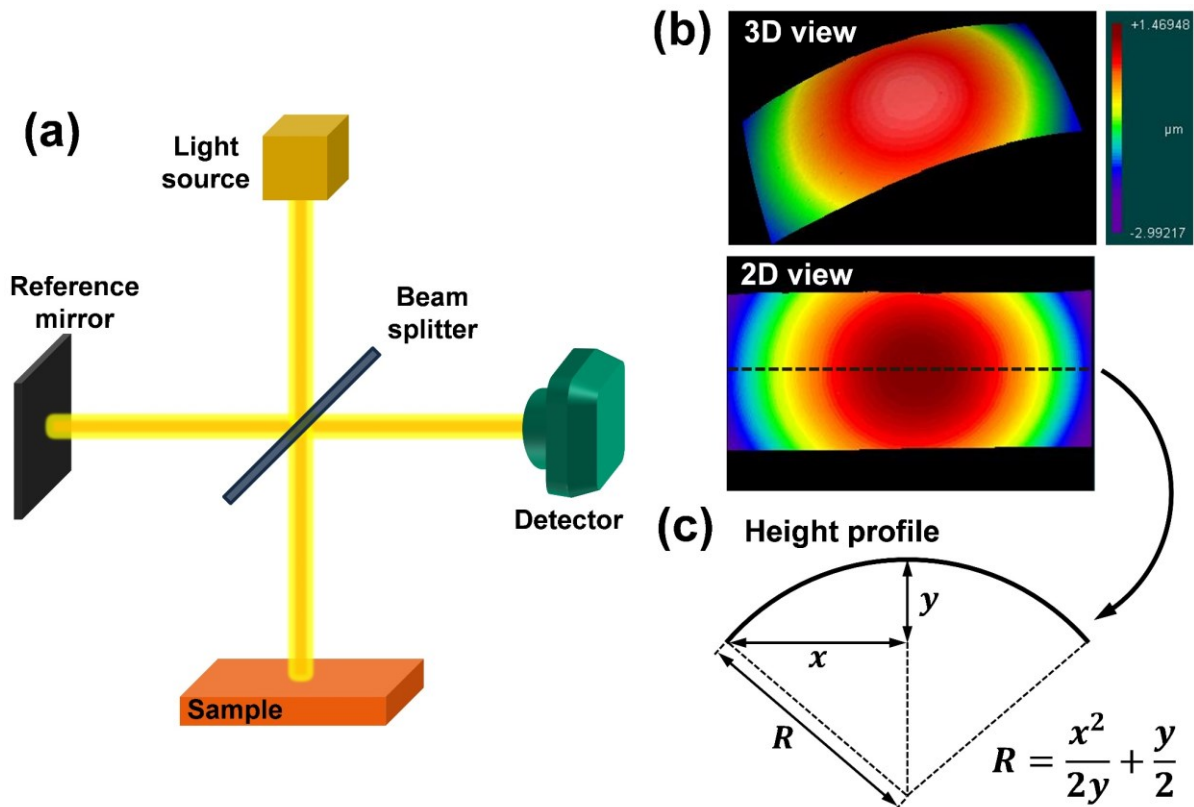
Figure 2.12. (a) Schematic of the WLI system. (b) 3D (top panel) and 2D (bottom panel) views of a Zr-W film under stress taken by using a white light interferometer. (c) Schematic showing how the curvature radius was calculated using the height profile extracted from the image shown in (b).

on 3D surfaces with a high vertical resolution (< 0.1 nm). Typical 3D and 2D views of a topographic image performed in a Zr-W thin film is shown in Figure 2.12(b). From the topographic image, a lineal height profile can be extracted and the curvature radius calculated as shown in Figure 2.12(c).

2.4.5 Statistic parameters of the films surface

The changes in the surface topography of the films were quantified by determining the height distribution function of the film surface and the roughness, calculated here as the root mean square (RMS) of the surface profile. These magnitudes were measured using Atomic Force Microscopy (AFM). In AFM, a sharp tip (tip diameter ~10 nm) is scanned over the sample surface. The interatomic forces between the sample surface and the tip produces a deflection of a cantilever when the topography at the surface of the sample is changing, which allows to obtain high-resolution 3D topographical images (see Figure 2.13(a)). In this thesis,
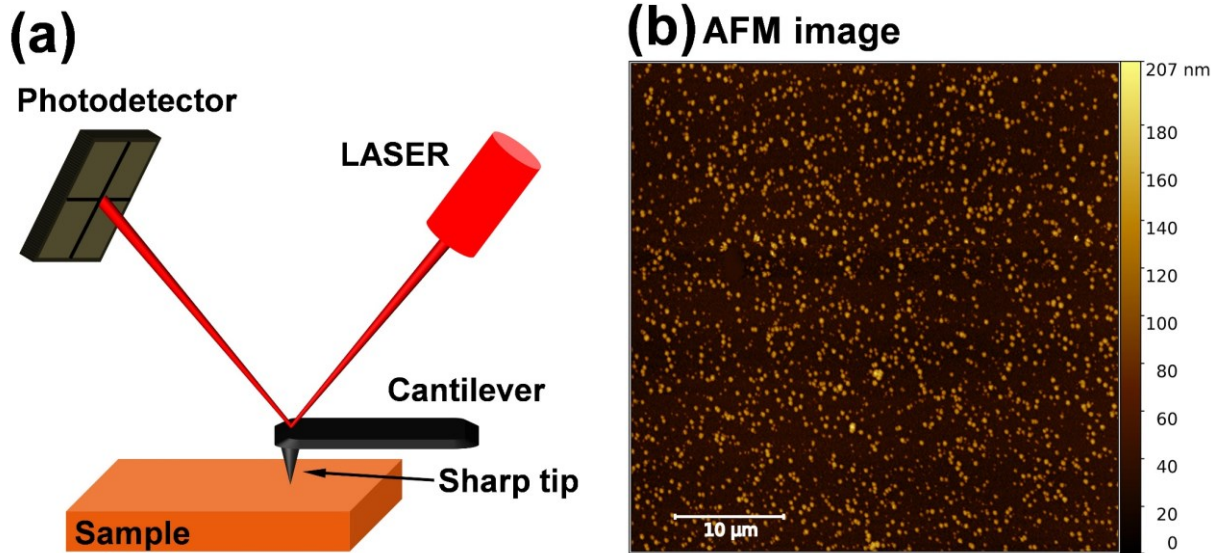
Figure 2.13. (a) Schematic of the AFM system. (b) AFM image of a Zr-Mo thin film.

the film topography was examined using a Nano-Observer Atomic Force Microscope developed by CSInstruments operated in resonant mode. An AFM image of a Zr-Mo thin film is shown in Figure 2.13(b). From the topographic image, the surface roughness together with the height distribution function of the film can be determined.

2.4.6 Optical reflectance

The reflectance is defined as the fraction of the incident electromagnetic radiation on a surface that is reflected by it. The total reflectance of a surface R_T can be divided into two terms: the specular reflectance R_S and the diffuse reflectance R_D. In specular reflectance, the incident ray is reflected from the surface in a single direction (mirror-like reflection). Real surfaces are not completely flat, which results in the appearance of a diffuse reflectance component, as can be seen in Figure 2.14.

A part of this thesis will be dedicated to study the modification of the surface topography in thin films. Consequently, a modulation of the reflectance is expected since this magnitude is very sensitive to the surface roughness.

The reflectance measurements were performed in the 350-900 nm range using a Varian Cary 5000 UV-vis-NIR spectrophotometer coupled with an integrating sphere. In this thesis, instead of the reflectance of the sample we use the relative reflectance R':

$$R' = \frac{R_S}{R_T}. \tag{2.5}$$
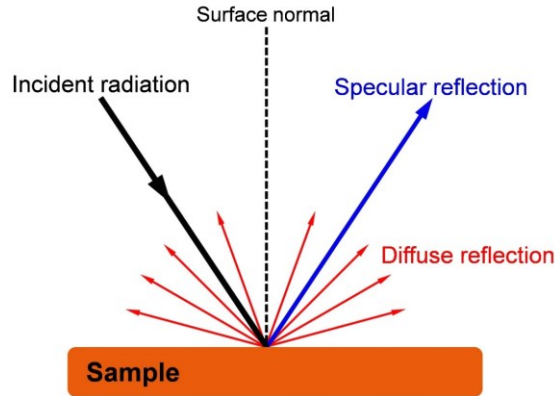
Figure 2.14. Specular and diffuse reflectance.

Commonly the specular reflectance is reported, however if divided by the total reflectance, a fraction that only depends on the surface topography is obtained [59–62]. Since we are interested in studying the way the reflectance is modulated by modifying the surface roughness of the films, this term is more relevant.

2.4.7 Mechanical properties

In order to determine the hardness H and Young's modulus E of the films, indentation tests were performed using a CSM Instruments (Anton Paar) Ultra Nanoindenter which allows a continuous capture of the penetration depth in the material and the force during the indentation process. The experiments were performed with a diamond Berkovich indenter tip with a maximum loading force of 300 μN. This force allows us to comply with the Buckle criterion on all measurements. This criterion is of paramount importance because if the penetration depth reaches more than 10% of the film thickness, the results are influenced by the substrate. For all the results, the loading rate of 600 μN min^{-1} was kept constant. For each measurement, the average of 10 indentation tests was taken. Hardness and Young's modulus were determined using Oliver and Pharr method [63–65]. Hardness was calculated as:

$$H = \frac{P_{\text{max}}}{A_{\text{c}}}$$

(2.6)

where P_{max} is the maximum indentation load and A_{c} the projected contact area (depending of the indenter shape). Young's modulus was calculated using the formula:

$$\frac{1}{E_{\text{eff}}} = \frac{1 - v^2}{E} + \frac{1 - v_i^2}{E_i}$$

(2.7)
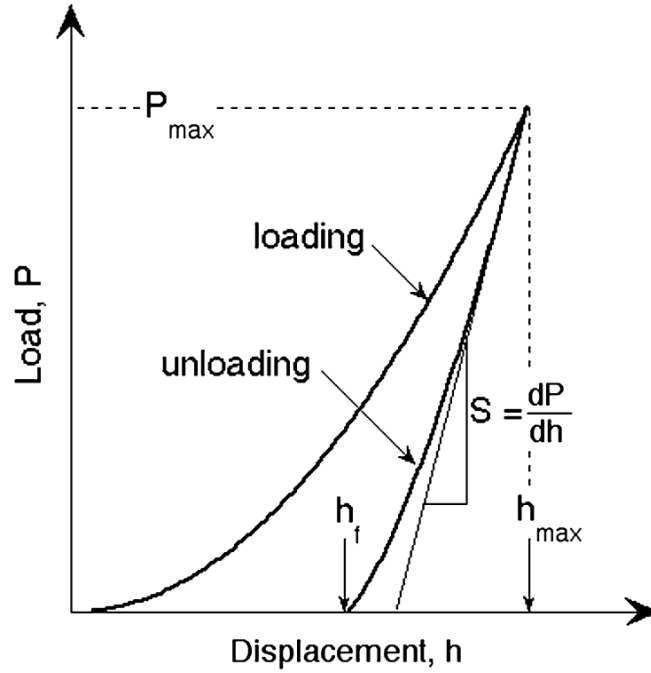
Figure 2.15. Schematic of a load-displacement indentation curve showing the important measured parameters [63–65].

where E and E_i are the Young's modulus of the sample and the indenter, and v and v_i are the Poisson's ratio of the sample and the indenter. For diamond, $E_i = 1141$ GPa and $v_i = 0.07$. The Poisson's ratio of the sample was fixed at 0.3. Finally, E_{eff} is the effective elastic modulus which can be calculated as:

$$E_{\text{eff}} = \frac{1}{\beta} \frac{\sqrt{\pi}}{2} \frac{S}{\sqrt{A_c}} \tag{2.8}$$

where β is a constant which depends on the geometry of the indenter ($\beta = 1.034$ for a Berkovich indenter) and $S = \mathrm{d}P/\mathrm{d}h$ is the slope of the initial portion of the unloading curve (stiffness). A schematic of an indentation curve showing the important measured parameters is shown in Figure 2.15.

The friction coefficient of the films was measured by sliding contact tests performed at a micrometer length scale, by means of a lateral force measurement attached to a MTS Nanoindenter XP. A Berkovich indenter was employed to scratch the film surface at a velocity of 10 µm s^{-1} under increasing load, up to a maximum of 200 mN. Different scan tracks were performed on each specimen at a fixed distance between tracks of 500 µm.

Chapter 3

Structural and mechanical properties of Zr-Mo thin films: From the nanocrystalline to the amorphous state
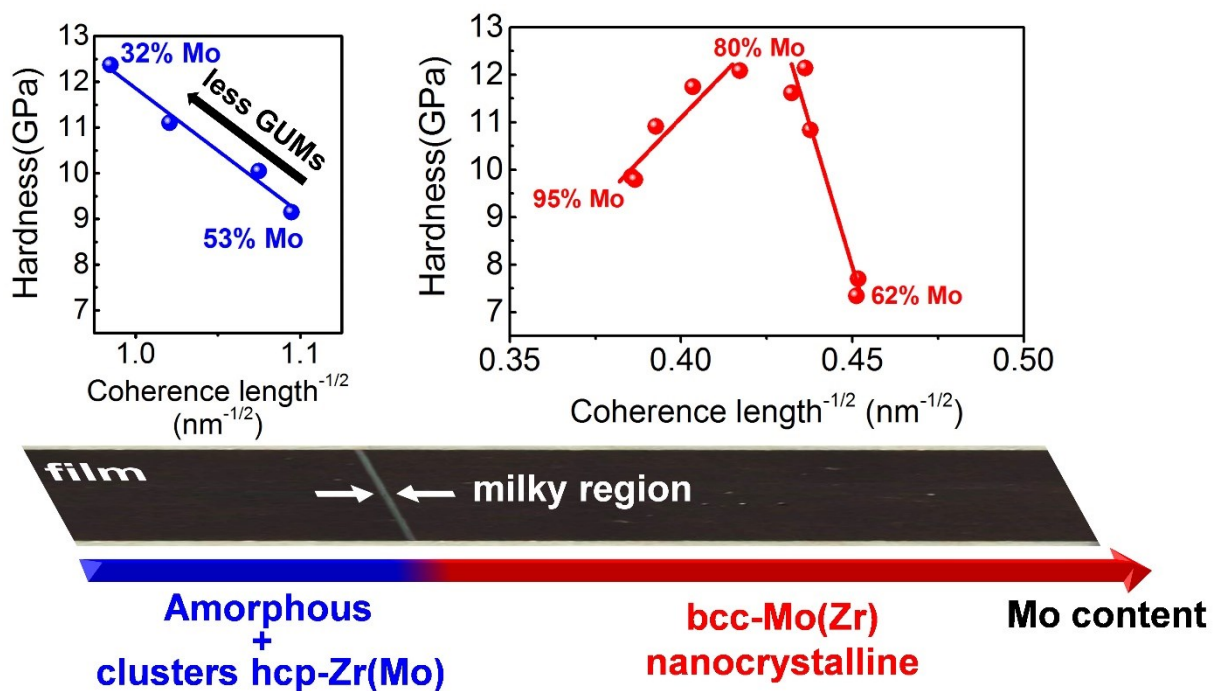
ABSTRACT: In this chapter, Zr-Mo thin films were synthesized in a wide composition range using a combinatorial approach by co-sputtering molybdenum and zirconium targets in the presence of argon. X-ray diffraction and transmission electron microscopy analyses reveal an evolution of the films structure from a nanocrystalline solid solution of Zr in the bcc lattice of Mo to clusters in an amorphous matrix with the same local order that a solid solution of Mo into hcp Zr. The coherence length deduced from X-ray diffractograms was around 1-7 nm depending on the composition. Mechanical measurements show that the films exhibited high hardness H, low Young's modulus E and therefore high H/E ratio compared with the bulk of Zr and Mo. We also found low friction coefficient values for all the films. Finally, an inverse Hall-Petch effect was observed for coherence length lower than 6 nm.

Contents

3.1 Introduction

Nanocrystalline and amorphous metallic alloys attract attention due to their modified mechanical properties compared to microcrystalline ones. Except for few cases, it is difficult to reach nanocrystalline and amorphous state in binary metal alloys using conventional metallurgy. The high quench rate associated to the vapor-to-solid transition in sputter-deposited metallic alloys can be high enough to disable the crystallization of many systems. This fact can be used for the formation of amorphous and nanocrystalline structures and tailor the properties of so-produced metallic alloy thin films. These can exhibit high hardness H values (for example, through Hall-Petch hardening in the case of the nanocrystalline materials) while keeping an elastic modulus E characteristic of metals. Hence, such strategy can significantly improve the H/E ratio, a parameter known to drive the friction behavior of materials [66].

The bonding state and, more particularly, the cohesive energy is also an important parameter within a strategy that aims at controlling the mechanical properties of nanostructured metals as it primarily determines their elastic behavior [5]. From this point of view, Zr-based binary alloys designed on the basis of Mo addition are particularly interesting. First, the good ability of sputter-deposited Zr-based alloys to form amorphous and nanocrystalline structures [1–4] can act in favor of the alloys hardening. Moreover, the intrinsic high hardness of Mo [5] and the high cohesive energy of Mo and Zr [6] among the transition metals make the Zr-Mo system a good candidate for hard metallic coatings with good elastic properties.

In this chapter, we propose to investigate the relationship between the structural and mechanical properties of Zr-Mo thin films deposited by co-sputtering. For this purpose, a combinatorial approach will be used, which allows in a single deposition experiment, to obtain films in a wide composition range.

3.2 Composition and structure

In Figure 3.1(a) a schematic of the sputtering chamber is presented together with the parameters used during the growth of the film. The film was deposited on a glass substrate. An optical image of the film obtained is shown in Figure 3.1(b). Interestingly, at 9.3 cm from Mo target axis the film exhibits a narrow region (width of approx. 1 mm) where the appearance
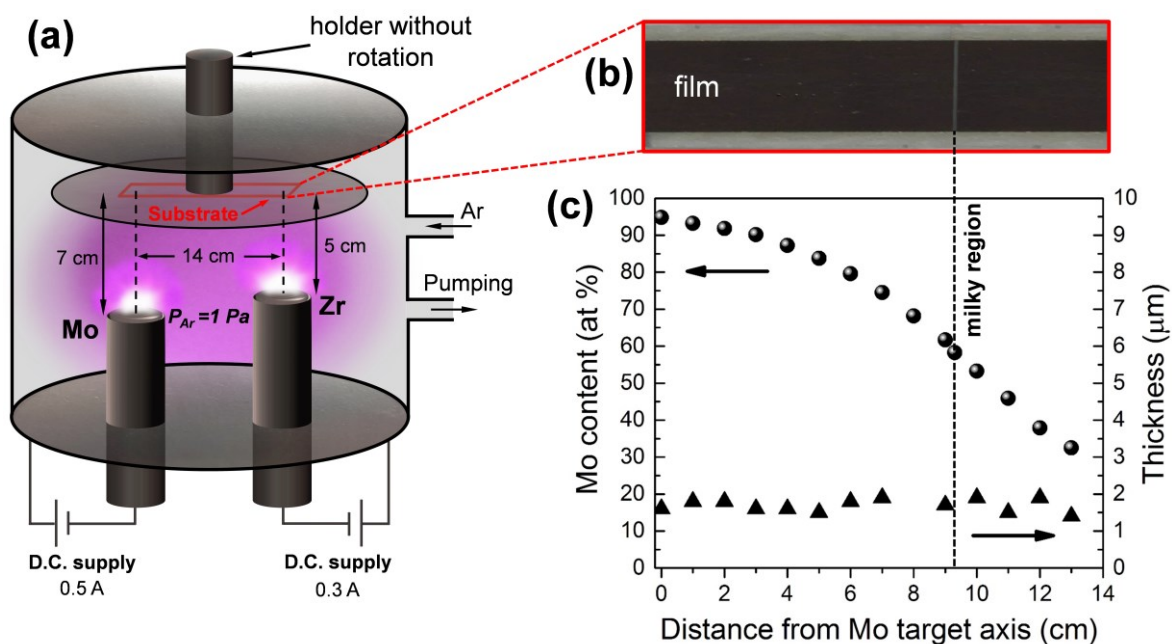
Figure 3.1. (a) Schematic of the sputtering chamber showing the parameters used during the film deposition. (b) Optical image of deposited film. (c) Evolution of the composition (circles) and the thickness (triangles) of the film as a function of the distance from the Mo target axis.

changes (the film has a milky-like appearance). This change in appearance is the first indication of a structural change in the film. Precisely, the objective of the next chapters of this thesis is to address the mechanisms behind its occurrence and its implication in the properties of the film.

As is shown with triangles in Figure 3.1(c), the thickness along the film is in the 1.4-1.9 µm range depending on position. Figure 3.1(c) also shows the evolution of the Mo content, calculated as the ratio $Mo/(Mo + Zr)$ of atomic contents (see Chapter 2), as we move away from the Mo target axis. Since the flux of particles impinging the growing film decreases with the distance from the target axis, the amount of Mo in the deposited film decreases with the distance from the Mo target axis, while that of zirconium increases keeping the film thickness quite constant. Thereby, it was possible to synthesize $Zr_{1-x}Mo_x$ films with x in the 0.32-0.95 range.

The X-ray diffractograms for different compositions are shown in Figure 3.2(a). In the case of sample with 58 at% Mo, it was impossible to obtain an X-ray diffractogram without overlapping of the adjacent regions in an area as narrow as the "milky region". However, as a
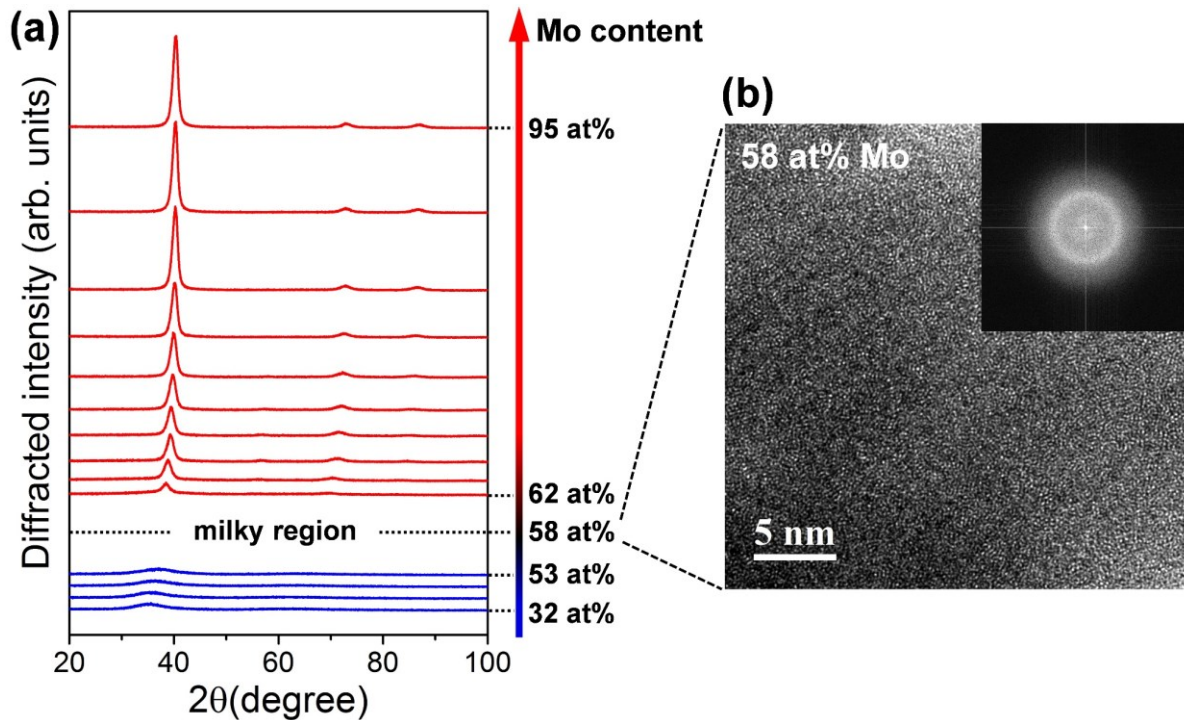
Figure 3.2. (a) X-ray diffractograms for the different Mo compositions. (b) HRTEM image and FFT of sample with 58 at% Mo (milky region).

first attempt to characterize the structure in this area, TEM analysis was performed (see Figure 3.2(b)). From the X-ray diffractograms, different structural behaviors can be identified depending on the Mo content, indicating a structural transition. From 95 to 62 at% Mo, the samples show well defined diffraction peaks, indicating the presence of a crystalline structure in this range of compositions. On the other hand, from 53 to 32 at% Mo, the samples show wide peaks typical of the amorphous structure. This transition is also evidenced in Figure 3.3, which shows the dependency of the interplanar spacing and the coherence length to the Mo content. The interplanar spacing was determined from X-ray diffractograms using Bragg's law (eq. (2.1)) taking the angular position of the first sharp diffraction peak (FSDP)[1]. The coherence length was estimated from the FSDP of the diffractograms using Scherrer's formula (eq. (2.3)). The transition from the crystalline to the amorphous structure when the composition is around 60 at% Mo has been previously observed in sputter-deposited Zr-Mo films [1].

---

[1] The term FSDP [67] usually refers to the first wide (and more intense) peak in the X-ray diffractogram of samples exhibiting an amorphous structure. Here we also use it to refer to the first diffraction peak of samples that exhibit a crystalline structure.
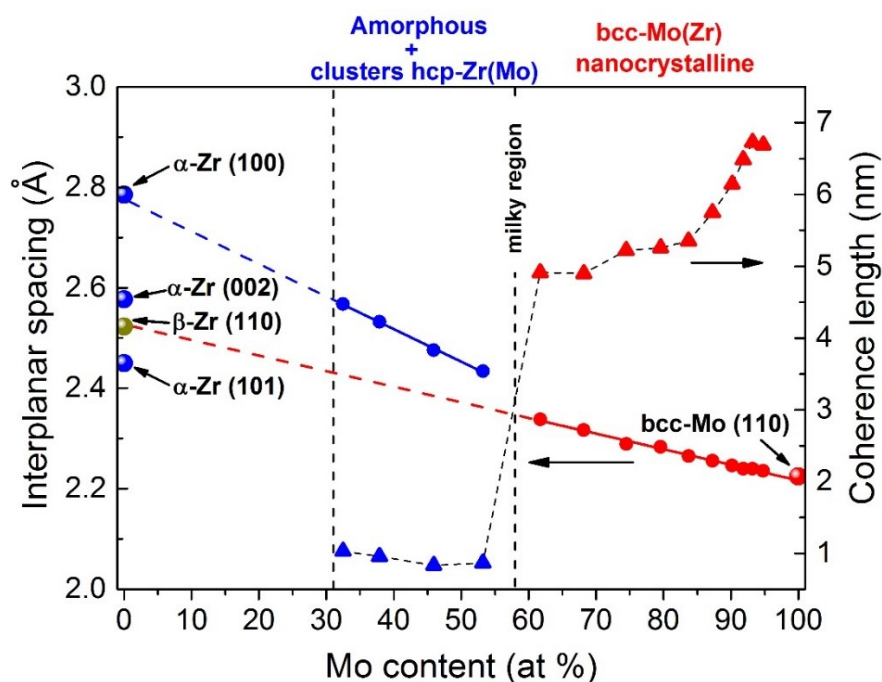
Figure 3.3. Dependency of the interplanar spacing and the coherence length with the Mo content.

3.3 Crystalline side

As previously mentioned, the X-ray diffractograms for samples with Mo content between 62 and 95 at% are typical of a crystalline structure, showing well defined diffraction peaks as can be seen in Figure 3.4(a). The crystalline structure was verified with TEM images made to these samples. For instance, in Figure 3.4 (b) the HRTEM image and its corresponding FFT pattern is shown for one of these samples (62 at% of Mo). The diffraction peaks can be ascribed to the bcc lattice of Mo, although they are shifted with respect to those of pure Mo. The shift of the peaks is reflected in the increase of the inteplanar spacing (extracted from the FSDP) when the Zr content increases, as can be seen with red circles in Figure 3.3. There is a linear dependency between the inteplanar spacing and the Mo (or Zr) content and its extrapolation goes from the interplanar spacing of the (110) planes of the bcc structure of Mo (ICDD 04-014-7435) to the interplanar spacing of the (110) planes of bcc-β-Zr (ICDD 01-071-3958). This behavior is typical of a solid solution, in this case of Zr in the bcc lattice of Mo. Thus, the shift of the peaks is due to the incorporation of Zr into Mo lattice, as the Zr atomic radius (1.62 Å) is higher than the Mo (1.36 Å) one [68]. Taking into account the above and considering the coherence length values (~5-7 nm) shown with red triangles in Figure 3.3, we can conclude that
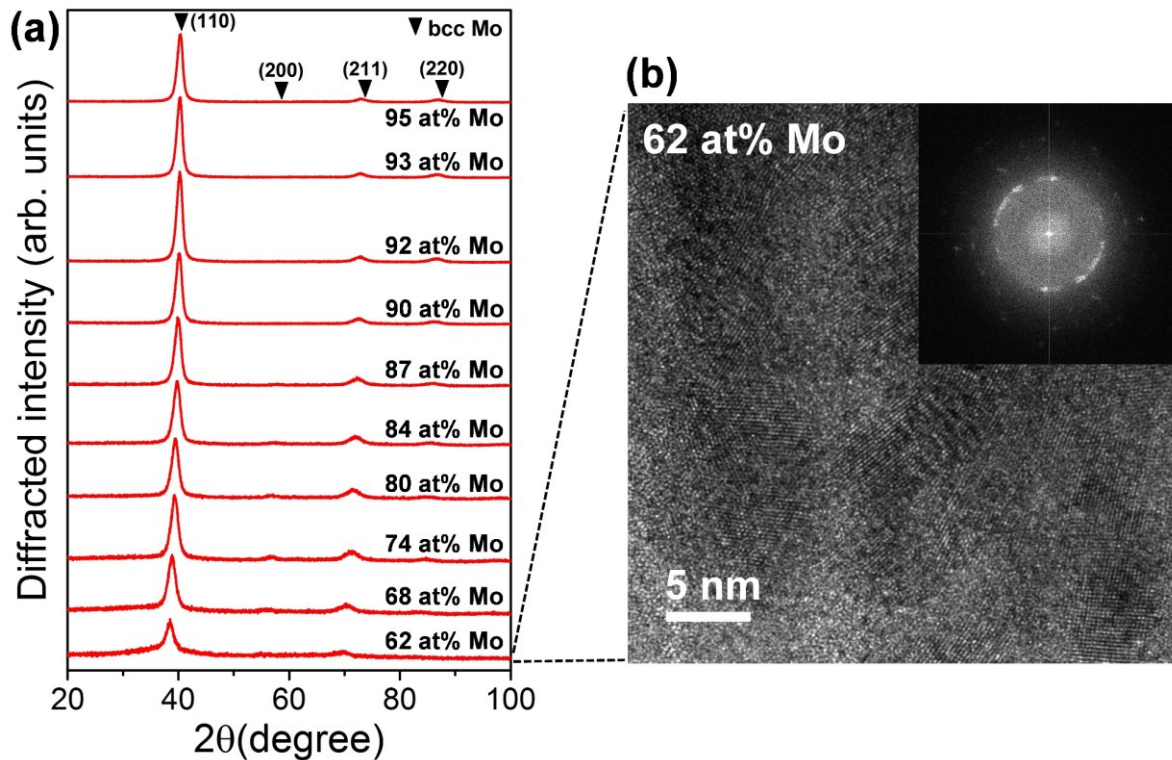
Figure 3.4. X-ray diffractograms (a) and HRTEM image with its corresponding FFT pattern (b) of sample with 62 at% Mo.

in this range of compositions (from 95% to 62% Mo content) the samples are nanocrystalline solid solutions of zirconium in the bcc lattice of molybdenum, bcc-Mo(Zr) nanocrystalline.

3.4 X-ray amorphous side

From 53 at% to 32 at% Mo, the structure of the samples is different from the previous one. The X-ray diffractograms acquired from these samples (see Figure 3.5(a)) are similar, with a characteristic wide peak and a second broader halo that are representative for the amorphous state. Also, FFT analysis performed on these samples (see Figure 3.5(c)) confirms their amorphous character.

However, amorphous does not necessarily mean a randomly ordered solid. Although the long-range order that characterizes crystalline metals is not present in amorphous alloys, some degree of short- and medium-range order do exist [69–72], which is due in part to their high atomic packing density. The polytetrahedral or cluster packing model is well accepted as a description of the short-range order (SRO) in metallic glasses [73]. These clusters are composed of an atom and its nearest-neighbor shell. To form these clusters the atoms are accommodated
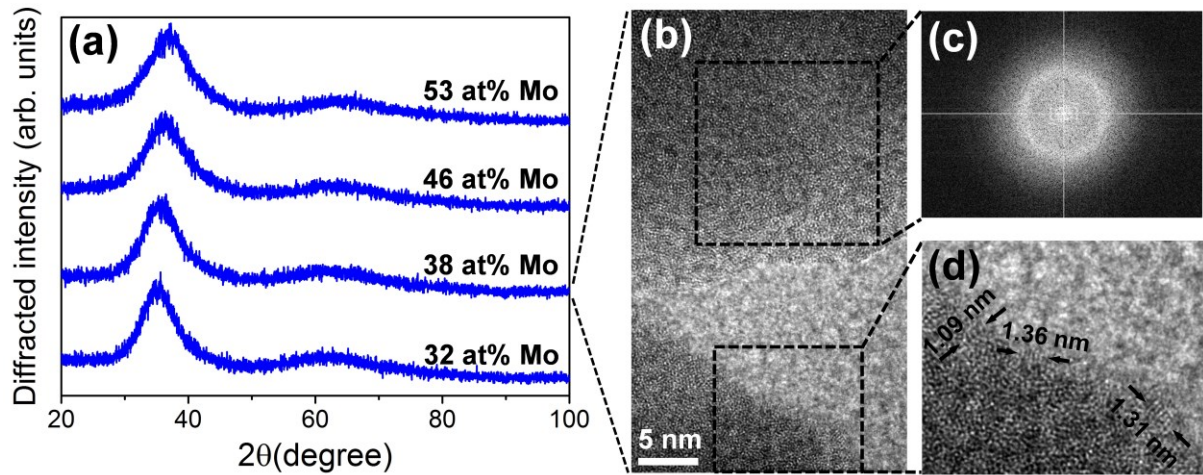
Figure 3.5. (a) X-ray diffractograms from sample with 32 at% to sample with 53 at% of Mo. HRTEM image (b) and FFT (c) of the sample with 38 at% of Mo. (d) Zoom made to the TEM image shown in (b) showing the existence of small crystalline-like regions.

in order to maximize the packing efficiency. The different types of polytetrahedrons that can be formed have been carefully studied and it is well known that for a given coordination number there is a type of cluster, the so-called polytetrahedral Z-cluster, with the highest compactness [73]. The Z-clusters can be distorted and other types of polytetrahedrons (with a lower compactness) can be formed. A given metallic glass is formed by the Z-cluster and their distorted versions but with a tendency to maximize the most compact Z-clusters. A critical parameter that determines the predominant Z-cluster type present in a given glass is the effective atomic size ratio and therefore the compositions of the glass. Even though the polytetrahedral clusters are the fundamental building blocks of the SRO in metallic glasses, how these clusters are connected and arranged to form the medium-range order (MRO) is still an outstanding question in metallic glass research. For example, the efficient cluster packing (ECP) model [69,70] can be a good approach to the MRO. Other authors have suggested that the MRO in bulk metallic glasses may be characterized by a self-similar, fractal packing of atomic clusters [72] and recently has been proven that this fractal behavior is present also in thin film metallic glasses [67].

Therefore, although at first sight the X-ray diffractograms appear very similar, they do not reflect similar local structures. Actually, the position and FWHM of the FSDP are changing

with the composition. We can see in Figure 3.3 the dependencies of the coherence length (blue triangles) and the interplanar spacing (blue circles) with the Mo content, both extracted from the FSDP. The coherence length values are between 0.8 and 1.5 nm, which is in accordance with the medium-range length scale in metallic glasses [72], indicating that some atomic organization exists at this scale. Indeed, TEM analysis made to the sample with 38 at% Mo (see Figure 3.5(b)-(d)) shows small crystalline-like regions whose dimensions are similar to that of the coherence length. In fact, this crystalline organization at the MRO has been previously observed in other metallic glass systems [74,75]. In Ref. [76] the presence of a local translational symmetry (LTS) in different metallic glass systems was explored and the authors stated that the LTS has a one-dimensional translational order. This last factor is in agreement with the elongated form of the small crystalline regions observed in Figure 3.5(c). This does not mean that the atomic organization at the MRO is crystalline-like but indicates that it is possible to have in amorphous structures small regions where is favorable the formation of a crystalline-like atomic organization. On the other hand, the behavior of the interplanar spacing (see Figure 3.3) resembles the Vegard's law involved in metallic crystallized systems (as happens in the crystalline side in our samples). In fact, Figure 3.3 shows that the extrapolation of the interplanar spacing goes to the interplanar spacing of the (100) planes of the hcp structure of Zr, as in a solid solution of Mo in the Zr structure. Therefore, it is plausible that, at the local level, the films have the same order as a solid solution of Mo in the hcp structure of Zr, and there may be small crystalline-like regions or "clusters" (not to be confused with the polytetrahedral clusters) with this organization. Then, we can propose with confidence that between 53% and 32% Mo content the samples are amorphous with the presence of clusters with a hcp-Zr(Mo) organization.

3.5 Mechanical properties

In the previous sections has been shown how the structure of Zr-Mo thin films evolves with the composition. This section is focused on the mechanical properties of the films (hardness H, Young's modulus E and friction coefficient) and their relation with the structural evolution.
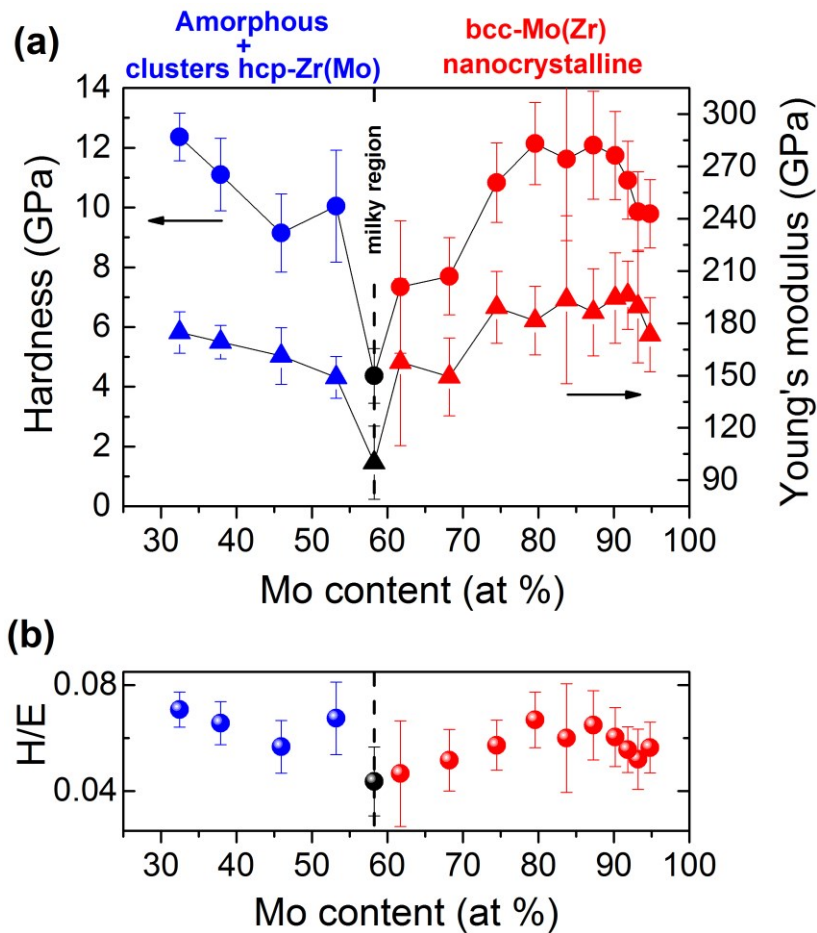
Figure 3.6. (a) Evolution of the hardness and Young's modulus of Zr-Mo thin films as a function of the Mo content. (b) *H/E* ratio as a function of the Mo composition.

Figure 3.6(a) shows the evolution of *H* and *E* as a function of the Mo content as extracted from nanoindentation measurements. The values for *H* are in the 4-13 GPa range, depending on the chemical composition, and in all cases are much larger than the *H* values of bulk pure Zr (~1.5 GPa) and bulk pure Mo (~2.3 GPa). Meanwhile, the values of *E* are in the 100-200 GPa range and are kept between the bulk Young's modulus values of Zr (~100 GPa) and Mo (~330 GPa). This combination of high *H* while *E* is kept in the values range of the metals leads, consequently, to high values of the *H/E* ratio, as is shown in Figure 3.6(b). In all cases, the *H/E* values are between 0.04 and 0.08. This makes the Zr-Mo system a coating candidate with a good wear resistance [66]. The results presented in Figure 3.6 indicate that films with 32 at% Mo in the X-ray amorphous side and 80 at% Mo in the crystalline side exhibit the best mechanical properties in the Zr-Mo system. We point out here that in the "milky region" the mechanical properties deteriorate, i.e. the hardness and the *H/E* ratio have a minimum.
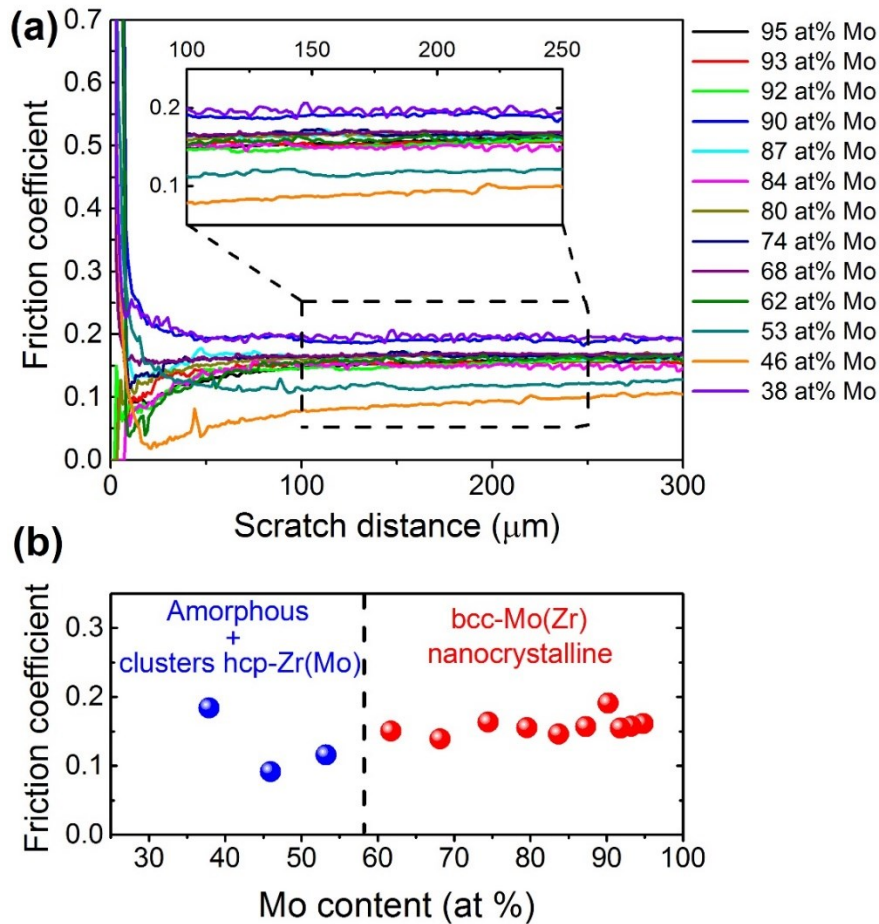
Figure 3.7. (a) Friction coefficient of sputter-deposited Zr-Mo films during microscratch experiments. The inset shows a zoom between 100 and 250 mm of the scratch distance. (b) Dependency of the friction coefficient to the molybdenum composition obtained averaging, for each sample, the values of friction between 100 and 250 mm of the scratch distance.

However, they are still higher compared to those of pure Zr and pure Mo. In addition, as will be shown in the next chapters, other properties emerge in this region which make it special.

Figure 3.7(a) shows the evolution of the friction coefficient for all the Mo contents studied during a microscratch with increasing applied load. For each sample, four friction measurements were made and averaged. In Figure 3.7(b), the dependency of the friction coefficient to the Mo content is presented. This dependency was obtained averaging, for each sample, the values of friction between 100 and 250 mm of the scratch distance (inset of Figure 3.7(a)). The friction coefficient values for all the samples were below 0.2. These low values of the friction are in agreement with the high *H/E* ratio.
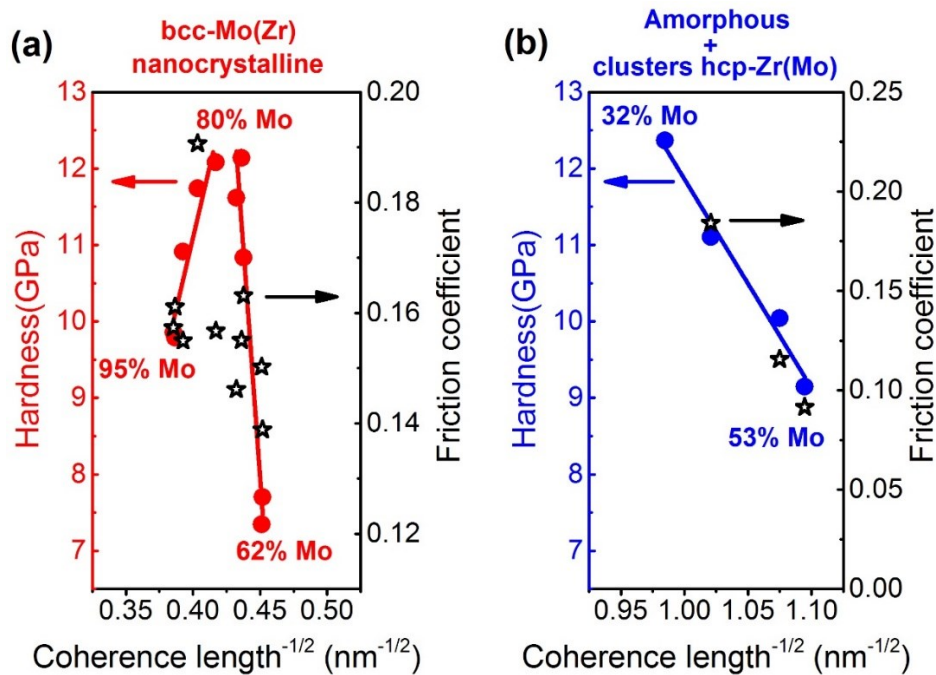
Figure 3.8. Dependency of hardness and friction coefficient with the reciprocal square root of the coherence length for films in the nanocrystalline bcc side (a) and in the X-ray amorphous side (b).

The high hardness values of the samples in the crystalline side could be explained by the intense Hall-Petch hardening [77] due to the very small values of coherence length in the films studied. In Figure 3.8(a) is shown the relation between hardness and the reciprocal square root of the coherence length in the crystalline side. As we can see, from 95 to 80 at% Mo the classical Hall-Petch relation is fulfilled and the hardness reaches a maximum for a coherence length of approximately 6 nm while from 80 to 62 at% Mo the Hall-Petch relation breaks down and the inverse Hall-Petch effect appears, that is, the hardness decreases when the coherence length decreases.

On the other side, the structural-mechanical properties relation in the X-ray amorphous side is more difficult to elucidate. As is shown in Figure 3.6, both H and E decrease with the increase of the Mo content, having a minimum in the "milky region". We note that the H values in the amorphous side can be higher than in the crystalline side, even when the Mo content (with a higher H value in the bulk pure state) is higher in the crystalline side. Indeed, the highest hardness is that of sample with the lowest Mo content (32 at%).

The hardness behavior can be understood in terms of relative presence of Z-clusters, with a higher compactness, and of highly distorted Z-clusters or "geometrically unfavored motifs" (GUMs) [78,79], with a lower compactness. Which Z-clusters are favored depends on the relative atomic size of the constituent elements and therefore on the composition. Although the atomic organization for a particular composition in any given metallic glass is such that it tends to maximize the presence of Z-clusters in order to keep the high atomic packing density, these locally favored structures are accompanied by a range of GUMs needed to fill the 3D space. GUMs are clusters with a lower stability (soft spots) as compared to the compact Z-clusters and are more susceptible to deformation [78,79]. For example, in the Cu-Zr system the highest hardness and Young's modulus are reached in $Cu_{0.64}Zr_{0.36}$, that is known as the composition with a highest quantity of full icosahedron (polytetrahedral Z-cluster with coordination number 12) and therefore is the most densely packed composition [80]. In our case, although we do not know the type of Z-cluster that dominates for each composition, the H and E measurements indicate that compositions closest to the "milky region" are dominated by GUMs. At the same time, sample with 32 at% Mo has the composition for which a higher density of Z-clusters is present.

In Figure 3.8(b) is shown the dependency of H to the reciprocal square root of the coherence length in the amorphous side. The figure shows that H decreases when the coherence length decreases as in the inverse Hall-Petch effect, and the dependency between H and the reciprocal square root of the coherence length seems to be linear. The increase of H with the coherence length could be understood if the latter is interpreted as the mean value of the medium-range length scale. In this sense, a higher coherence length implies larger domains formed either by well connected Z-clusters or by the crystalline-like regions that were shown in the previous section, which decrease the presence of GUMs. Consequently, higher coherence length implies less GUMs and therefore higher hardness values.

Finally, Figure 3.8 shows, with star symbols, the dependency of the friction coefficient to the coherence length. In the nanocrystalline side, the friction coefficient seems to be characterized by two regimes corresponding to those of the hardness. Nevertheless, the empirical H/E ratio criterion fails at predicting the evolution of the friction coefficient in this

case as higher *H/E* is associated to higher friction. We can suggest that the deformation mechanisms play the major role in the evolution of the friction. Indeed, a transition from Hall-Petch to inverse Hall-Petch can be the signature of change in deformation mechanism and softening of the material. In the amorphous side, the friction is proportional to the hardness. Both hardness and friction evolutions can be interpreted as a change in the density of GUMs that soften the material.

3.6   First approach to the "milky region"

So far, we have shown that a transition from a crystalline to an amorphous structure occurs in sputter-deposited Zr-Mo thin films. We also shown that the region of transition exhibit a change in appearance (a milky-like appearance). The phases present throughout the film, as well as the presence of the "milky region" are illustrated in the upper panel of Figure 3.9. However, the structure in the "milky region" has not been clarified. The only information that we have is the TEM image extracted from this region and shown in Figure 3.2(b). The FFT pattern in the inset of the figure shows only a diffuse halo, indicating that the structure of the "milky region" is amorphous. Nevertheless, a more carefully analysis of the structure in this region, which will be shown in the next chapter, reveals that the amorphous phase is not the only phase present in the "milky region". Actually, two different phases are coexisting in this region. The fact that the information extracted from the TEM analysis is not complete is due to the way in which the sample was collected (by scratching the film surface onto the TEM grid).

A first insight at the surface morphology of the "milky region" is provided in the bottom panel of Figure 3.9. The SEM top-views sequence shown in the figure reveals that the surface morphology in this region is changing significantly with composition. Effectively, looking from left to right (which means that we are moving towards regions with a higher Mo content), the number of zones that exhibit a rounded shape seems to increase until they cover the whole film surface. Is it possible to describe the kinetics of this process? What is the nature of the "milky region"? Is it something particular in the Zr-Mo system or can it be extended to other systems? Which properties of the film can be exploited due to the presence of the "milky region"? All
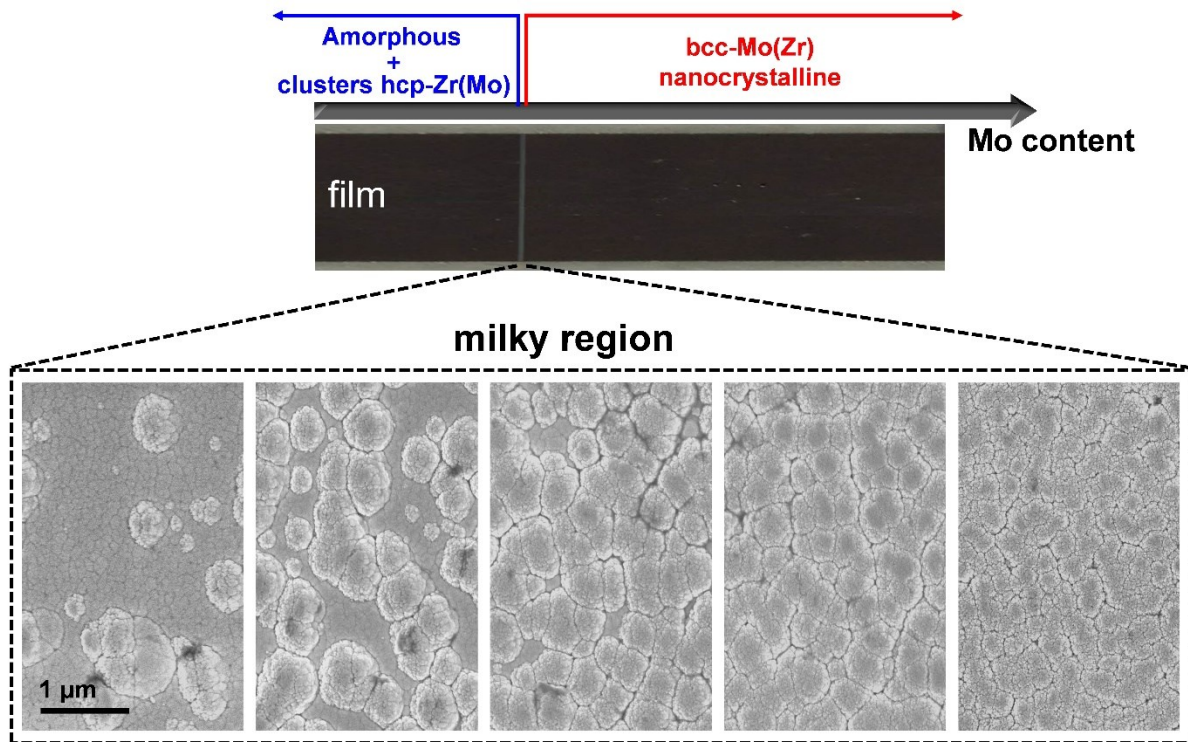
Figure 3.9. Upper panel: schematic showing the phases present throughout the film. Bottom panel: SEM top-views sequence along the "milky region" (from left to right).

these questions, among others, will be addressed in the next chapters and constitute the core of this thesis.

3.7 Chapter conclusions

This chapter provides a first insight to the Zr-Mo system. Using a combinatorial approach, it was possible to synthesize Zr-Mo thin films by co-sputtering in a wide range of compositions. We showed, using X-ray diffraction and transmission electron microscopy that a transition from a crystalline to an amorphous structure occurs in this system, depending on the composition. The evolution of the structural and the mechanical properties with composition can be summarized as follow:

- Films with a composition ranging from 62 to 95 at% Mo exhibit a crystalline structure, more particularly, a nanocrystalline solid solution of Zr in the bcc lattice of Mo. The small values of coherence length (between 5 and 7 nm) favor the Hall-Petch hardening, which is evidenced in the high hardness values (between 7.3 and 12.1 GPa) of the samples in this

range of compositions. Meanwhile, the Young's modulus values (between 150 and 200 GPa) are kept between those of the two bulk metals. Consequently, high values of the *H/E* ratio were found. The best combination of hardness (12.1 GPa) and *H/E* ratio (0.07) was that of film with 80 at% Mo. The films also exhibit low values of the friction coefficient. An inverse Hall-Petch effect is observed for coherence length lower than 6 nm.

- Films with a composition ranging from 32 to 53 at% Mo exhibit an amorphous structure. At the local level (length scale of the medium-range order in metallic glasses, i.e., ~0.6-2 nm), the amorphous structure exhibits the same local order as a solid solution of Mo into hcp Zr, and there may be small crystalline-like regions with this organization. The hardness values are high (between 9.1 and 12.4 GPa) while the Young's modulus values (between 150 and 175 GPa) are kept between those of the two bulk metals. The film with 32 at% Mo exhibit the higher values of hardness and *H/E* ratio (0.07). Interestingly, an increase of the hardness with the coherence length was observed that can be associated to the presence of less geometrically unfavored motifs (GUMs).

Hence, the constitutive phases obtained within the explored composition range are supersaturated nanocrystalline and amorphous solid solutions. This contrasts with the stable equilibrium phase diagram that contains (Mo) and (Zr) solid solutions of limited solubilities and one intermetallic Laves_c15 phase of $ZrMo_2$ composition. It is to be noted that the $ZrMo_2$ Laves phase was never observed in our Zr-Mo films neither using XRD nor using high resolution TEM. This is in line with the concept that the difficulty to form intermetallic phase of complex structure, due to high quenching rates associated to vapor condensation, favors the solid solution.

Finally, a region with a milky-like appearance forms, which has an intermediate composition to those of the amorphous and crystalline sides. The explanation behind the occurrence of this region is the motivation for the next chapter.

Chapter 4

Controlling surface morphology by nanocrystalline/amorphous competitive self-phase separation in thin films: Thickness-modulated reflectance and interference phenomena
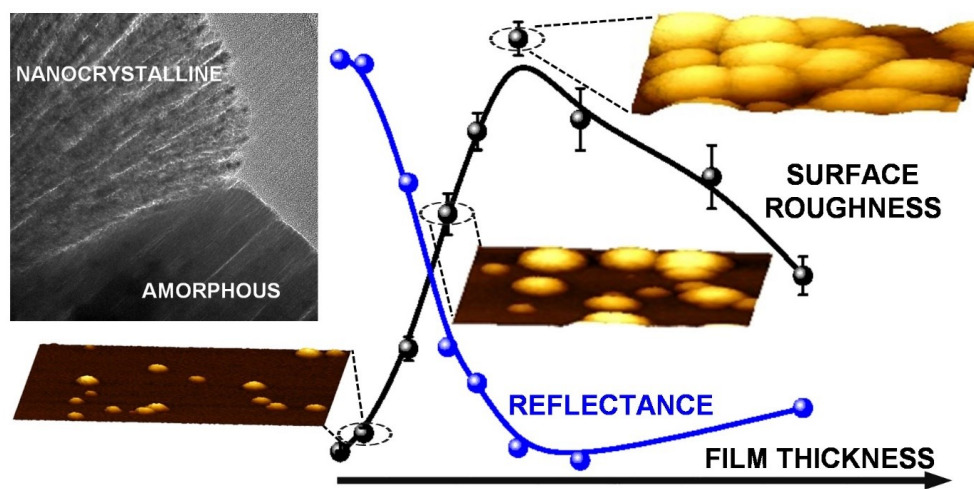
ABSTRACT: In this chapter, we demonstrate that a self-separation of a nanocrystalline and an amorphous phase occurs in sputter-deposited Zr-Mo thin films obtained at compositions intermediate to those necessary to form single-phased amorphous and nanocrystalline films. We explore the possibility of controlling the surface morphology features of these films using the competitive growth between the two phases. The evolution of the residual stress with the thickness at the biphased composition is correlated with the morphology evolution. In addition, a possible mechanism for the self-separation of phases is presented. The particular geometry in which the nanocrystalline phase in competition with the amorphous phase grows made possible to change the surface morphology of the films at the biphasic composition by changing the film thickness. In this way, it was possible to control the surface roughness and, because of this, tuning the film reflectance at a determined wavelength. We show that the self-separation of phases as presented here is not limited to Zr-Mo alloys and can be extended to other systems.

Contents

4.1 Introduction

The fabrication of new functional surfaces plays an important role in the development of the modern industry. Many efforts have been made in order to modify and control the surface morphology of a variety of materials by using different techniques [81–84]. The functionalities of surface modified materials are wide: controllable wettability [85,86], biomedical applications [87], solar cells [88], among others. Phase separation phenomenon is widely observed in thin films and has been thoroughly studied in order to manipulate the resulting functional properties. Different configurations could be obtained, such as the nanodispersion of metal or ceramic particles in a ceramic matrix [89,90]. Alternatively, thin films showing lateral self-separation of ceramic phases could be obtained in case of specific epitaxial relationships between phases or between at least one phase and the substrate [91–93]. Apart for some specific cases (see for instance [94,95]), the topography of the film surface has scarcely been reported to be markedly affected by the phase separation. To the best of our knowledge, surface morphology modification induced by phase separation has not been exploited so far to manipulate the functional properties.

In the previous chapter was shown that in sputter-deposited Zr-Mo thin films, a structural transition from an amorphous to a nanocrystalline phase occurs around 60 at% Mo. The transition region appears as a singularity in the optical properties within the explored compositions, showing a milky-like appearance. In this chapter, we propose to delve into the nature of the so-called "milky region". We demonstrate that a competitive self-separation of an amorphous and a nanocrystalline phase occurs for Zr-Mo thin films obtained at a composition intermediate (around 60 at% Mo) to those necessary to form single-phased amorphous and nanocrystalline films. Residual stress measurements, often used on single metallic elements, are used here for explaining the dynamical growth with thickness of Zr-Mo films obtained at the biphased composition, proving the usefulness of this technique when studying microstructures that are more complex. Moreover, we show that, because of the phase separation, the surface morphology can be modulated. In this way, the surface roughness, largely known to influence the scattered light [59,60,62], can be tuned and, consequently, a thickness-controlled reflectance is achieved.
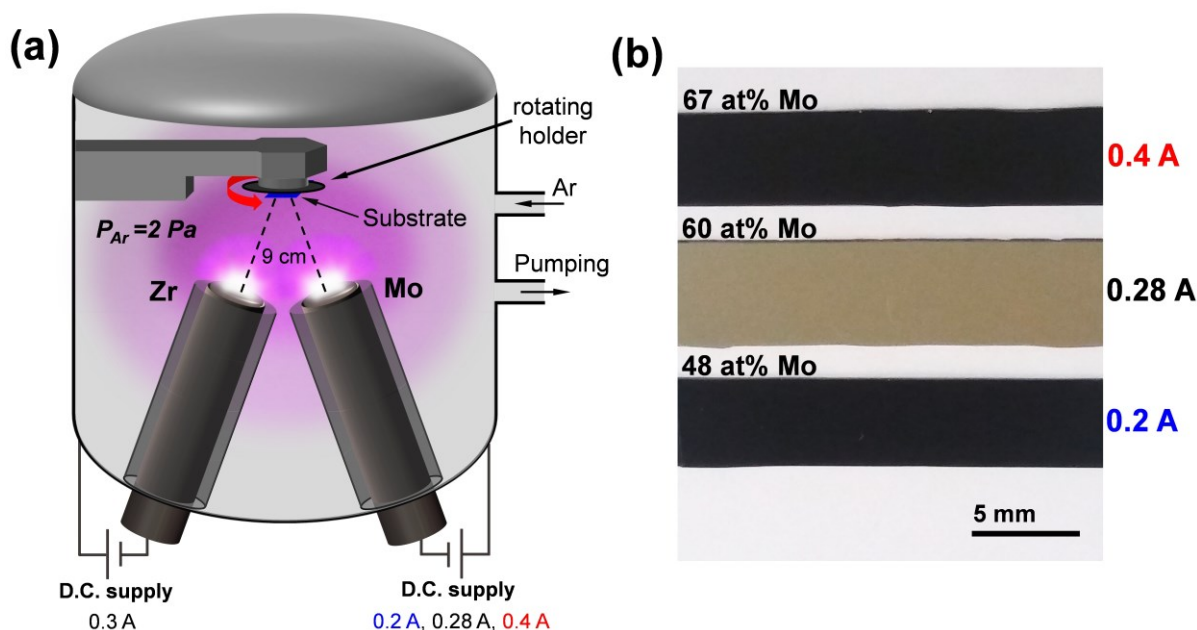
Figure 4.1. (a) Schematic of the sputtering chamber showing the parameters used during the films deposition. (b) Optical image of deposited films showing the change in coloration of sample obtained with a discharge current of 0.28 A applied to the Mo target.

4.2 Nanocrystalline/amorphous self-phase separation

A schematic of the sputtering chamber together with the parameters used during the growth of the films is presented in Figure 4.1(a). In order to ensure the homogeneity of the films, all the depositions were made with the substrate holder in rotating mode. Note that, unlike the previous chapter, the composition of the films was controlled by changing the discharge current applied to the Mo target (0.2, 0.28 and 0.4 A), keeping constant the discharge current applied to the Zr target (0.3 A). It resulted in Zr-Mo thin films of thickness around 1500 nm containing 48, 60 and 67 at% Mo, respectively. The optical image of the films shown in Figure 4.1(b) evidences the difference in appearance of the film with 60 at% Mo, corresponding to the composition of the "milky region" referred in the previous chapter. X-ray diffractograms performed to these films are provided in Figure 4.2(a). In line with the previous chapter, XRD data clearly indicate the possibility to modify the structure in the range of compositions explored. In more details, the signature of nanocrystalline bcc Mo is obtained for the highest Mo content (peaks are shifted with respect to pure Mo due to the incorporation of Zr atoms of larger atomic radius than Mo) and a wide diffraction signal corresponding to amorphous or
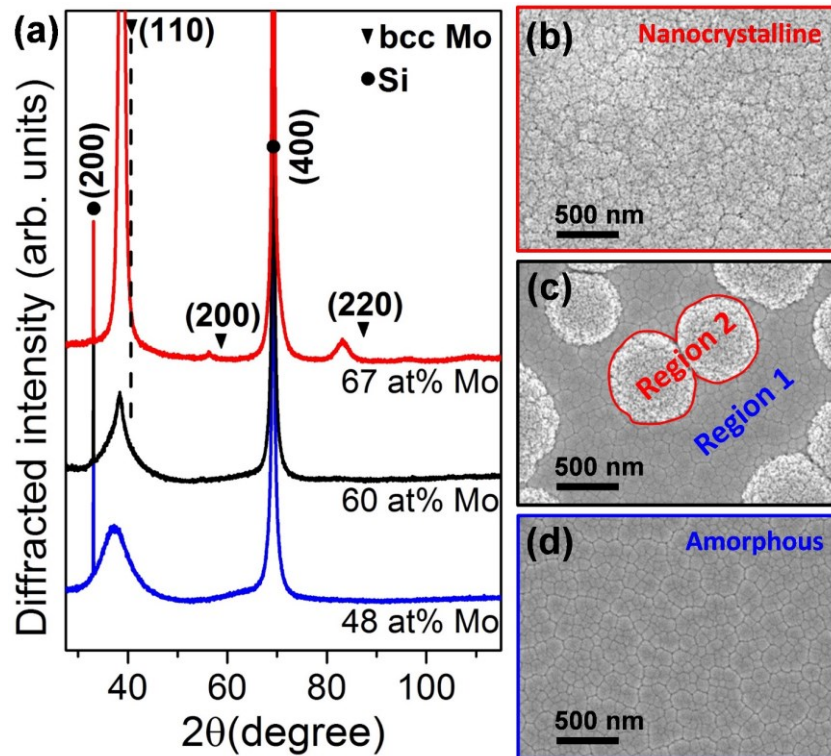
Figure 4.2. Morphology and structure of the films. (a) X-ray diffractograms of samples grown at different currents applied to the Mo target: blue line (0.2 A), black line (0.28 A) and red line (0.4 A). (b)-(d) Top-view SEM images corresponding to samples shown in (a).

ultrafine-grained phase is obtained for the lower Mo content. At the intermediate composition, a mixture of both signals is obtained, indicating that the microstructure of the "milky region" is a mixture of the amorphous and nanocrystalline phases, as was already advanced in the previous chapter.

In general, in absence of specific epitaxial orientation between the deposited phases and the substrate and without intentional thermal assistance, biphased coatings deposited using PVD methods consist of a matrix with nanodispersion of a secondary phase. Formation of such nanocomposites is driven both by thermodynamics and kinetics, and the very high cooling rates associated to the condensation of the gas phase using PVD methods play an important role in nanodispersing the secondary phase. In the present case, a careful investigation of the film morphology reveals a different situation. In Figure 4.2(c) is shown a SEM top-view image of the sample with 60% of Mo content. The image shows two regions with different morphologies: region 1 that is more flat and acts as a matrix embedding region 2 that is composed by zones of rounded shape. At the local scale, the surface morphology of the region 1 is similar to that of
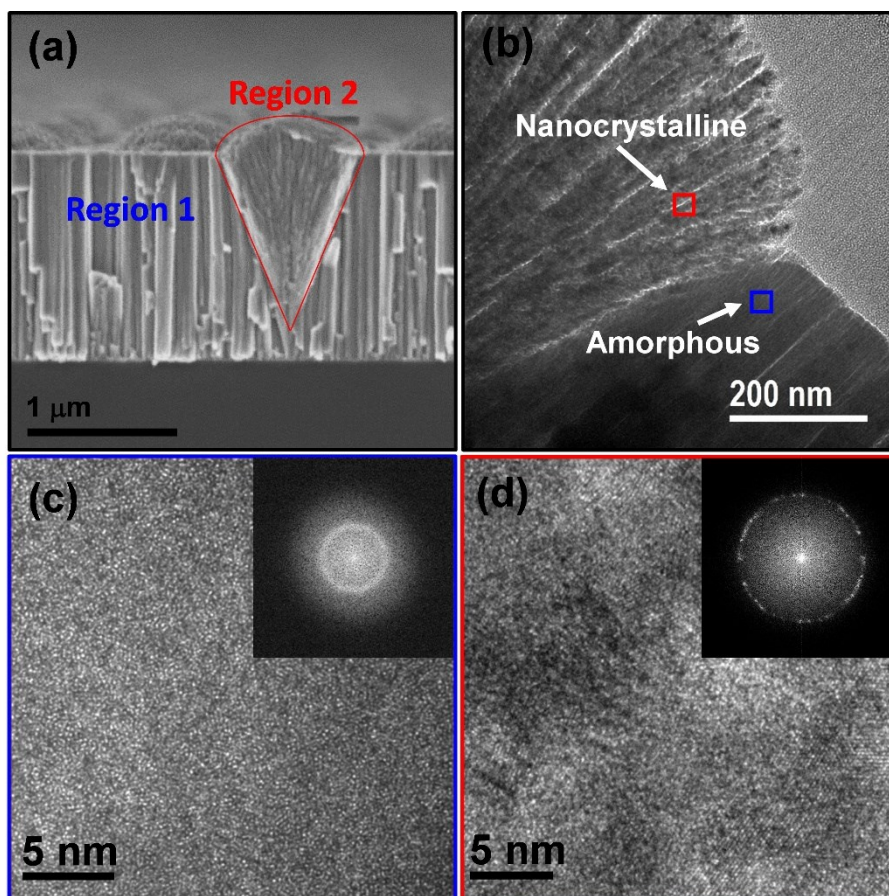
Figure 4.3. SEM (a) and TEM (b) cross-sectional images of sample shown in Figure 3.1(c). (c) HRTEM image and FFT from the region highlighted with a blue square in (b). (d) HRTEM image and FFT from the region highlighted with a red square in (b).

the amorphous film of lower Mo content (see Figure 4.2(d)), while the surface morphology of region 2 resembles that of the nanocrystalline film of higher Mo content (see Figure 4.2(b)).

Figure 4.3(a) shows the cross-sectional view of the biphased sample and evidences that the shape of region 2 is conical inside the bulk of the film and terminates with a dome whose base is aligned with the surface of region 1. The TEM image of the film shown in Figure 4.3(b) evidences the spatial separation of both regions. To bring further details on the local structure in both regions, HRTEM investigation and their FFT were performed. Figure 4.3(c)-(d) show representative data collected in regions 1 and 2, marked by the blue and red squares in Figure 4.3(b). The HRTEM image of Figure 4.3(c) and diffuse halo in the corresponding FFT confirm the amorphous state in region 1. On the other hand, the HRTEM image of Figure 4.3(d) confirms the nanocrystalline character of region 2 and the interplanar distance corresponding to the well-defined ring in the FFT pattern matches with that extracted from XRD.

In summary, the "milky region" is obtained by working at a composition intermediate between those of the amorphous and the nanocrystalline phases. It is a biphased region in which a self-separation of amorphous and nanocrystalline phases occurs. Thus, the film grows initially amorphous and, for a certain thickness, the nanocrystalline phase nucleates, and both phases continue growing together in competition. The focus of the next sections will be on the intermediate biphased composition, in particular the evolution of the morphology and the properties with the film thickness will be discussed. Throughout this thesis, the terms "milky region", nanocrystalline/amorphous self-phase separation or nanocrystalline/amorphous competitive growth will be used to refer to the same phenomenon.

4.3 Stress evolution with thickness

In order to study how the morphology and the properties of the biphased composition (60 at% Mo) evolve with the film thickness, several samples were grown under the same deposition conditions, but changing the deposition time. The thickness of the films obtained as a function of the deposition time is shown in Figure 4.4(a). A constant deposition rate of 24 nm/min was kept during all the depositions. The X-ray diffractograms shown in Figure 4.4(b), evidence that the signal of the peaks associated to the nanocrystalline phase is growing with the increase of the thickness. This means that the ratio between the nanocrystalline and the amorphous phase is increasing with thickness, which is due to the particular geometry (a conical shape of the nanocrystalline phase inside the bulk of the film as can be seen Figure 4.3(a)-(b)) resulting from the competitive growth between both phases.

Figure 4.5(a) shows the evolution of in-plane residual stress state of the film with thickness determined using the Stoney equation (eq. (2.4)). From the figure, three different zones can be identified. First, the stress increases (becomes less compressive) with thickness in zone 1, a decrease of the stress level is evidenced in zone 2 and, finally, it stabilizes in zone 3. Figure 4.5(b) shows the dependence with thickness of the surface coverage by the nanocrystalline phase extracted from the analysis of SEM images (see Appendix section for details). The inset in Figure 4.5(b) shows the dependency of the stress with the surface coverage in the three zones already mentioned and typical top and cross-sectional SEM images from each zone are shown
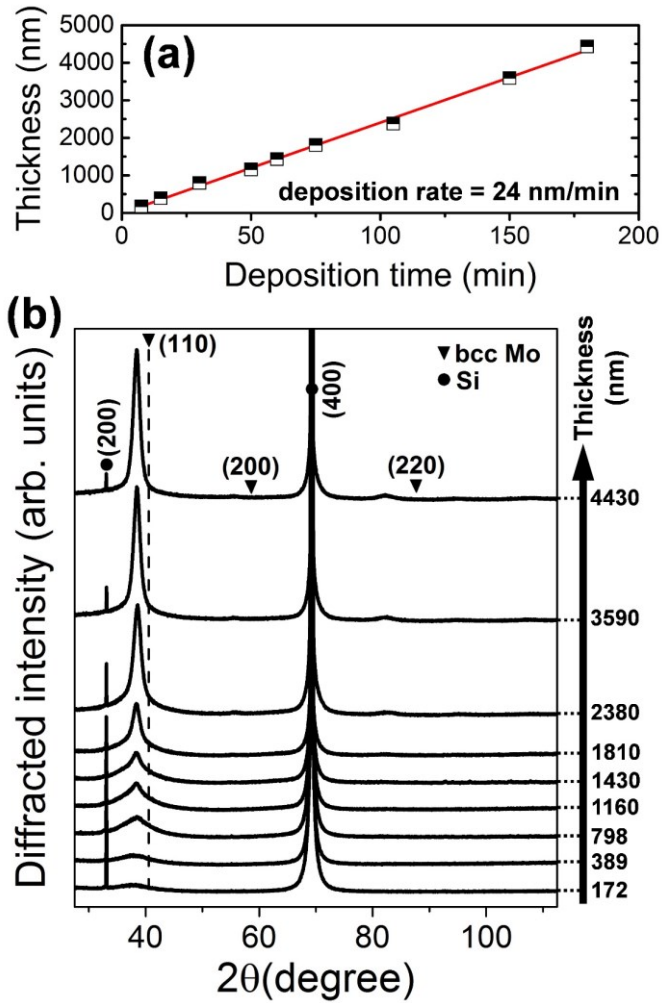
Figure 4.4. (a) Evolution of the film thickness with the deposition time of biphased films (60 at% Mo) showing a constant deposition rate of 24 nm/min. (b) X-ray diffractograms of biphased films grown at different thicknesses.

in Figure 4.5(c). From Figure 4.5(b) we can estimate to 162 nm the thickness at which the nucleation of the nanocrystalline phase starts, assuming that the coverage-thickness dependence follows an exponential law. A schematic of the morphology evolution with the thickness together with the stress in each zone is shown in Figure 4.6. The stress evolution can be interpreted as follows:

Zone 1 (surface coverage below 15%): In this zone, the nanocrystalline regions start to nucleate and grow without touching each other. As the thickness increases, the stress becomes less compressive, i.e. a tensile component of the stress develops due to the growth of the nanocrystalline regions. This can be understood by taking in consideration that the growth of

60
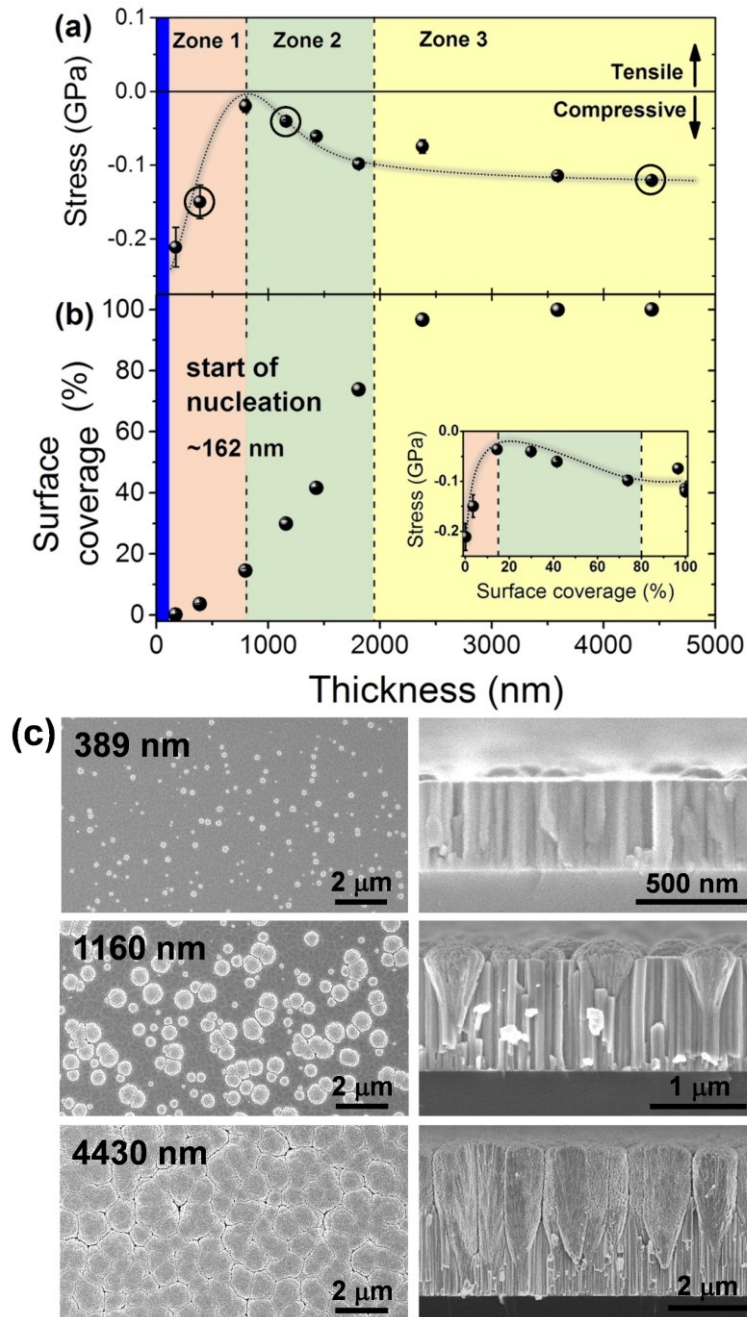
Figure 4.5. Evolution of residual stress (a) and surface coverage by the nanocrystalline phase (b) with the increase of the films thickness at the biphased composition (60 at% Mo). The inset in (b) shows the dependency of the stress with the surface coverage. Three different zones can be identified and top (left) and cross-sectional (right) SEM images representative of each zone are shown in (c).

the crystalline phase can induce a volume contraction of the film, causing an increase in the tensile stress [96,97].
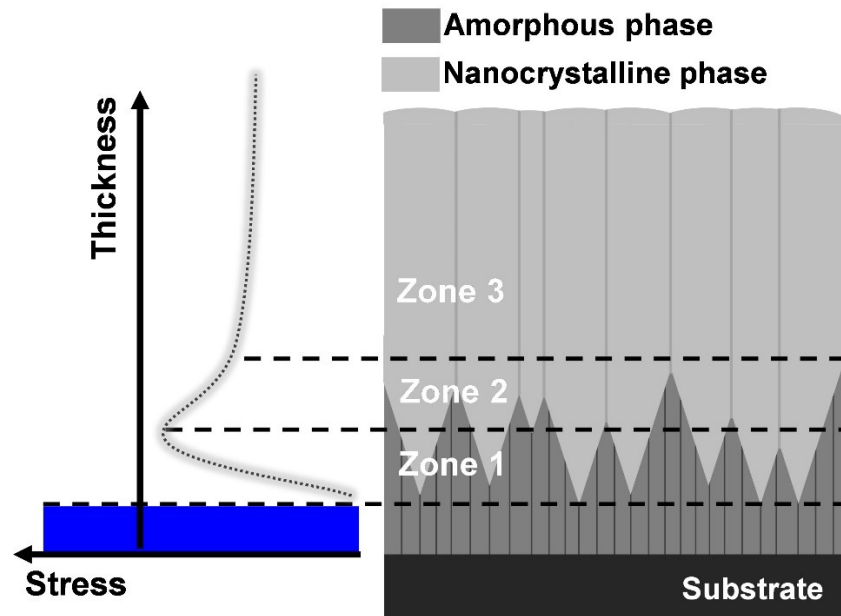
Figure 4.6. Schematic showing the evolution with thickness of the film morphology and the stress.

Zone 2 (surface coverage between 15% and 80%): This zone is dominated by the coalescence of the nanocrystalline regions. A better look at the microstructure of the nanocrystalline regions shows that they are composed of nano-columns that grow from their axis in a feather-like morphology (see, for example, Figure 4.3(b)). When two neighboring crystalline regions contact, the growth of the nano-columns in the in-plane direction is inhibited. Thus, the impingement of two nanocrystalline regions create a repulsive force between them as indicated by the arrows of Figure 4.7(b). We propose that this repulsive force is the responsible of the increase in the compressive stress in zone 2.

Zone 3 (surface coverage above 80%): Almost all the surface is covered by the nanocrystalline phase. Consequently, the driving mechanism for the compressive stress increase observed in zone 2 is interrupted and the stress stabilizes at a constant value.

Stress and microstructure evolutions have been explained from the moment when the nanocrystalline phase starts to nucleate (for thicknesses higher than approximately 162 nm). For a thickness lower than 162 nm, marked as a blue domain in Figure 4.6(a) and Figure 4.6, the whole film is amorphous and, therefore, the surface morphology is not markedly affected by a change of the film thickness. Nevertheless, the conditions for starting the nucleation of the nanocrystalline phase are defined in this zone. Because of this, an explanation of the possible path for the nucleation will be presented in the following.
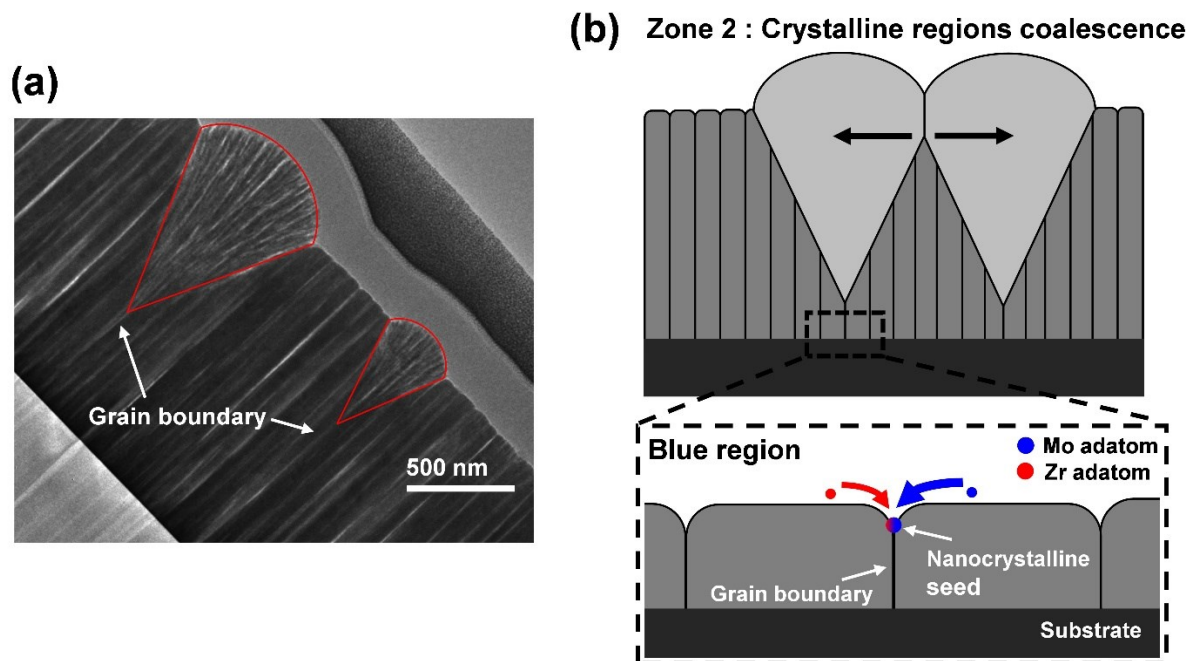
Figure 4.7. (a) TEM cross-sectional image of the film showing nanocrystalline regions growing from the boundaries between adjacent columns. (b) On top, the generation of compressive stress by the impingement of two nanocrystalline regions is presented. The black arrows indicate the sense of the repulsive force that appears when two neighboring crystalline regions are touching each other. At the bottom is shown the migration of the adatoms from the surface to the grain boundary. The bigger blue arrow compared with the red one means more Mo atoms going to the grain boundary.

4.4   Possible path for the nanocrystalline/amorphous self-phase separation

First of all, we want to point out that the temperature measured at the substrate did not exceed 45 °C, even after 3 hours of deposition (see Figure 4.8). The nucleation of the nanocrystalline phase begins within the first 10 minutes of deposition during which the substrate temperature increase is negligible. Hence, we can discard the change in temperature as the main origin of the nucleation of the nanocrystalline phase.

Figure 4.7(a) shows a typical TEM cross-sectional image of the films. It appears that the nucleation of the nanocrystalline phase starts at the boundaries between adjacent columns. Moreover, as was shown in previous sections, increasing the Mo content, the structure of the
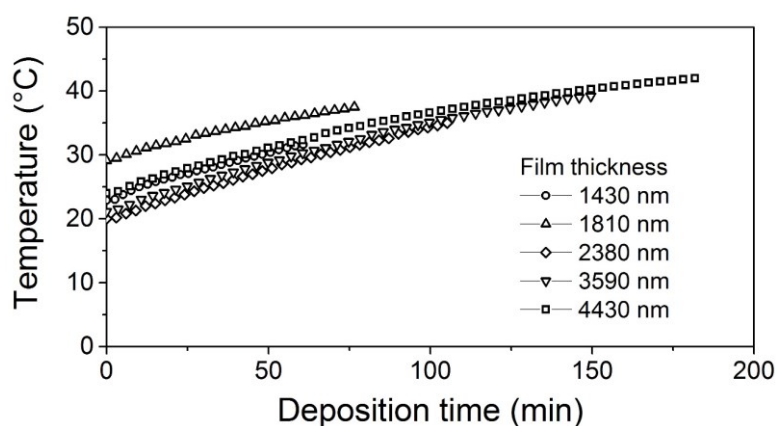
Figure 4.8. Evolution with the deposition time of the temperature measured at the substrate holder for some of the films obtained.

films evolves from an amorphous to a nanocrystalline phase, with both phases coexisting at the biphased composition (see Figure 4.2). This indicates that, besides the possibility to use the interfacial energy available at the grain boundary, the composition is an important factor to trigger the structural transition. Thus, at the biphased composition (60% of Mo content), the favored phase in the initial growth stages is the amorphous one. Nevertheless, if by some mechanism the Mo content locally increases, a local transition to a crystalline structure can occur. This could therefore explain the transition observed when the film thickness reaches 162 nm. To explain this, we take in consideration that the amorphous phase is growing in Volmer-Weber mode, as follows from its columnar structure (see Figure 4.5(c)). In Volmer-Weber type growth, in the post-coalescence regime, when the grain boundaries between islands are created, it is possible to have a diffusion of adatoms from the surface of the islands to the grain boundaries, which depends of the adatom mobility [98–101]. This is due to the difference in the chemical potential between the growth surface and the grain boundaries. In most of the studies dedicated to understand the stress behavior in the post-coalescence regime, single element materials were considered and less information exist about metallic alloy systems. Nevertheless, when two elements with different mobilities are diffusing into the grain boundaries, as in our case, their diffusion rates are generally different, provoking a preferential segregation of the most mobile element at the grain boundaries [102,103]. This means that if, for example, the diffusion from the surface into the grain boundary of the Mo adatoms is higher than that of the Zr adatoms, the Mo/Zr proportion can be increased into the grain boundary,

provoking the nanocrystalline phase nucleation. This process is illustrated at the bottom of Figure 4.7(b), where a bigger blue arrow indicate higher diffusion rate of Mo atoms into the grain boundary. Thereby, the difference in the diffusion rates of Mo and Zr into the grain boundaries could be the mechanism inducing the nanocrystalline phase nucleation.

As previously mentioned, the mobility is an important factor to understand the stress behavior in the post-coalescence regime. The fact the highest value of the compressive stress was obtained at the beginning of zone 1 indicates that such a stress state developed during the growth of the initial amorphous phase (blue zone of Figure 4.6). This is an indication that the adatom mobility was high on this amorphous phase [104,105]. This seems contradictory with the high melting points of Zr (T_m = 2128 K) and Mo (T_m = 2896 K), and the fact that no thermal assistance was used during growth. Nevertheless, as recently shown [106], in the case of amorphous alloys the temperature of reference is rather the glass transition temperature than the melting point. The glass transition temperature at the biphased composition calculated using the model presented in [107] is T_g = 997 K, much more lower than the melting temperatures of Zr and Mo. Hence, we can conclude that the amorphous structure favors the adatom mobility and, thereby, the diffusion of adatoms into the grain boundaries, likely facilitating the nucleation of the crystalline phase.

4.5 Thickness-modulated reflectance

The possibility to modulate the surface morphology at the biphased composition by changing the film thickness can be exploited to control the surface-related properties. Here we propose to illustrate the potential of the competitive self-separation of amorphous and nanocrystalline phases by probing its ability to modulate the optical reflectance, as optical reflectance is highly sensitive to the nature and morphology of surfaces. Due to the increase of the nanocrystalline/amorphous ratio with thickness, a change in the surface roughness is also expected. This is highlighted in Figure 4.9, where the dependence of the surface roughness (black circles) with the thickness obtained from AFM measurements is shown. A smooth variation of the roughness from 5 to 100 nm is achieved by increasing the thickness up to 2 µm. Above 2 µm, the decrease of the roughness with thickness indicates a smoothening of the surface after it is completely covered by the nanocrystalline phase (zone 3 in Figure 4.5). Figure 4.10 shows the AFM images (left) for some of the samples obtained with their corresponding height distribution functions (right). The first peak of the height distribution functions is representative of the background, which in this case belongs to the height distribution function of the amorphous region. On the other hand, the second peak, coming from higher structures, represents the height distribution function of the dome-like nanocrystalline region.
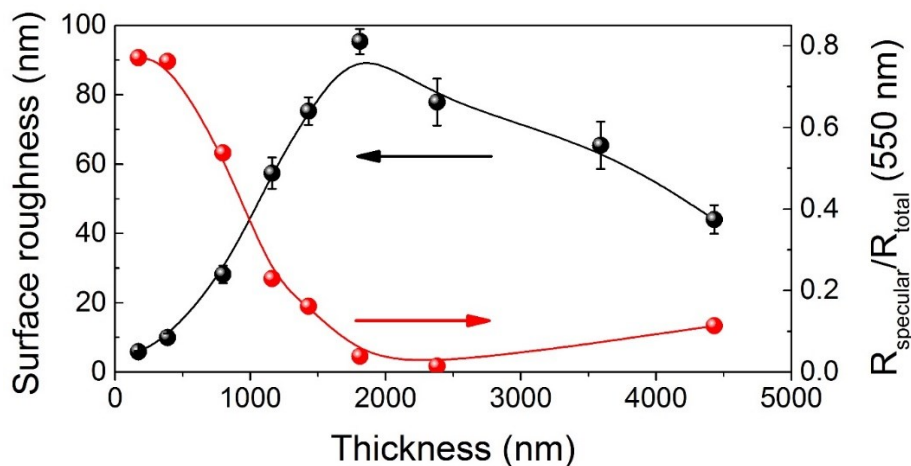
Figure 4.9. Evolution with thickness of the surface roughness (black circles) and the relative reflectance $\frac{R_S}{R_T}$ at a wavelength of 550 nm (red circles).

The possibility to control the roughness can be used to modulate the optical properties of the films. Figure 4.11 shows the relative reflectance (see eq. (2.5)) spectra for the different thicknesses obtained. The correlation between the surface roughness and relative reflectance is evidenced in Figure 4.9, where the dependence of the relative reflectance with thickness at a wavelength of 550 nm is shown. Therefore, by changing the film thickness and, with that, the surface roughness, we are able to control the reflectance at a certain wavelength.

Another important point to be addressed comes from the analysis of the zooms shown in Figure 4.11 for film thicknesses of 1160, 1430 and 1810 nm. A minimum is observed in the reflectance spectra. Further, the position of this minimum is changing with film thickness. Moreover, it is evident from the spectrum of the 1810 nm film that reflectance oscillates, as in an interference phenomenon. This can be understood by taking into account the height distribution functions of these samples, which are shown in Figure 4.10. As said before, the distributions show two predominant heights corresponding to the amorphous (background) and nanocrystalline (dome-like) regions. Therefore, if a light wave approaches the film, the presence of two height levels creates a path difference, which results in the creation of an interference pattern. The condition for minimum intensity in an interference pattern is [108]:

$$\Delta = (n + 1/2)\lambda_{min}, \tag{4.1}$$

where Δ is the path difference, n is an integer value and λ_{min} is the wavelength at which a minimum in intensity is detected. Hence, for the first minimum of interference $n = 0$ and, taking into account that the path difference for a wave coming perpendicular to the film surface is $\Delta = 2h$, where h is the distance between the two predominant heights, we can rewrite eq. (4.1) as:

$$h = \frac{\lambda_{min}}{4}. \tag{4.2}$$
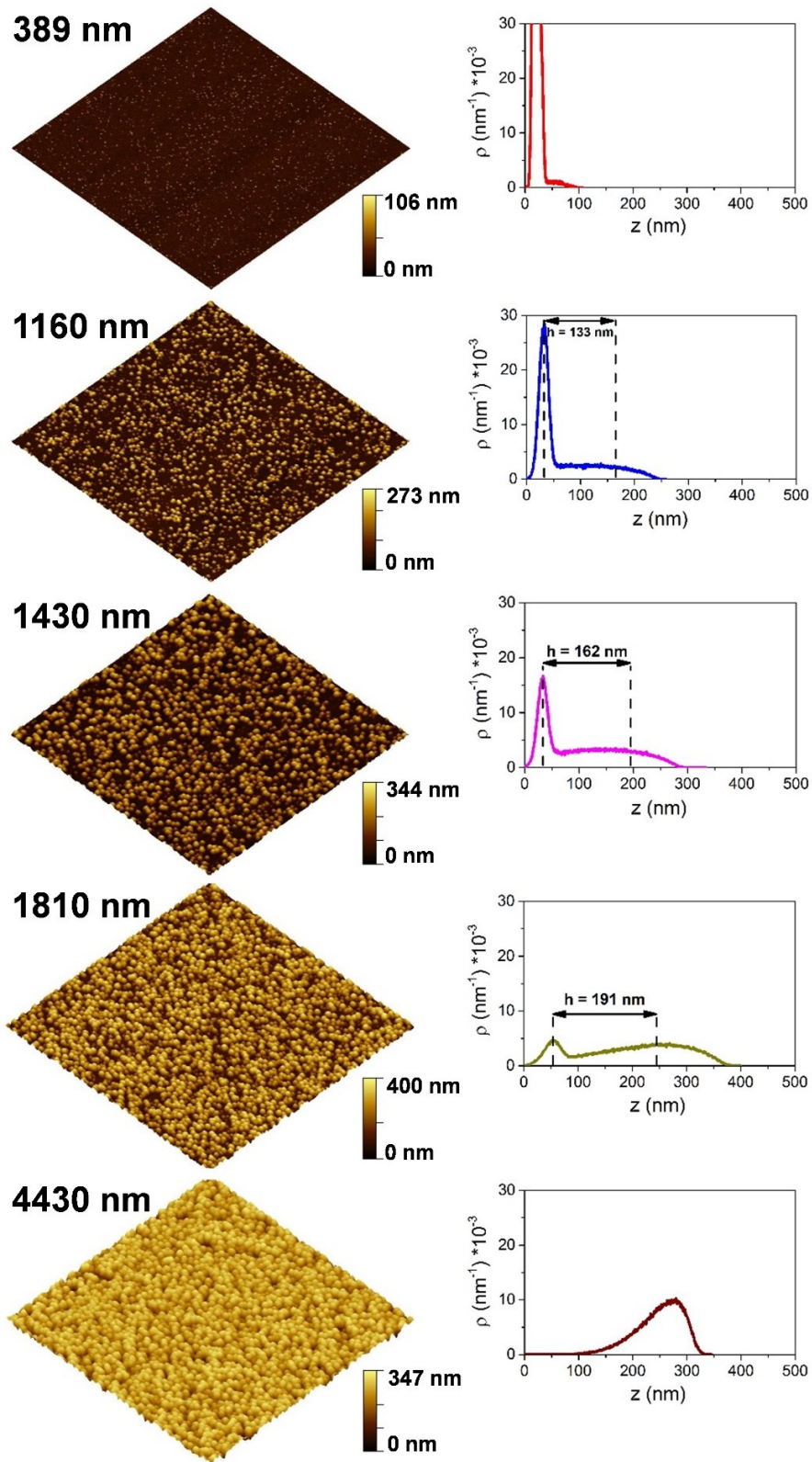
Figure 4.10. The panels show 45x45 μm² AFM images (left) for some of the samples obtained with their corresponding height distribution functions (right). The values of *h* for film thicknesses of 1160, 1430 and 1810 nm were calculated using eq. (4.2).

Eq. (4.2) gives us the height difference h that two height levels must have to cause a minimum in the reflectance spectrum at a wavelength $\lambda_{\min}$. Taking into account the values of $\lambda_{\min}$ extracted from the reflectance spectra (see Figure 4.11), the values of h were calculated and the results are shown in Figure 4.10. In this way, the higher height reached by the nanocrystalline phase with respect to the amorphous one creates a difference in height levels that is responsible for the minimum and maximum in the reflectance intensity. Thus, as the dome-like nanocrystalline phase grows with the increase of the film thickness, the difference in height levels also increases, causing a shift of the minimum of interference to longer wavelengths.

It is important to note that from eq. (4.2) it follows that in order to see the first minimum of the interference pattern in the range of wavelengths studied (between 350 and 900 nm), the height difference of the two height levels have to be between 87.5 and 225 nm. This is the case for the samples with a thickness between 1160 and 1810 nm while for the others thicknesses this condition is not satisfied. This is the reason why, for other thickness values, a minimum is not observed in the reflectance spectrum in the range of wavelengths studied. On the other hand, it is also important to have a similar proportion between the lowest and the highest levels. That means the surface coverage should be around 50%. This condition is better fulfilled when the film thickness is between 1160 and 1810 nm, where the surface coverage varies between 30 and 80%.

Even for thicknesses between 1160 and 1810 nm, where the samples satisfy the conditions explained above, there is not a strong difference between the minimum and the maximum of the reflectance, i.e. the interference pattern is not very well defined. This is because we do not have two well-defined height levels. On the contrary, there is a dispersion of the height values fundamentally within the height distribution of the nanocrystalline region, as can be follow from Figure 4.10. Thus, in order to obtain a better-defined interference pattern, a reduction in the dispersion of the height values is necessary. This last issue can be addressed by changing the deposition conditions, for example, the deposition pressure. In this way, the geometry of the nanocrystalline region could be changed and obtaining, for example, flatter structures would decrease the dispersion in the height distribution.
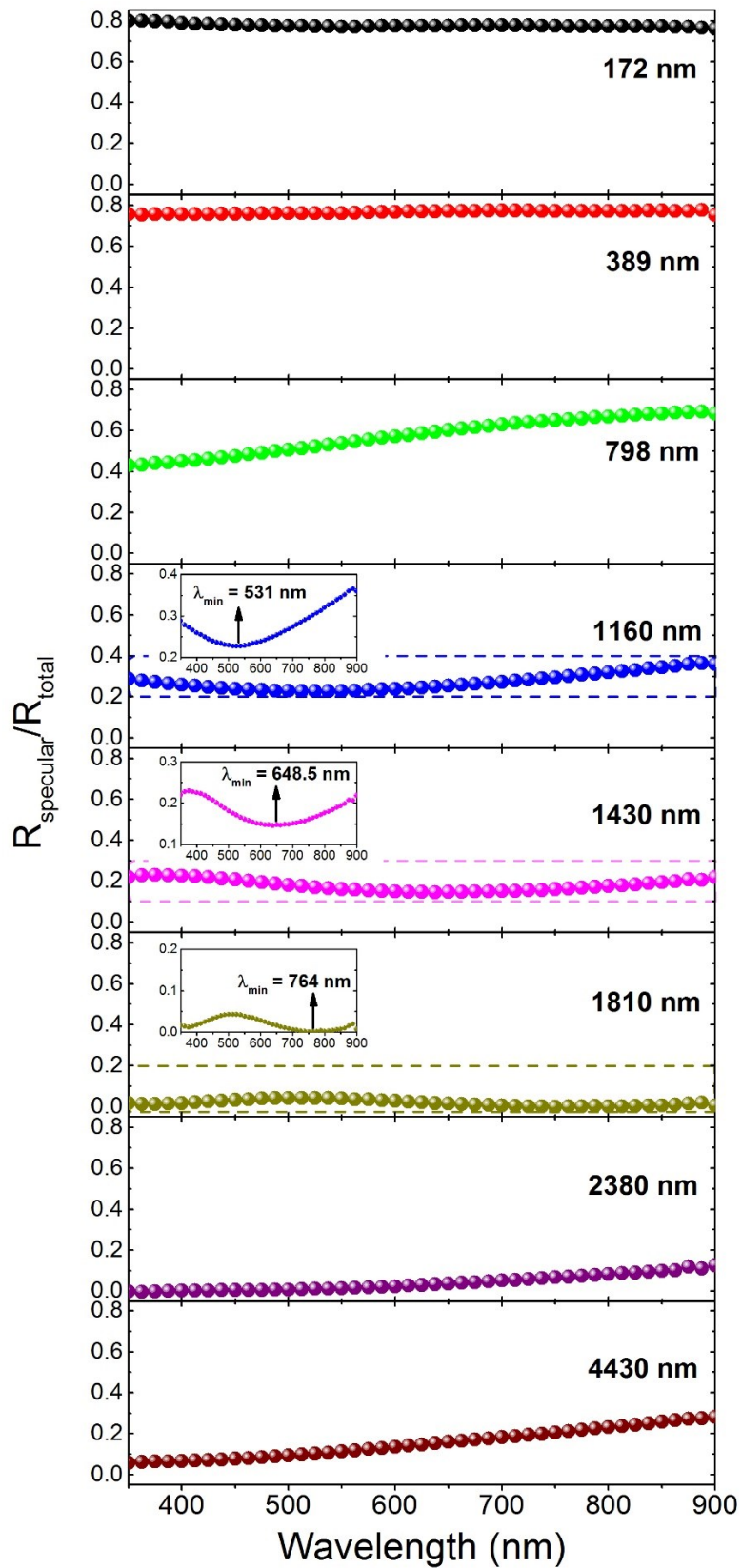
Figure 4.11. Relative reflectance spectra as the thickness increases. The zooms for film thicknesses of 1160, 1430 and 1810 nm show a minimum in the relative reflectance spectra.

Thereby, the reason behind the change of coloration in the "milky region" is the increase of the surface roughness due to the particular geometry of the nanocrystalline phase when growing in competition with the amorphous one. In fact, we have shown that the surface roughness can be tuned and a thickness-controlled reflectance can be achieved.

4.6 Towards a generalization of the nanocrystalline/amorphous competitive growth phenomenon

So far, we have shown that a competitive self-separation of phases occurs in Zr-Mo thin films obtained at 60 at% Mo, i.e. by working at a composition intermediate to those necessary to form single-phased amorphous and nanocrystalline films (in Chapter 5 we will show that this phenomenon occurs in a composition range that can be determined using a kinetics model). Nevertheless, this does not seem to be something particular for the Zr-Mo system. Here we show other examples in which nanocrystalline/amorphous competitive growth also occurs.

In sputter-deposited Zr-W thin films, a transition from the amorphous to the crystalline phase was also observed [3]. This transition is illustrated in the X-ray diffractograms shown in Figure 4.12(a1), in which the composition of Zr-W thin films was varied by changing the discharge current applied to the W target while keeping constant the current applied to the Zr target. Figure 4.12(a1) highlights that, as in the case of Zr-Mo, a mixture of both signals (the amorphous and the nanocrystalline) is obtained at the intermediate composition, in this case 72 at% of W. In addition, the SEM top-views shown in Figure 4.12(a2-a4) reveal the same situation as in the case of Zr-Mo. The surface morphology of sample obtained at the intermediate composition (72 at% of W) is a combination of the surface morphologies of the crystalline and the amorphous samples. Hence, competitive self-phase separation does not appear to be restricted to the Zr-Mo system and is likely largely present, but easily missed, in other binary alloys exhibiting a composition-driven transition from an amorphous to a crystalline phase.

Another example to support such a possible generalization of the process is the case of TiO_2 films [94]. In these films, a similar phase separation phenomenon was reported, that exhibits a transition from amorphous state with local anatase character to nanocrystalline rutile, the controlling parameter being the oxygen partial pressure during film growth that sets the
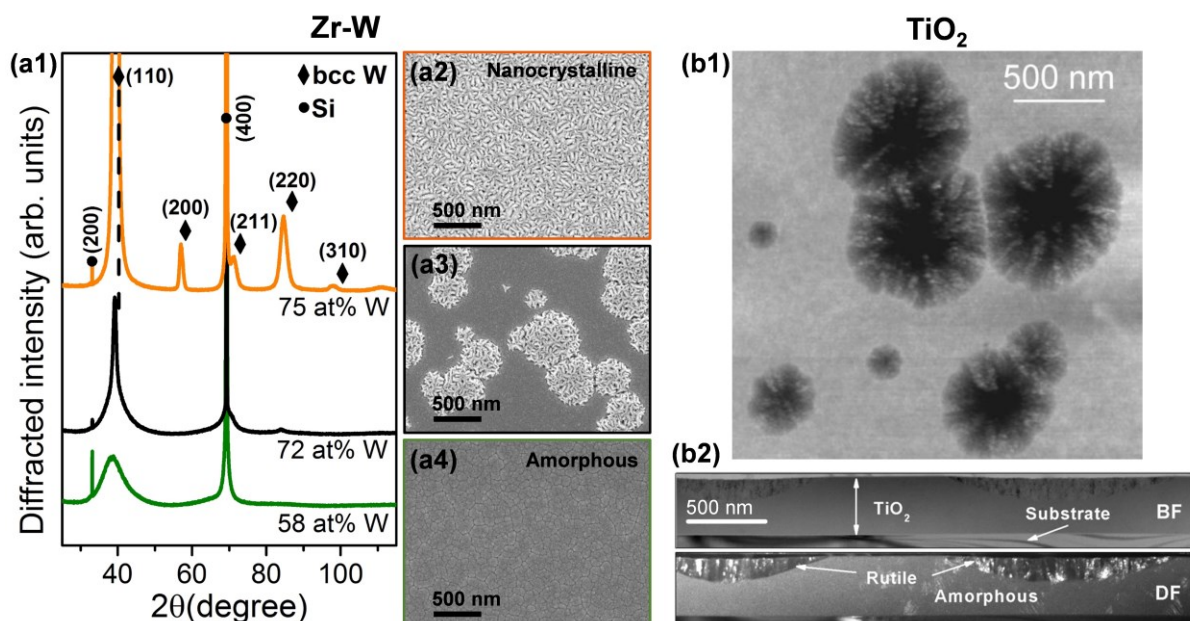
Figure 4.12. Sputter-deposited Zr-W (a) and TiO$_2$ (b) thin films. (a1) X-ray diffractograms for Zr-W films grown with different W contents. (a2-a4) Top-view SEM images corresponding to samples shown in (a1). (b1) AFM image of a TiO$_2$ film grown at 0.3 Pa. Lower heights appear in dark. (b2) TEM cross-sections showing bright (BF) and dark (DF) field images of TiO$_2$ films (from ref. [94]).

oxygen content in the Ti-O films. Similarly to the results reported on Zr-Mo and Zr-W, in biphased Ti-O films, growth initiates with the amorphous phase before the nanocrystalline phase nucleates. The difference between the results obtained with Zr-Mo films and those for the TiO$_2$ films is the geometrical shape of the nanocrystalline phases. In the case of Zr-Mo, the nanocrystalline phase grows with a dome-like shape at the surface (see Figure 4.5(c)), while TiO$_2$ films reported in [94] exhibit hollow structures (holes) on the surface (see Figure 4.12(b)). Such difference can be understood considering the growth rates of the nanocrystalline phase in the in-plane (parallel to the film surface) and vertical (perpendicular to the film surface) directions are different in the two situations. An increase of the growth rate in the in-plane direction with reference to the vertical one, supported by an improved mobility of adatoms, can lead to diffusion of adatoms from the center of nanocrystalline precipitates towards their periphery. TiO$_2$ films were deposited at a lower pressure (0.3 Pa) than Zr-Mo (2 Pa) and Zr-W (3 Pa) films. A lower working pressure increases the mean free path of sputtered atoms in the gas phase and decreases the number of collisions a sputtered atom experiences before it lands on the film surface. This result in the increase of the kinetic energy of the adatoms arriving at

the film surface, favoring the mobility in the in-plane direction and, consequently, the growth rate of the crystalline region in this direction can increase.

Precisely, the two examples presented here are the inspiration for the next two chapters of this thesis. In Chapter 5, a deeper study of the Zr-W system will be conducted, including the development of a model capable of describing the kinetics of the nanocrystalline/amorphous competitive growth. Then, in Chapter 6, the hypothesis presented here on the influence of the deposition pressure on the geometrical shape of the crystalline phase will be tested. To this end, Zr-Mo films deposited at lower pressure will be presented.

4.7   Chapter conclusions

In this chapter, the nature of the "milky region" was investigated. We have shown that it is a biphased region that appears when working at a composition between those necessary to obtain monophased amorphous and nanocrystalline sputter-deposited Zr-Mo thin films. In this region, a self-separation of these phases in well defined spatial regions can be achieved. The regions delimiting the nanocrystalline phase present a conical shape (with a feather-like morphology) embedded in the amorphous phase and that terminates with a dome whose base is aligned with the surface of the amorphous phase. Due to the particular geometry in which the nanocrystalline phase grows, the morphology at the biphased composition changes with the film thickness. The influence of the morphology evolution on the stress was discussed. Moreover, our results indicate that the nucleation of the nanocrystalline phase starts at the boundaries between adjacent columns (grains). Based on this, we proposed that the difference in the diffusion rates of Mo and Zr towards the grain boundaries is a possible mechanism for the self-separation of phases. Because of the competitive self-phase separation, it was possible to control the surface roughness of the films and, thereby, to tune the reflectance at a determined wavelength, using the film thickness as a control parameter. Thus, it was demonstrated that the origin of the change in optical appearance in the "milky region" is the increase of the surface roughness. We also shown that the presence of a minimum in the reflectance spectra is due to the presence of two height levels in the height distribution function.

Finally, we show that the self-separation of phases as presented here is a more general phenomenon. It can be obtained in other binary alloys showing a composition-driven transition from an amorphous to a crystalline phase. This is the case of the Zr-W system, which will be studied in the next chapter in more details. Also in the Ti-O system, a similar phenomenon occurs but with a different morphology of the crystalline phase, suggesting that the geometry in which the crystalline phase grows can be changed by varying the working pressure. This will be the object of study of Chapter 6. Thus, by changing the parameter that triggers this transition, i.e. the Mo(W) content in the case of Zr-Mo(W) alloys and the oxygen partial pressure in the Ti-O system, the self-separation of phases can be obtained.

Chapter 5

Kinetics of nanocrystalline/amorphous competitive growth in thin films
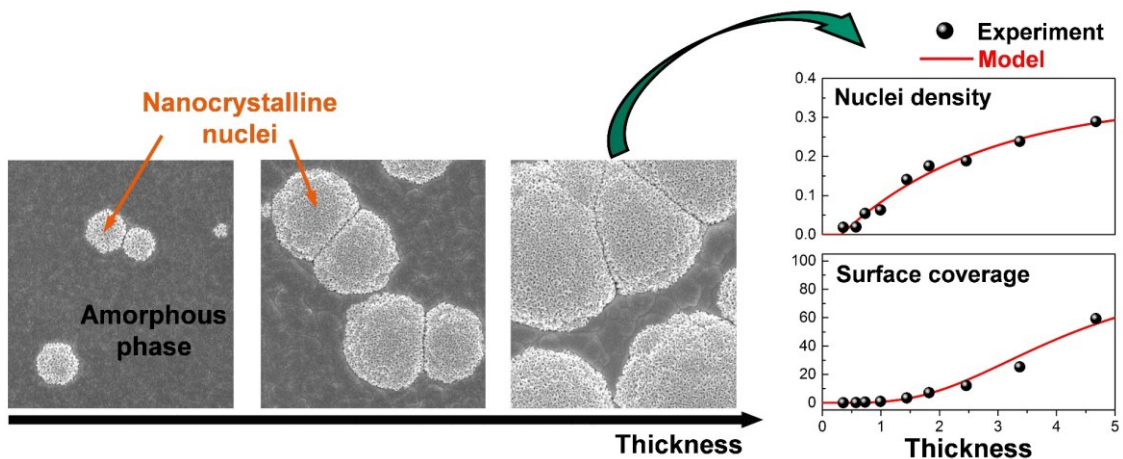
ABSTRACT: Kinetic models are fundamental for the design and optimization of nanostructured materials from both a fundamental and a functional point of view. In the previous chapter, we have shown the possibility of obtaining sputter-deposited biphased nanostructures consisting of a nanocrystalline phase with a feather-like morphology embedded in an amorphous phase. The peculiar morphology of these nanostructures appears as a consequence of the competitive growth between the two phases. In this chapter, we present a model derived from the modular kinetic model for 2D transformations in which Avrami nucleation is assumed and capable of describing the kinetics of competitive growth in thin films. This model is applied to fit experimental density of nuclei and surface coverage of overgrowing phase for a nanocrystalline phase progressively overgrowing an amorphous matrix in Zr-W sputter-deposited thin film alloys. Thereby, fundamental parameters of the competitive growth process are extracted, i.e. composition-driven density of nucleation sites, critical thickness for nucleation, impingement parameters and nucleation rate. Moreover, the model developed allowed constructing the thickness-composition phase diagram evidencing the nanocrystalline-amorphous competitive growth, yet occurring in a wide composition range, is easily hidden experimentally due to composition-driven kinetics and critical nucleation thickness.

Contents

5.1 Introduction

Competitive growth is widely observed in thin films grown by physical vapor deposition (PVD) methods. It is one of the fundamental mechanisms governing the growth process when working in zone T of the extended structure zone model (following the classification presented in [50,109,110]), when grains with the geometrically fastest-growing direction perpendicular to the substrate overgrow grains of all other orientations, similar to the so-called van der Drift [111] evolutionary selection. Yet, formalism for its kinetics is not available to date. On the other hand, the kinetics of solid-state phase transformations are often described using the classical Kolmogorov-Johnson-Mehl-Avrami (KJMA) [112–116] approach. The KJMA approach, although powerful, is not applicable in many cases in which the constraints imposed in its deduction are violated. A more general approach that avoid the restrictions of the classical KJMA model is the modular kinetic model (MKM) [117–120], in which KJMA model is recovered for the specific case of isothermal annealing and pre-existing nuclei or continuous nucleation.

In Chapter 4, we showed that by working at a composition intermediate to those needed to obtain single-phased amorphous or nanocrystalline Zr-Mo films, the so-called "milky region" is obtained. We reported that, in this region, as a consequence of the competitive growth of the amorphous and the nanocrystalline phases, original microstructures can be obtained consisting of a nanocrystalline phase of feather-like morphology embedded in an amorphous matrix. Similar to the case of Zr-Mo, in sputter-deposited Zr-W thin film alloys synthesized without thermal assistance a transition from a X-ray amorphous to a nanocrystalline structure is obtained upon increasing the W content [3,8]. This transition was illustrated at the end of Chapter 4 (see Figure 4.12(a)) and the analysis of the surface morphology of the films indicated that the nanocrystalline and the amorphous phases are coexisting at the intermediate composition. In this chapter, we demonstrate that nanocrystalline/amorphous competitive growth also occurs in Zr-W system. We develop a model capable of describing the kinetics of this competitive growth. Interestingly, this can be addressed using the MKM approach, even though competitive growth is not strictly a phase transformation. As a proof of concept, we
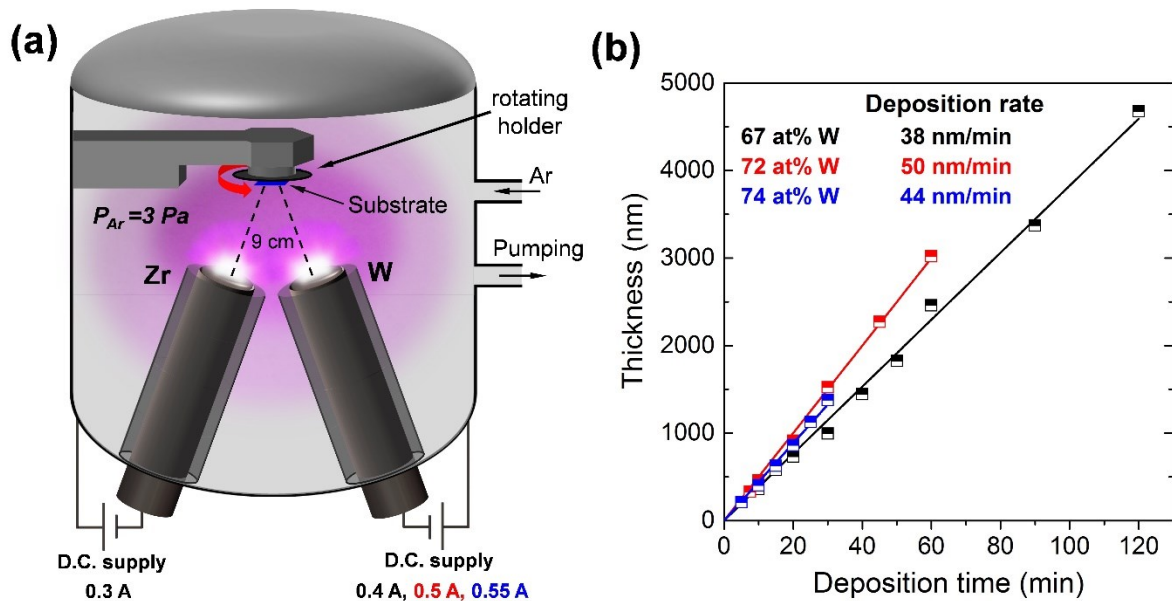
Figure 5.1. (a) Schematic of the sputtering chamber showing the parameters used during film depositions. (b) Evolution of the thickness with the deposition time for the compositions studied.

chose the Zr-W system. Yet, the model developed can be generalized to other systems where the nanocrystalline/amorphous competitive growth occurs.

5.2 Evolution of the surface morphology with composition and thickness

So far, we have referred to the "milky region" as occurring at *one* composition: the intermediate to those needed to obtain single-phased amorphous or nanocrystalline films. However, the "milky region" must exist in a range of compositions. In order to clarify the extend of the composition range in which the competitive growth phenomenon occurs, here we propose to study different compositions within the "milky region". Thus, Zr-W thin films were deposited following the same procedure that in previous chapter but varying the W content. To ensure the homogeneity of the films, all the depositions were made with the substrate holder in rotating mode. The W content in the films was controlled by applying a discharge current of 0.3 A to the Zr target and 0.4, 0.5 and 0.55 A to the W target (see Figure 5.1(a)). Under these conditions, films with W content of 67, 72 and 74 at% were obtained. The evolution of the film thickness with the deposition time for the compositions studied is shown in Figure 5.1(b).
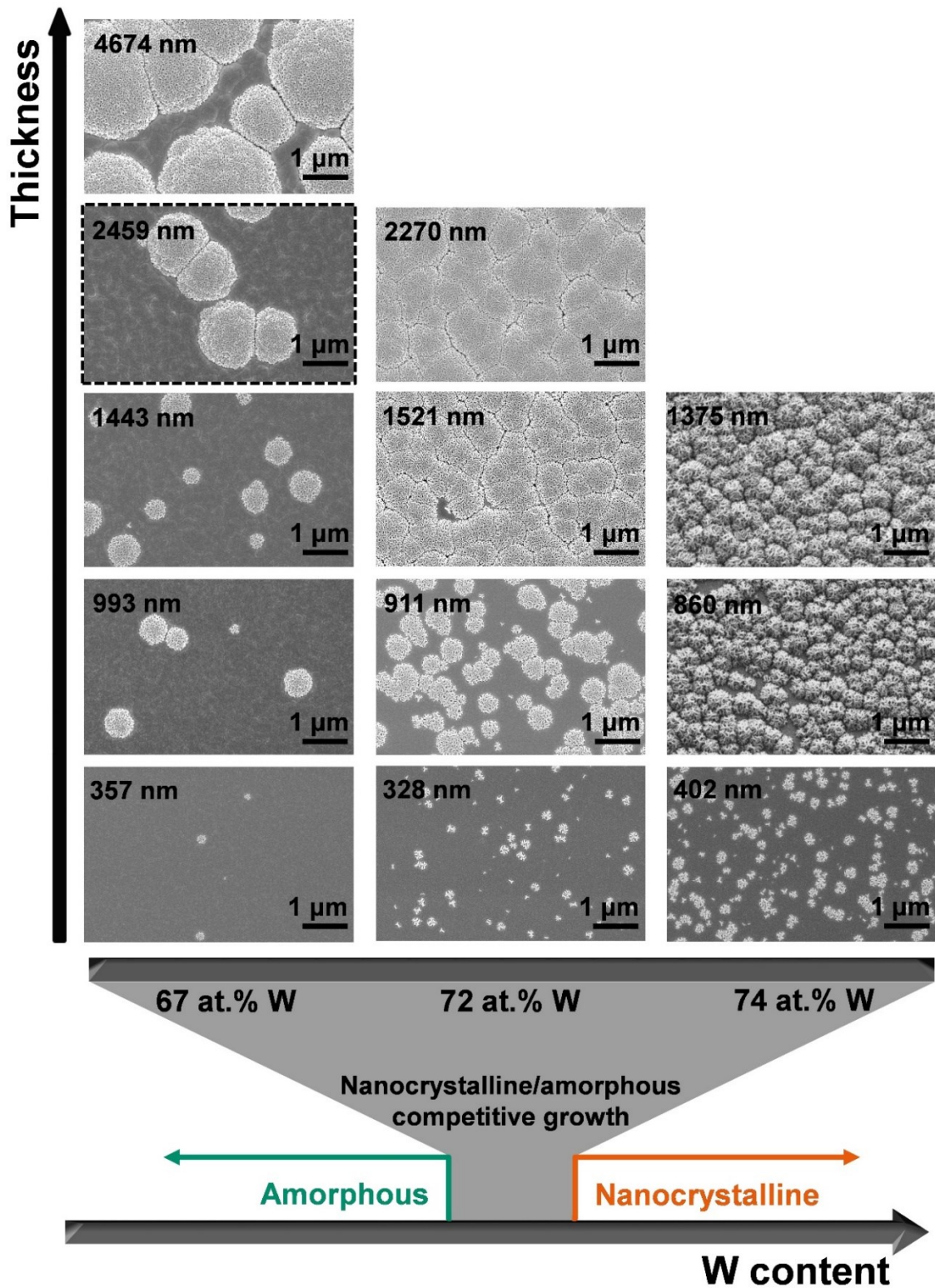
Figure 5.2. Evolution of the surface morphology with composition and thickness. At the bottom, a schematic of the structure evolution with W content in sputter-deposited Zr-W thin films is presented. On top, the evolution of the surface morphology with thickness is shown for three compositions supporting the nanocrystalline/amorphous competitive growth.

The schematic shown at the bottom of Figure 5.2 illustrates that the nanocrystalline/amorphous competitive growth occurs for the three obtained compositions. It is observed that, in the explored composition range, competitive growth occurs after a critical thickness is reached. Two regions with different morphologies can be observed in the SEM top-view images. A phase with dark contrast dominates at lower thicknesses and acts as a matrix embedding brighter zones of rounded shape and that dominate at higher thicknesses. Figure 5.2 evidences that the proportion between the two phases can be controlled by changing the thickness or composition. Figure 5.3(a) shows a typical cross-section TEM view of the biphased samples and evidences that the cross section of the brighter zones is conical inside the bulk of the film and terminates with a dome whose base is aligned with the surface of the matrix as for the case of Zr-Mo in the previous chapter. The zoom shown in Figure 5.3(b) evidences the spatial separation of both regions and the high resolution TEM images and their FFT patterns
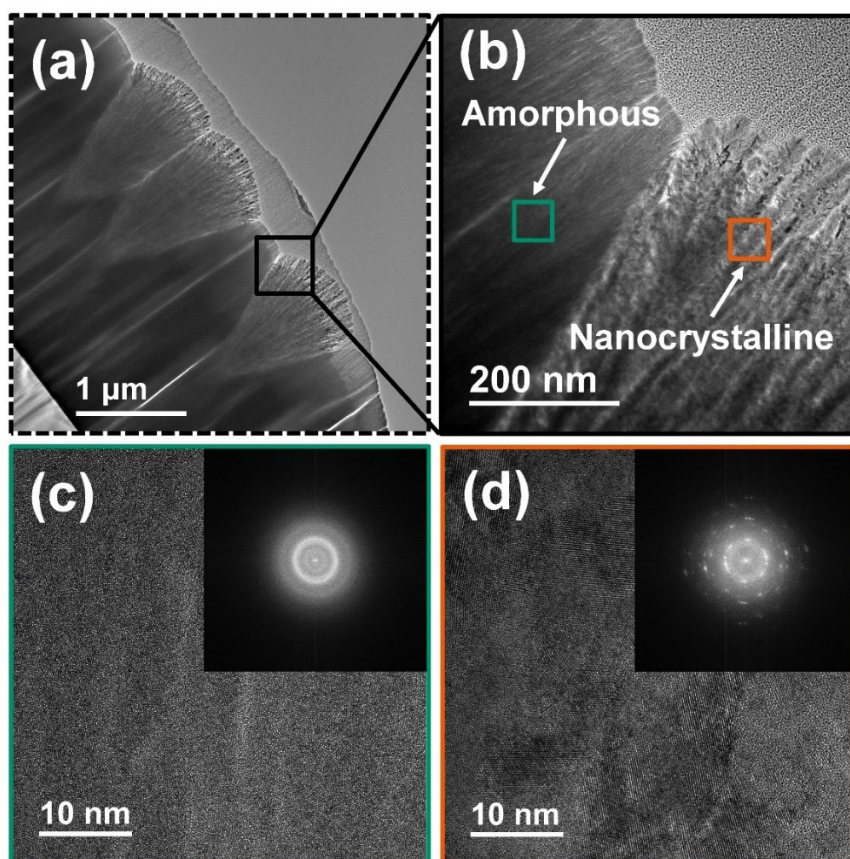
Figure 5.3. (a) TEM cross-sectional image of sample highlighted in Figure 5.2. (b) Zoom of image shown in (a). (c) HRTEM image and FFT from the region highlighted with a green square in (b). (d) HRTEM image and FFT from the region highlighted with an orange square in (b).

performed in the zones marked by the green (Figure 5.3(c)) and orange (Figure 5.3(d)) squares confirm the amorphous and nanocrystalline character of the darker and brighter regions, respectively.

5.3   Stress evolution with thickness

In Figure 5.4(a), the evolution of residual stress with thickness for the three compositions studied is shown. Similarly to the case of Zr-Mo, three regimes in the stress behavior can be identified: increase-slight decrease-stabilization. Interestingly, when the W content is increased, the stress is scaling with thickness, i.e., at higher W contents the maximum in the stress curve (more relaxed state) is reached at a lower thickness. This is because with the increase of W content, more nanocrystalline regions appears for the same thickness, as can be seen in Figure 5.2. Thus, we can infer that the factor that determines the level of stress is the proportion between the nanocrystalline and the amorphous phases. This is clearly evidenced in Figure 5.4(b), where the dependence of the stress with the surface coverage by the nanocrystalline regions is shown. In the figure is also shown the stress-surface coverage dependency in the Zr-Mo system for the composition studied in Chapter 4. The figure indicates that the stress evolution as a function of the surface coverage follows the same trend for the Zr-W (even for different compositions) and the Zr-Mo systems. We can conclude that the surface coverage by the nanocrystalline regions determines the behavior of the stress in the nanocrystalline/amorphous competitive growth phenomenon. Therefore, stress first increases in zone 1 (surface coverage below 15%), decreases slightly in zone 2 (surface coverage between 15% and 80%) and finally stabilizes in zone 3 (surface coverage above 80%).
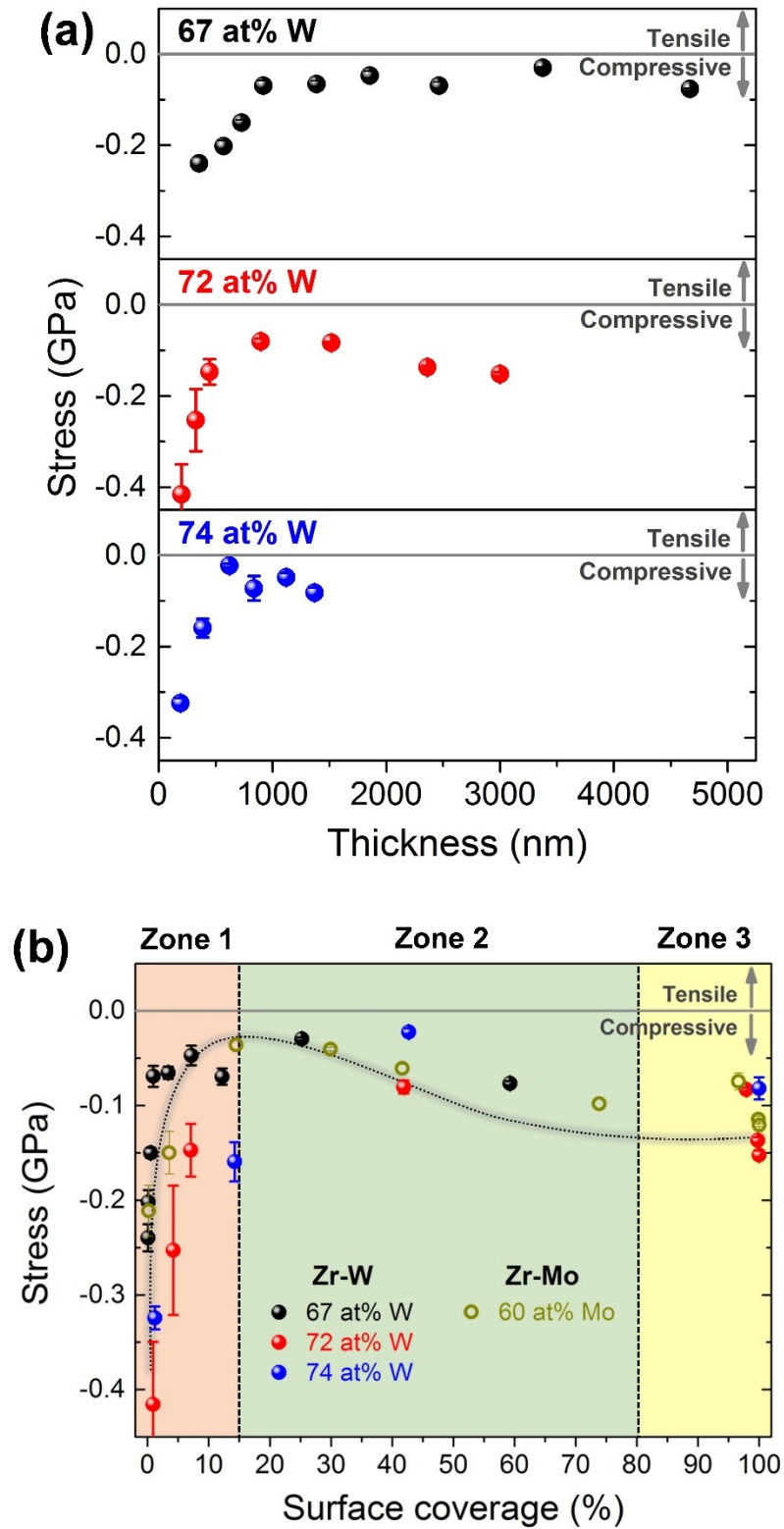
Figure 5.4. (a) Evolution of residual stress with thickness in the Zr-W system for the three compositions studied. (b) Dependency of the stress with the surface coverage for Zr-W and Zr-Mo films. In both cases, three different zones can be identified.

5.4 Kinetics of the phase separation

In the following, a kinetics model using the MKM [117–120] approach and capable of describing the nanocrystalline/amorphous competitive growth is developed. It is important to point out that this phenomenon is not a phase transformation in the "classical" sense. In a phase transformation, a new phase appear from a previous one upon change of one or many controlling factors, as temperature, concentration, etc. In the present case, the amorphous phase is growing in competition with the nanocrystalline one, but it is not transforming into the nanocrystalline phase. That is, the regions that condensate in an amorphous phase at a given film thickness keep their amorphous structure when the film continues growing. However, the surface morphology evolution with thickness presented in Figure 5.2 can be interpreted as a picture from the same region of the sample when the time is passing. In this way, the amorphous phase seems to be transforming into the nanocrystalline one. Thus, the surface morphology evolution with film thickness, as presented in Figure 5.2, is equivalent to an "apparent" 2D transformation with time. This means that the formalism of 2D transformation can be used to extract the kinetics of competitive growth between the amorphous and the nanocrystalline phases.

We start assuming an Avrami nucleation mechanism [114–116], which means in our case that the nucleation of the nanocrystalline phase occurs at certain sites in the sample, which are gradually exhausted upon film growth. Let N be the number of particles of the nanocrystalline phase (growth nuclei) per unit area and N_{germ} the number of germ nuclei per unit area from which the growth nuclei are formed, such that the total number of growth and germ nuclei per unit area N_0 is constant. Thus, the change in the density of growth nuclei can be written as [117–120]

$$\frac{dN}{dt} = -\frac{dN_{germ}}{dt} = \lambda\, N_{germ},\qquad(5.1)$$

where λ is the rate at which an individual germ nucleus becomes in a growth nucleus. After integration, considering the boundary condition that the density of germ nuclei equals N_0 at $t = 0$, the density of growth nuclei is given by

$$N_{(t)} = N_0 \left(1 - e^{-\int_0^t \lambda \, dt}\right). \tag{5.2}$$

The nature of the apparent 2-dimensional phase transformation presented here makes possible the use of film thickness h as a replacement of time t as the variable that controls the grade of transformation. Considering that the deposition rate of the film V_0 is constant, the sample thickness is $h = V_0 t$ and, in this way, all the expressions obtained can be expressed as a function of film thickness. Thus, the density of growth nuclei can be re-written as:

$$N_{(h)} = N_0 \left(1 - e^{-\frac{1}{V_0}\int_0^h \lambda \, dh}\right) \tag{5.3}$$

and its derivative (the nucleation rate) as:

$$\frac{dN}{dh} = \frac{\lambda}{V_0} N_0 e^{-\frac{1}{V_0}\int_0^h \lambda \, dh}. \tag{5.4}$$

An important point in our approach is how to express the rate λ. It is usually supposed [114,117–120] that λ obeys Arrhenius-type temperature dependence: $\lambda = \lambda_0 e^{-\frac{Q_n}{RT}}$, where λ_0 is a temperature-independent rate and Q_N is the activation energy (energy barrier) for nucleation. In our case, the experimental evidence is pointing to the conclusion that there is a thickness from which nucleation starts, i.e., there is an incubation thickness. This indicates that the activation energy for the nucleation of the crystalline phase $Q_N \gg RT$ at the beginning of the film growth, consequently, the films starts to grow amorphous. With the increase of the film thickness, the crystalline phase starts to nucleate which implies that the energy barrier Q_N decreases to a value of the order of RT. The reasons behind this decrease in the energy barrier with thickness could be chemical (a local change in composition due to the preferred segregation of one of the species, for example, to the grain boundaries, as was proposed in the previous chapter), mechanical (local changes of the strain energy due to the heterogeneous distributions of the film stress [121] which can decrease the energy barrier), among others. Considering this, we propose to write λ as follows:

$$\lambda = \lambda_0 e^{-\frac{Q_n}{RT}} \Theta[h - h_c], \tag{5.5}$$
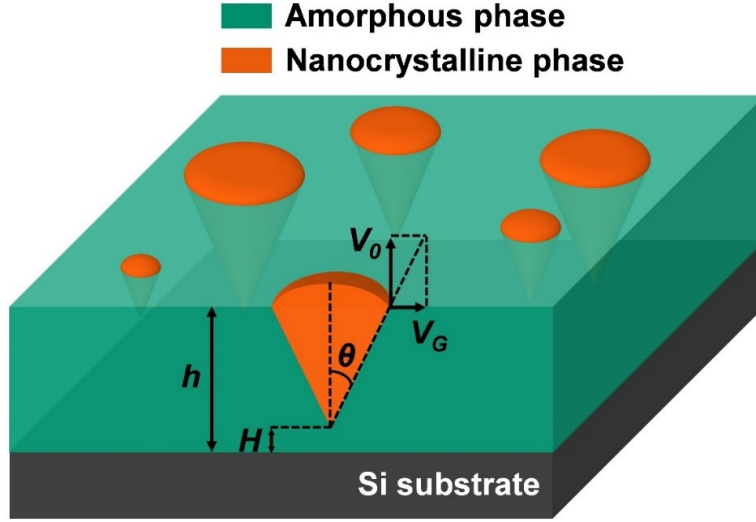
Figure 5.5. Schematic of the obtained microstructure of a film grown in the biphased region.

where Θ is the unitary-step Heaviside function and h_c is the critical thickness from which nucleation starts. Eq. (5.5) is a simplification of the real scenario presented above where a gradual decrease of Q_N occurs instead of the sudden decrease of the function Θ. Nevertheless, the use of Θ simplifies all the derived equations, yet retaining the physics of the phenomenon. Thereby, eqs. (5.3) and (5.4) follow the dependencies:

$$N_{(h)} = N_0 \left(1 - e^{-\frac{\lambda_f}{V_0}(h-h_c)} \right) \Theta[h - h_c] \tag{5.6}$$

and

$$\frac{dN}{dh} = \frac{\lambda_f}{V_0} N_0 e^{-\frac{\lambda_f}{V_0}(h-h_c)} \Theta[h - h_c], \tag{5.7}$$

where $\lambda_f = \lambda_0 e^{-\frac{Q_n}{RT}}$. In this way, through eq. (5.6), the evolution of the density of growth nuclei with thickness can be calculated.

In the framework of the MKM approach, the evolution of the so-called "extended transformed fraction" with time t for 2-dimensional transformation is given by [117–120]

$$\chi_e(t) = \frac{S_e}{S} = \int_0^t \left(\frac{dN}{dt} \right)_{(\tau)} Y_{(\tau,t)} d\tau, \tag{5.8}$$

where S_e represents, in our case, the projected area, perpendicular to the growth direction of nanocrystalline regions if they could each nucleate and grow in the absence of other interfering growing nuclei and S is the total surface area. Eq. (5.8) can be re-written as a function of h as follows:

$$\chi_e(h) = \int_0^h \left(\frac{dN}{dh}\right)_{(H)} Y_{(H,h)} dH, \tag{5.9}$$

where $\frac{dN}{dh}$ is given by eq. (5.7) and $Y_{(H,h)}$ represents the projected area at a film thickness h of a nanocrystalline nucleus nucleated at a film thickness H (see Figure 5.5). Thus, $Y_{(H,h)}$ can be written in our case as:

$$Y_{(H,h)} = \pi \left(\frac{V_G}{V_0}\right)^2 (h - H)^2, \tag{5.10}$$

where V_G is the growth velocity of the nanocrystalline phase in the in-plane direction (see Figure 5.5). Using eqs. (5.7) and (5.10) the extended transformed fraction is obtained

$$\chi_e(h) = \pi N_0 \left(\frac{V_G}{V_0}\right)^2 \frac{\lambda_f}{V_0} e^{\frac{\lambda_f}{V_0}h_c} I \Theta[h - h_c], \tag{5.11}$$

where $I = \int_{h_c}^h (h - H)^2 e^{-\frac{\lambda_f}{V_0}H} dH$. After integration of I, the final expression for the extended transformed fraction is given by

$$\chi_e(h) = \pi \left(\frac{V_G}{V_0}\right)^2 \frac{N_0}{\left(\frac{\lambda_f}{V_0}\right)^2} \left(-2e^{-\frac{\lambda_f}{V_0}(h-h_c)} + \left(\frac{\lambda_f}{V_0}(h - h_c) - 1\right)^2 + 1\right) \Theta[h - h_c]. \tag{5.12}$$

The relation between the extended transformed fraction and the real transformed fraction (in our case, surface coverage by the nanocrystalline phase) f depends on the spatial distribution of the nanocrystalline growth nuclei in the parent phase (amorphous phase). Thus, if a random nucleation (RN) of the new phase is supposed, as in the case of the classical Kolmogorov-Johnson-Mehl-Avrami (KJMA) [114–116] approach, they can be related according to

$$f = 1 - e^{-\chi_e}. \tag{5.13}$$

Nevertheless, if nuclei are not randomly distributed, for example, when grain boundaries nucleation (GBN) occurs, eq. (5.13) is not fulfilled. A phenomenological approach accounting for impingement in this case has been proposed in [120] and f can be written as a function of χ_e as follows:

$$f = 1 - (1 + (\xi - 1)\chi_e)^{-1/\xi-1}, \tag{5.14}$$

where ξ is the so-called "impingement parameter".

So far, expressions for the evolution with thickness of the density of nuclei (eq. (5.6)) and the transformed fraction in the case of RN (eqs. (5.12) and (5.13)) and GBN (eqs. (5.12) and
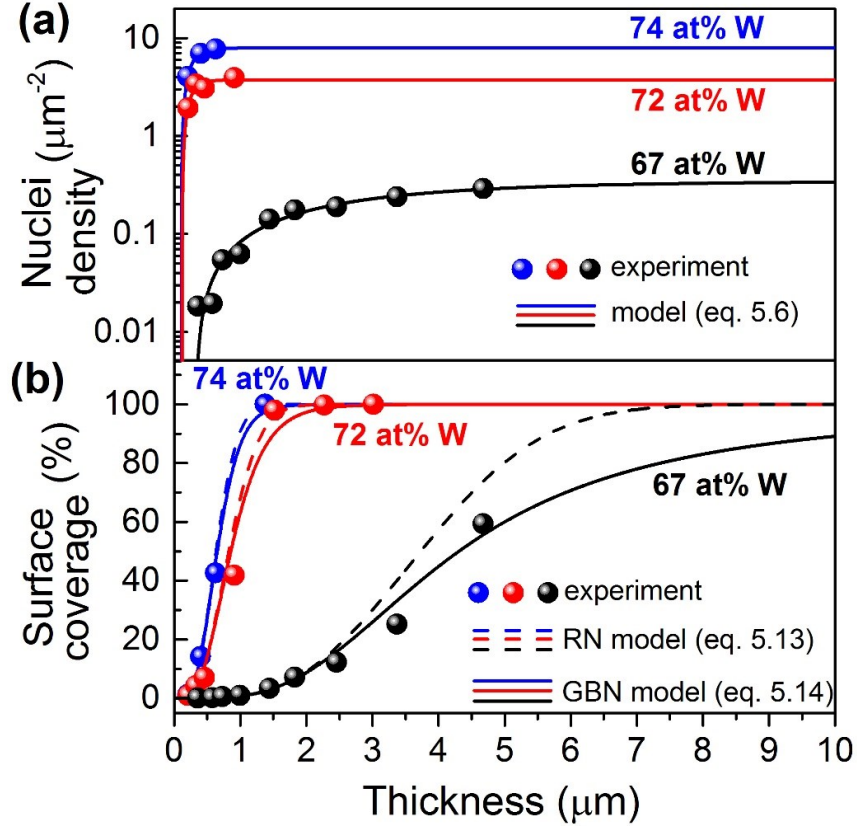
Figure 5.6. Evolution of the density of nanocrystalline nuclei (a) and surface coverage by the nanocrystalline phase (b) with the increase of the film thickness for the three compositions studied. The dots represents the experimental data. In (a) the lines follow eq. (5.6). In (b) the dotted lines follow eq. (5.13) and the continues lines follow eq. (5.14). The parameters used are shown in Table 5.1.

(5.14)) has been obtained. In the case of eq. (5.6) there are three free parameters to fit the experimental data: N_0, $\frac{\lambda_f}{v_0}$ and h_c. On the other hand, eq. (5.12) has as free parameters the three of eq. (5.6) and the ratio $\frac{V_G}{v_0}$ between the in-plane growth velocity of the nanocrystalline regions and the deposition rate. From the schematic shown in Figure 5.5 follows that $\frac{V_G}{v_0} = \tan(\theta)$, where θ is the angle between the generatrix and the axis of the cone representing the embedded part of the nanocrystalline zones. The analysis of several cross-section images reveals that θ can be considered constant for all the samples studied and can be approximated to $\theta = 22°$. Thus $\frac{V_G}{v_0} = 0.404$ can be fixed and eq. (5.6) and eq. (5.12) can be used to fit the data with the same free parameters.

Table 5.1. Fitting parameters. Evolution with W content of the density of nucleation sites N_0, λ_f/V_0, the critical thickness h_c and the impingement parameter ξ.

W content (at%)	N_0 (µm^{-2})	λ_f/V_0 (10^{-3} nm^{-1})	h_c (nm)	ξ
67	0.34	0.41	322	2.15
72	3.74	8.33	120	1.26
74	7.92	7.19	108	1.18

Figure 5.6(a) shows the evolution with thickness of the density of nuclei for the three compositions studied extracted from the analysis of the SEM images (see Appendix section for details). The fittings of eq. (5.6) to the experimental data are shown with full lines and the values of the parameters obtained are reported in Table 5.1. We can conclude that increasing the W content implies an increase of the density of nucleation sites N_0, a decrease of the critical thickness h_c and the rate λ_f at which an individual germ nucleus becomes in a growth nucleus increases then stabilizes.

The parameters obtained by fitting the density of nuclei can be evaluated in eq. (5.12). In this way, the evolution of the extended transformed fraction χ_e with the sample thickness can be calculated. Then, the surface coverage can be determined from eq. (5.13) or eq. (5.14), depending on the type of nucleation assumed. The measured surface coverage is shown with points in Figure 5.6(b) for the three compositions studied determined by analyzing the SEM images (see Appendix section for details). Dotted lines represent the surface coverage calculated in the case of RN (eq. (5.13)). We can see, especially for the case of lower W content (67 at%), that the measured surface coverage is lower than calculated. This is because the nanocrystalline zones start to interact earlier than in the case of random nucleation, and it is an indication that the nucleation occurs at the grain boundaries, as was already proposed in Chapter 4. For GBN it is more suitable to use eq. (5.14). In this equation, the parameter ξ takes into account the grade of impingement. The fit of eq. (5.14) to the experimental data using ξ as free parameter is shown with lines in Figure 5.6(b). The fact that ξ is closer to 1 when the W content increases (Table 5.1) means that when the density of nuclei increases, the surface coverage in the case of GBN approaches that of RN.
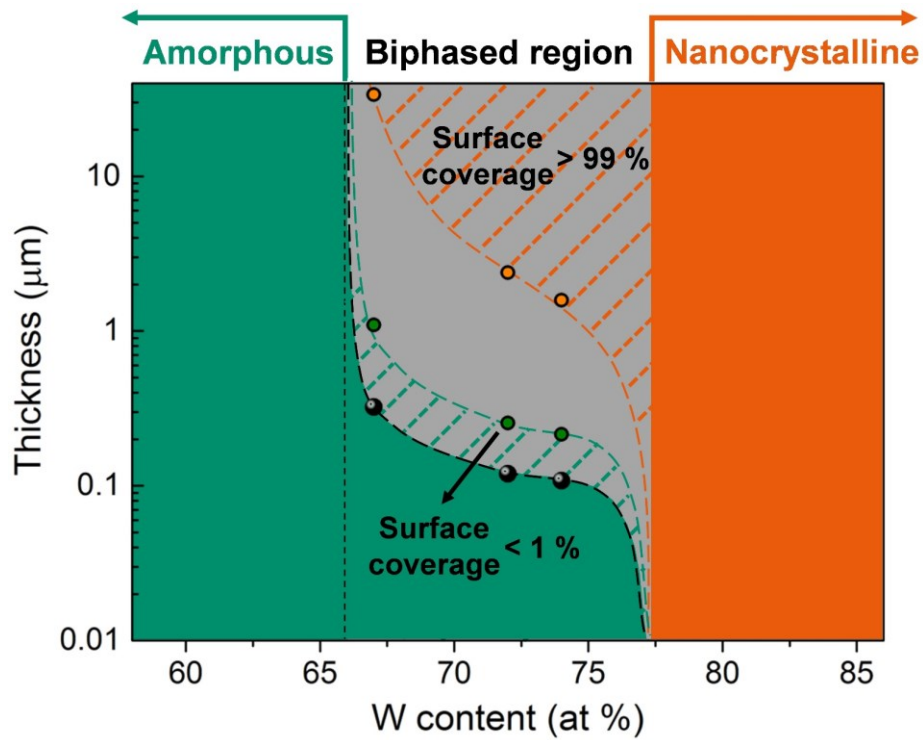
Figure 5.7. Thickness-composition Zr-W phase diagram. Depending on composition, the structure of the films can be single-phased amorphous (green zone), single-phased nanocrystalline (orange zone) or biphased at intermediate compositions (gray zone). In this domain are shown the values of the critical thickness (black points) and the thickness at which the surface coverage is lower than **1**% (green points) and higher than **99**% (orange points).

As illustrated in Figure 5.2, the proportion between the nanocrystalline and the amorphous phase can be controlled either by varying the composition or the film thickness. The biphased region is obtained when the W content is varied in the range $W_0 < W < W_c$. If $W \leq W_0$ the obtained films are single-phased amorphous and if $W \geq W_c$ the films are single-phased nanocrystalline. W_0 and W_c can be determined by using the evolution of the density of nucleation sites N_0 with composition (Table 5.1) and considering that N_0 satisfies the boundaries conditions: $N_0 = 0$ when $W = W_0$ and $N_0 \to \infty$ when $W = W_c$. Note that, at the same time $h_c = 0$ when $W = W_c$ as follows from the definition of W_c. Thereby, the following empirical dependency between N_0 and W can be assumed:

$$N_0 = A \left(\frac{W - W_0}{W_c - W} \right), \tag{5.15}$$

where A, W_0 and W_c can be determined with the values of N_0 and W content presented in Table 5.1. Thus, we obtain: $A = 3.30 \ \mu m^{-2}$, $W_0 = 65.9$ at% and $W_c = 77.4$ at%.

In Figure 5.7 is shown a thickness-composition phase diagram of sputter-deposited Zr-W alloy films when the W content is changed. We can see that the nanocrystalline/amorphous competitive growth can occur in a relatively wide range of compositions of about $\Delta W = W_c - W_0 = 11.5$ at%. In the figure are also shown, with black points, the values of critical thickness calculated from the model as well as the values of thickness at which the surface coverage is lower than 1% (green points) and higher than 99% (orange points) calculated from extrapolation of the model. Consequently, even when working in the range of compositions that belongs to the biphased domain of the phase diagram, the film appears to be completely amorphous for thicknesses in the region marked with green dotted lines and, in fact, is completely amorphous in the region below h_c. Similarly, looking at the surface morphology, the film seems to be completely nanocrystalline for thicknesses in the region marked with orange dotted lines. This means that, due to composition-dependent kinetics and critical nucleation thickness, the peculiar biphased topography can easily be missed experimentally. Therefore, the presented model can serve as a platform for systematic studies on the nanocrystalline/amorphous and likely for other types of competitive growths in other systems if the relevant geometrical description is used.

5.5 Chapter conclusions

In this chapter, the nanocrystalline/amorphous competitive growth phenomenon was reported in the Zr-W system. We studied how this phenomenon develops for three different compositions. The evolution of the residual stress with thickness showed that the three zones already described in the previous chapter also occurs in the Zr-W system. Furthermore, the stress evolution with the surface coverage is the same in the Zr-Mo and the Zr-W systems (even for different compositions in the case of Zr-W), proving that the stress behavior is controlled by the proportion between the nanocrystalline and the amorphous phases.

A model capable of describing the kinetics of the nanocrystalline/amorphous competitive growth in thin films was developed. The model has two original aspects: First, the modular

kinetic model (MKM) approach used for 2D phase transformation can be adapted to successfully describe the kinetics of competitive growth in thin films. Second, owing to the geometry of the nanocrystalline phase, the density of nuclei and surface coverage of nanocrystalline phase can be related to the film thickness. The model shows that the density of nucleation sites, critical thickness for nucleation and type of nucleation (grain boundary or random) are composition-dependent. Finally, a phase diagram is proposed that shows that, despite the existence of a wide composition range for the nanocrystalline/amorphous competitive growth, the dependency to the film thickness can easily hide the phenomenon in experiments. Hence, this model highlights the interest of careful investigation to track the same phenomenon in other systems.

Chapter 6

Near the edge of crystalline-to-amorphous transition: From massive monocrystalline grains to crystalline/amorphous competitive growth in thin films
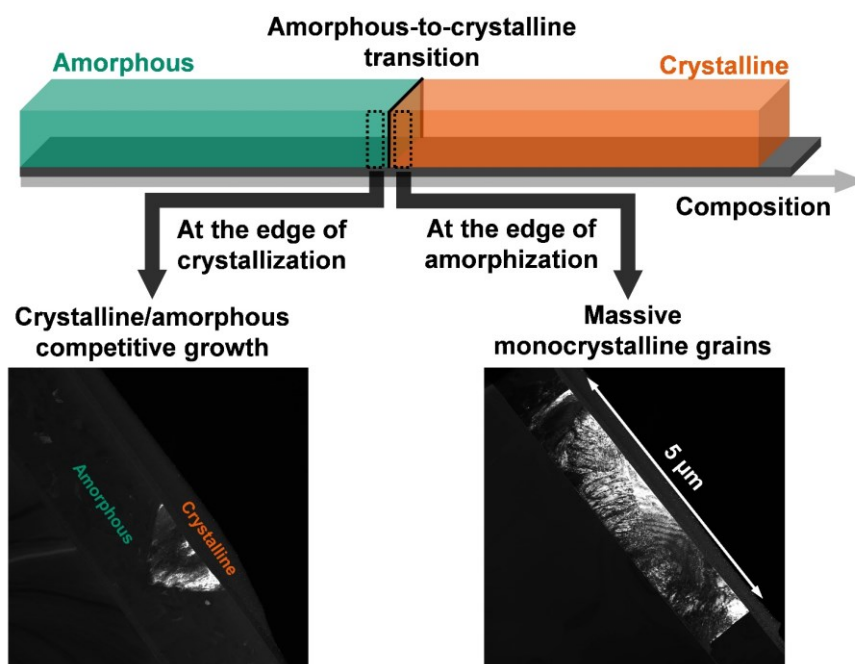
ABSTRACT: In this chapter, we explore the effect of working at low Ar pressure on the microstructure of sputter-deposited Zr-Mo thin films. Two series of depositions were performed: single-layer films deposited at 0.5 Pa, and bi-layer films consisting of a bottom layer deposited at 2 Pa and a top layer deposited at 0.5 Pa. In single-layer films, massive monocrystalline grains with lateral size larger than 1 μm were obtained when working near to the composition of the crystalline-to-amorphous transition. On the other hand, in bi-layer films the crystalline/amorphous competitive growth phenomenon was observed. In this case, the geometrical shape of the crystalline phase was similar to those reported in TiO_2, supporting that crystalline/amorphous competitive growth is more general and can be extended to other systems.

Contents

6.1 Introduction

The two previous chapters have been devoted to the study of the nanocrystalline/amorphous competitive growth phenomenon in the Zr-Mo and Zr-W systems. In both cases, the films obtained have been deposited at high working argon pressure (2 Pa for the Zr-Mo and 3 Pa for the Zr-W films). In this chapter, we propose to study the consequences of decreasing the working pressure, which acts directly on the mobility of the adatoms. As already explained at the end of Chapter 4, an increase in adatom mobility can change the geometry of the crystalline regions and could be the reason of the hollow shape of the crystalline phase in the case of the TiO_2 system (see Figure 4.12(b)).

The residual stress in a thin film strongly influences its adhesive strength with the substrate. Films deposited at low working pressure frequently present cracking and delamination because the high compressive stress in the films. A way to reduce the thin film residual stress is the incorporation, between the film and the substrates, of a bottom layer deposited at high working pressure [122,123]. This bottom layer possess a lower density structure compared with that of the film (deposited at a lower pressure), and can act as a compliant layer reducing the stress in the film. This method has proven to be effective in reducing the residual stress for single element materials, such as W and Si [122,123]. In this chapter, we will employ this approach in Zr-Mo alloys. Thus, Zr-Mo thin films will be deposited with and without the compliant layer.

Here we prove that by decreasing the working pressure, the geometrical shape of the crystalline phase when growing in competition with the amorphous one can be changed. In addition, we demonstrate that another phenomenon occurs near the crystalline-to-amorphous transition: massive monocrystalline grains with lateral size larger than 1 μm can be obtained.

(a) Series 1 (single-layer) Series 2 (bi-layer)

(b)

	I_{Zr} (A)	I_{Mo} (A)	P_{Ar} (Pa)		Thickness (nm)
Series 1	0.3	0.1	0.5		1266
		0.2			1215
		0.3			1144
		0.32			1055
		0.35			517
		0.4			1192
		0.5			1165
		0.6			1177
		0.7			950
			Layer 1	Layer 2	
Series 2	0.3	0.1	2	0.5	1262
		0.2			1129
		0.3			1217
		0.32			1162
		0.35			1142
		0.4			1190
		0.5			1228
		0.6			1261
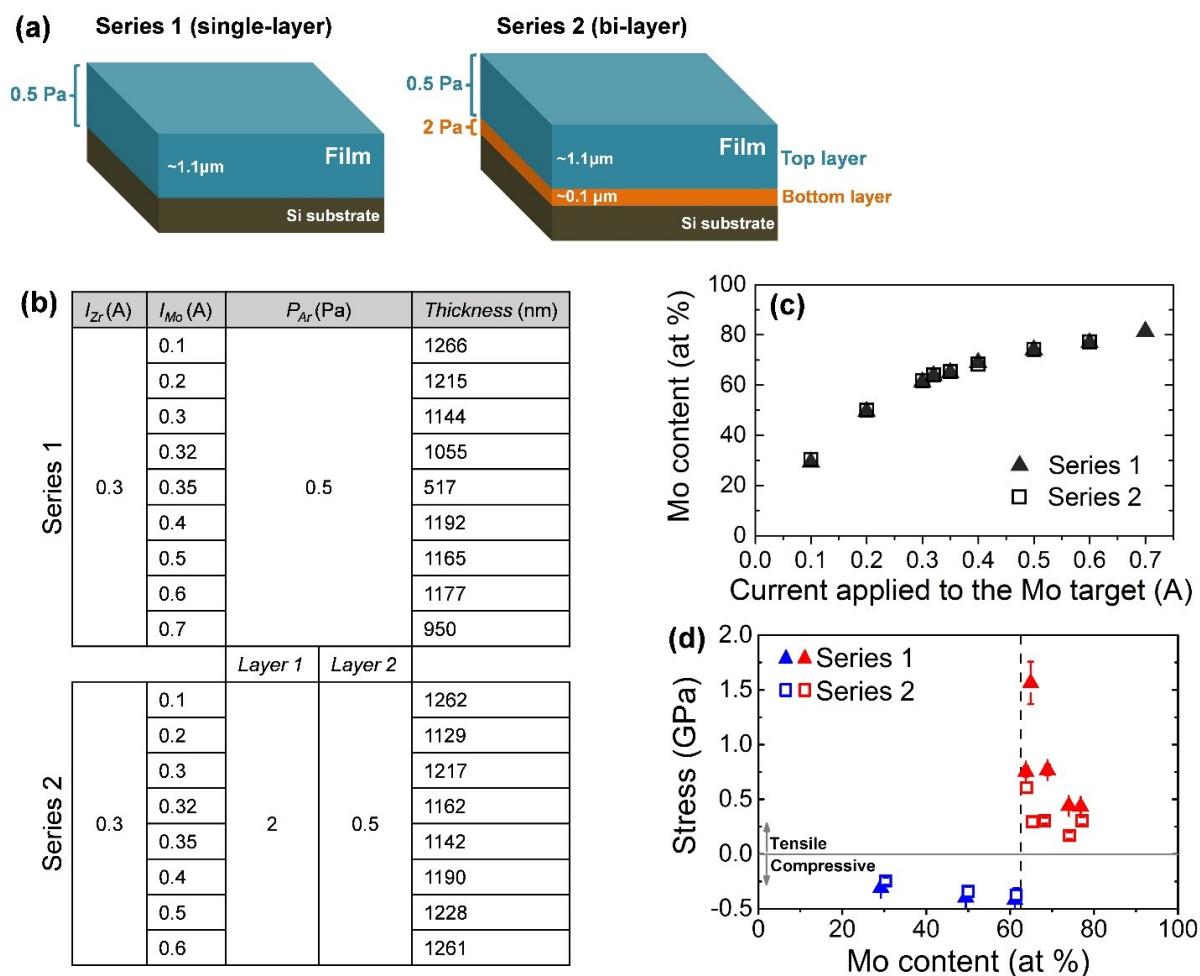
Figure 6.1. (a) Schematic of the two series of depositions performed. (b) Parameters used in the two series of depositions. (c) Evolution of the composition of the films as a function of the discharge current applied to the Mo target for the two series of depositions. (d) Dependency of in-plane residual stress with the Mo content.

6.2 Deposition conditions and stress evolution

In order to study the consequences of decreasing the working pressure on the structure of Zr-Mo films, two series of depositions were performed. In series 1, single-layer films with a nominal thickness of 1.1 μm were synthesized at a working argon pressure of 0.5 Pa. In series 2, bi-layer films were synthesized consisting of a first (bottom) layer deposited at a high working argon pressure of 2 Pa with a nominal thickness of 100 nm and, consecutively, a second (top) layer was deposited at 0.5 Pa and a nominal thickness of 1.1 μm. In Figure 6.1(a), a schematic of the two series of depositions performed is shown. In all cases, the targets-to substrate distance was fixed at 9 cm and the homogeneity of the films was ensured by rotating

the substrate holder during depositions. The composition of the films was controlled by varying the discharge current applied to the Mo and Zr targets. The values used as well as the thickness of the films synthesized are shown in Figure 6.1(b). Thus, films with compositions ranging from 29 to 81 at% Mo were obtained, as is shown in Figure 6.1(c).

In-plane residual stress measurements of the films obtained were performed and the results are shown in Figure 6.1(d). We point out here that the thickness of single-layer film obtained at I_{Mo}=0.35 A (65 at% Mo) was 517 nm. This is because at this composition the highest tensile stress is reached (see Figure 6.1(d)), consequently, films with this composition obtained at thicknesses larger than 1 µm were delaminated. The evolution of residual stress with composition evidences that a transition from a tensile to a compressive regime occurs between 61 and 64 at% Mo, corresponding to the compositions range of the crystalline-to-amorphous transition in the Zr-Mo system. We also notice that bi-layer films are more relaxed than single-layer films, i.e. they present lower tensile (or compressive) stress than single-layer films. This shows that the incorporation of the bottom layer of columnar morphology deposited at higher working pressure (2 Pa) effectively serves as compliant layer to the top one deposited at lower working pressure (0.5 Pa) [122,123]. Nevertheless, the marked differences in stress values between the single and bi-layer films when approaching to the composition of the tensile-to-compressive transition indicates that the bottom layer may also influence the evolution of the films microstructure. This will be investigated in more details in the next sections.

6.3 Structural evolution of single-layer films

The X-ray diffractograms in Figure 6.2(a) show that a transition from an amorphous to a crystalline structure occurs for a composition between 61 and 64 at% Mo, in line with the results obtained in previous chapters for films deposited at higher working pressure. Effectively, a wide diffraction signal corresponding to the amorphous phase is obtained for compositions between 29 and 61 at% Mo, while the signature of crystalline bcc Mo is obtained for Mo contents higher than 64 at%. However, no evidence of a coexistence of both signals, characteristic of the "milky region", was found for the compositions around the transition. In Figure 6.2(b), the evolution with Mo content of the volume fraction of grains with specific (*hkl*)

Figure 6.2. Structure and surface morphology of single-layer films. (a) X-ray diffractograms for the different Mo compositions. (b) Volume fraction of grains with specific (***hkl***) planes parallel to the substrate as a function of the Mo content. (c) Top-view SEM images for some of the compositions explored.

98

planes parallel to the substrate is shown. This fraction was calculated using eq. (2.2).

Figure 6.2(b) shows that the film with the higher Mo content (81 at%) presents a preferential out-of-plane (perpendicular to the substrate) orientation in the [110] direction. This is in line with the large number of works reporting a [110] out-of-plane fiber texture of sputter-deposited pure Mo thin films obtained at room temperature [124–131]. As Mo has a bcc structure, the [110] is the most compact orientation and, consequently, the (110) plane presents the lowest surface energy, which has been also confirmed by first-principles total-energy calculations [132]. Therefore, the texture in the [110] direction is often explained as an attempt to reach the thermodynamic most stable configuration, i.e. that in which the planes of lowest surface energy are parallel to the substrate. However, to achieve such configuration, high adatoms mobility is required and this is reached by working in zone II of the extended structure zone model [50]. For Mo films obtained at room temperature, the homologous temperature T_h is ~ 0.1, far from the range of temperature usually assumed for zone II ($T_h > 0.3$). In fact, the homologous temperature is within the zone I in which randomly oriented polycrystalline microstructure is expected [50]. Because of this, some authors have suggested to push down the lower end of zone II in the structure zone model to a homologous temperature of less than 0.1 [129]. Even so, the origin of preferred orientation of sputter-deposited pure Mo thin films in the [110] direction is not clear.

Decreasing the Mo content, from 77 to 74 at% Mo, the preferred orientation is changed to [310]-oriented planes but is not very pronounced. At 69 at% Mo, [310] and [200]-oriented grains dominate with equivalent proportion. This indicates that the incorporation of Zr atoms into the bcc structure of Mo acts against the tendency of Mo to grow with a [110] out-of-plane texture. TEM analysis performed to the film with 69 at% Mo (Figure 6.3(a)) shows that it exhibits a columnar microstructure. The X-ray diffractogram at this composition and the SAED pattern performed to a wide region of the film (green square in Figure 6.3(a)) reveal that, as a whole, the film is polycrystalline. Nevertheless, the SAED pattern performed on one of the columns (orange square in Figure 6.3(a)) shows that each of them is monocrystalline. The bright and dark field images show that the lateral size of the columns is ranging between 50 and 500 nm.

Figure 6.3. Microstructural evolution of single-layer films synthesized at compositions near to the amorphous transition. TEM images (left panels), SAED patterns of the regions marked with an orange circle in the TEM images (middle panels), and bright and dark field images (right panels) of films obtained at 69 (a), 65 (b) and 64 (c) at% Mo.

A surprising feature in the X-ray diffractograms is the significant increase of the signal intensity in the [100] direction while more Zr atoms are incorporated into the bcc structure of Mo and the composition approaches that of the transition to the amorphous structure. This is reflected in the sharp increase of the fraction of grains oriented in this direction at 65 and 64 at% Mo. The change to a marked preferential out-of-plane orientation in the [100] direction occurs together with a change in the surface morphology of the films, as can be seen in the top-view SEM images in Figure 6.2(c). In fact, the SEM images indicate that larger grains are formed while approaching to the amorphous transition. This is confirmed by TEM analysis performed to the films shown in Figure 6.3. Effectively, at 65 at% Mo (Figure 6.3(b)), the film microstructure is formed by massive monocrystalline grains (columns) with a lateral (parallel to the substrate) size larger than 1 µm (see bright and dark field images in Figure 6.3(b)). Although most of this monocrystalline grains are out-of-plane oriented in the [100] direction (as is the case of the one shown in Figure 6.3(b)), a fraction of them have other orientations, as can be seen in Figure 6.2(b). This situation drastically changes when increasing the Mo content by just 1 at% (Figure 6.3(c)), just at the edge of the amorphous transition. In this case, practically the whole film is [100]-oriented out-of-plane. Effectively, at 64 at% Mo, the film is formed by massive monocrystalline grains grown in the [100] direction and with lateral size as large as 5 µm (see bright and dark field images in Figure 6.3(c)). We point out here that no preferential in-plane orientation was found. The mechanisms of formation of the massive monocrystalline grains will be discussed in section 6.5.

6.4 Structural evolution of bi-layer films

The growth at high working pressure (2 Pa) of a thin bottom layer (~100 nm thickness) before the deposition of the top layer can strongly affects its structural evolution. This is evidenced in the X-ray diffractograms performed to the bi-layer films shown in Figure 6.4(a). As in the case of single-layer films, for Mo contents higher than 64 at%, the films are crystalline, showing the characteristic peaks of the bcc structure of Mo shifted with respect to those of pure Mo due the incorporation of Zr atoms into the crystal lattice of Mo. However, the evolution of the fraction of grains with specific (hkl) planes parallel to the substrate shown in Figure 6.4(b)
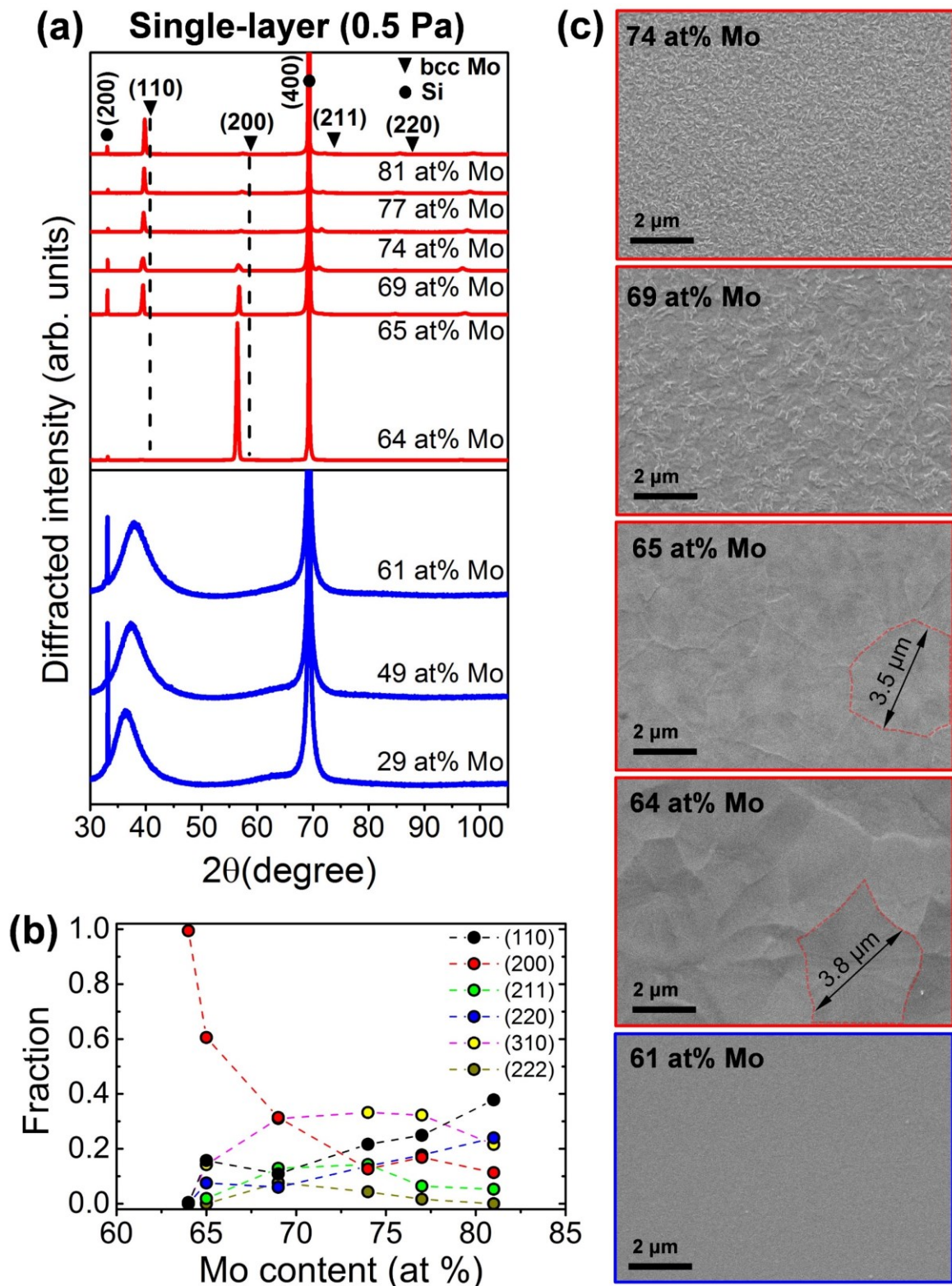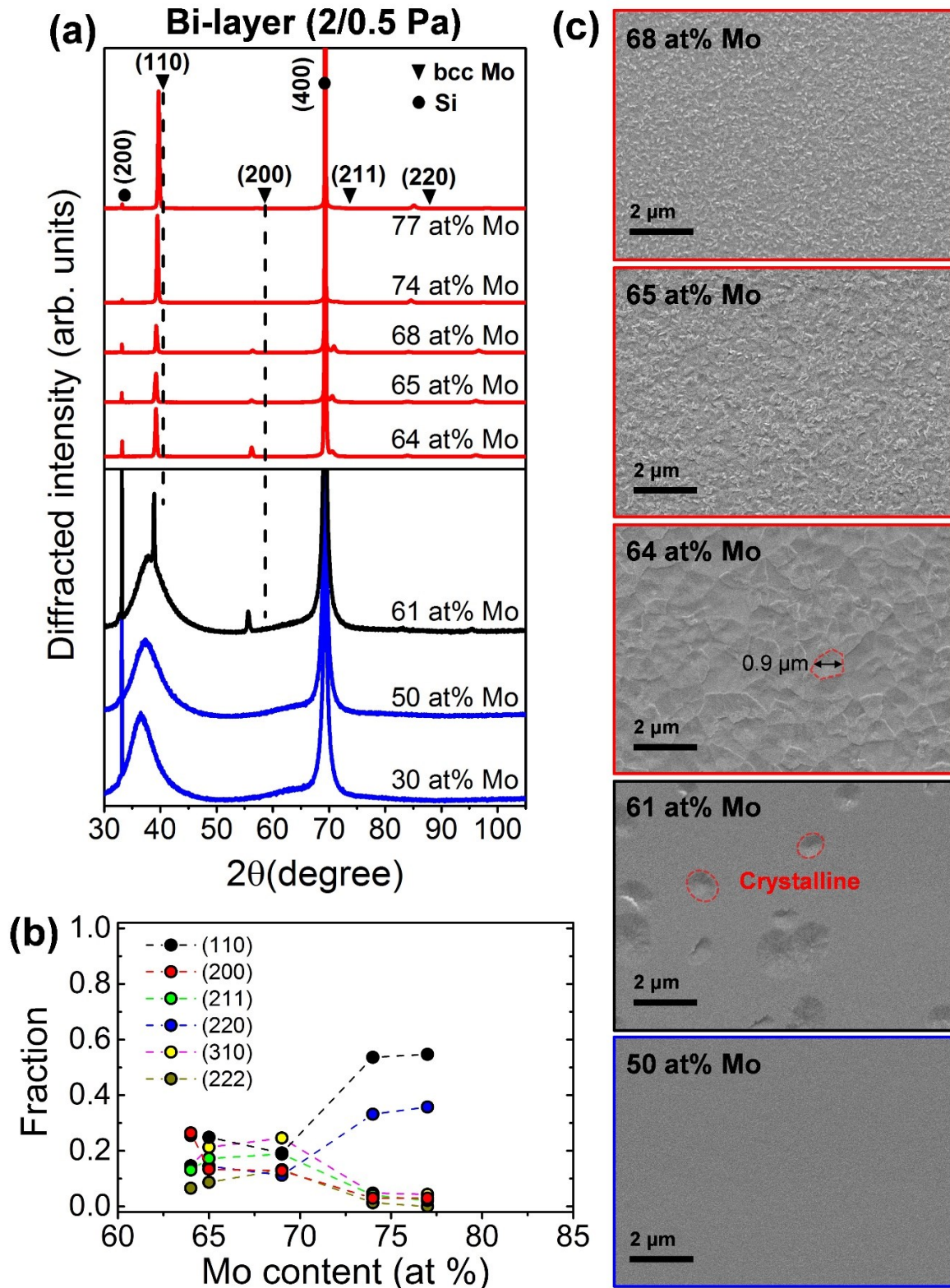
Figure 6.4. Structure and surface morphology of bi-layer films. (a) X-ray diffractograms for the different Mo compositions. (b) Volume fraction of grains with specific (***hkl***) planes parallel to the substrate as a function of the Mo content. (c) Top-view SEM images for some of the compositions explored.
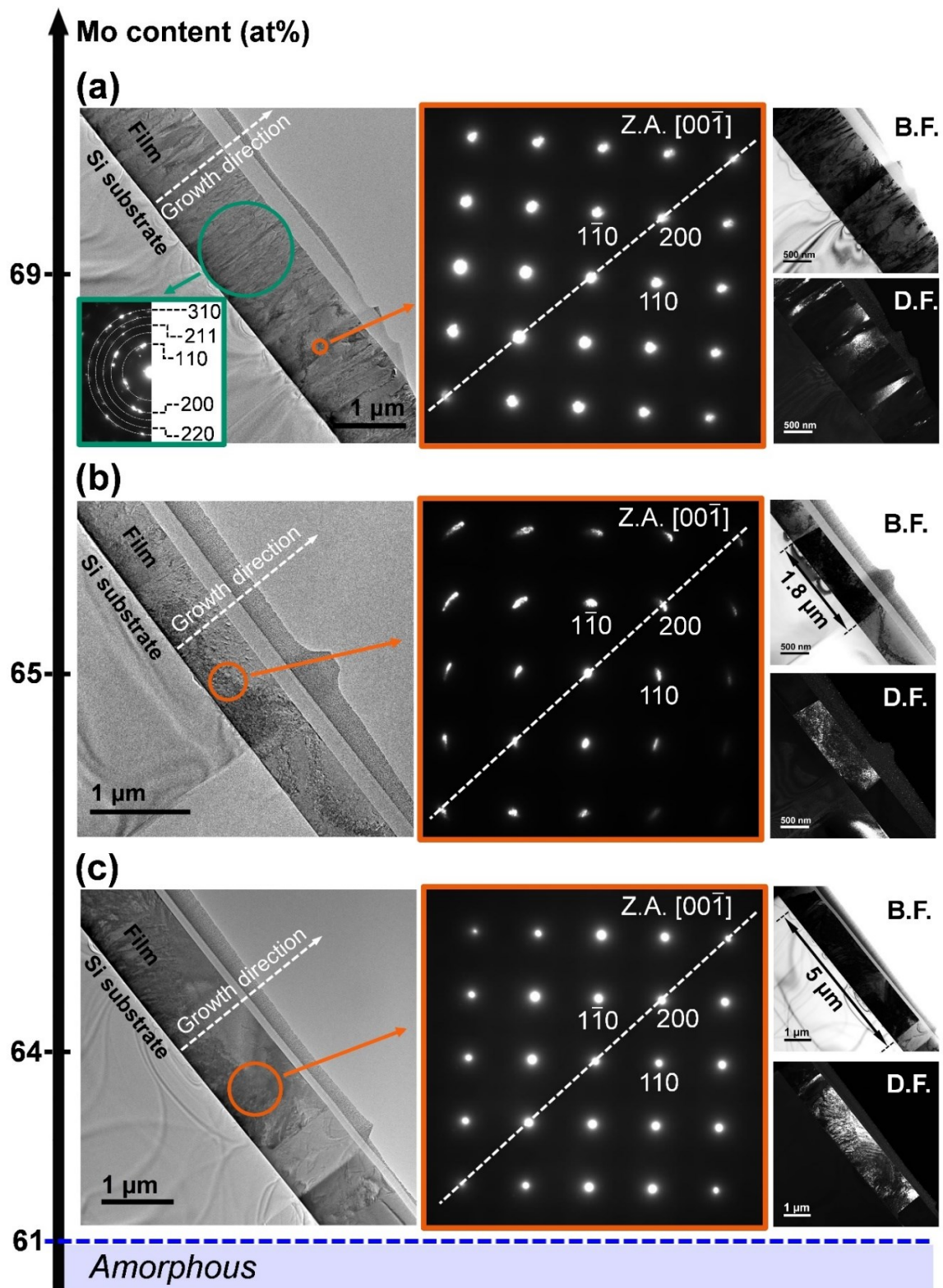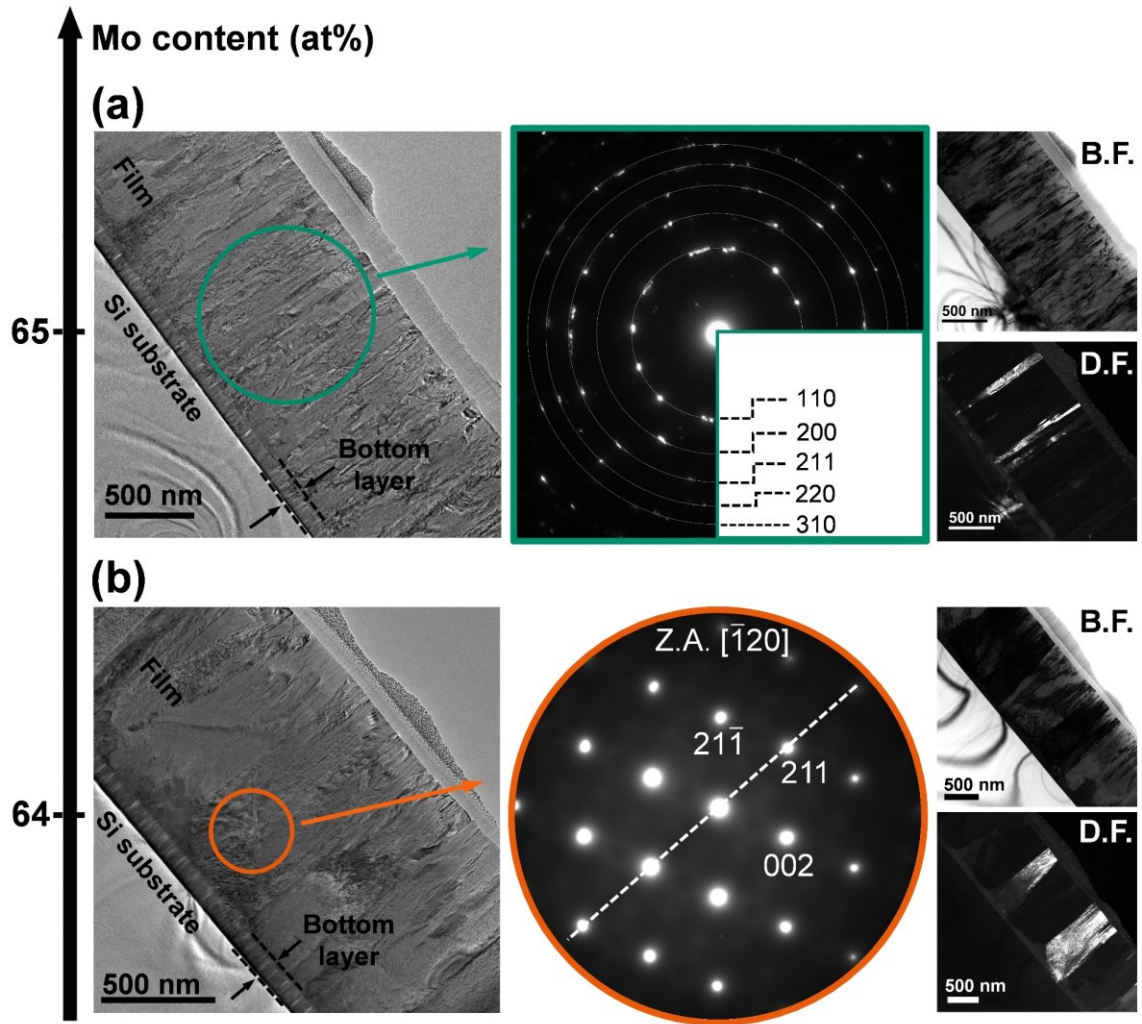
Figure 6.5. Microstructural evolution of bi-layer films synthesized at compositions near to the amorphous transition. TEM images (left panels), SAED patterns of the regions marked in the TEM images (middle panels), and bright and dark field images (right panels) of films obtained at 65 (a) and 64 (c) at% Mo.

is different from that presented in Figure 6.2(b) for single-layer films. Decreasing the Mo content (approaching to the composition of the amorphous transition) the films present a change from a marked out-of-plane orientation in the [110] direction (77 and 74 at% Mo) to a quasi-random out-of-plane orientation (from 68 to 64 at% Mo). The SEM top-view images shown in Figure 6.4(c) indicate that, such as in the case of single-layer films, the surface morphology of the films change when approaching to the amorphous transition. The TEM analyzes performed to the films with 65 at% Mo (Figure 6.5(a)) and 64 at% Mo (Figure 6.5(b)) show that these films present a columnar microstructure. Each of these columns are monocrystalline, but the
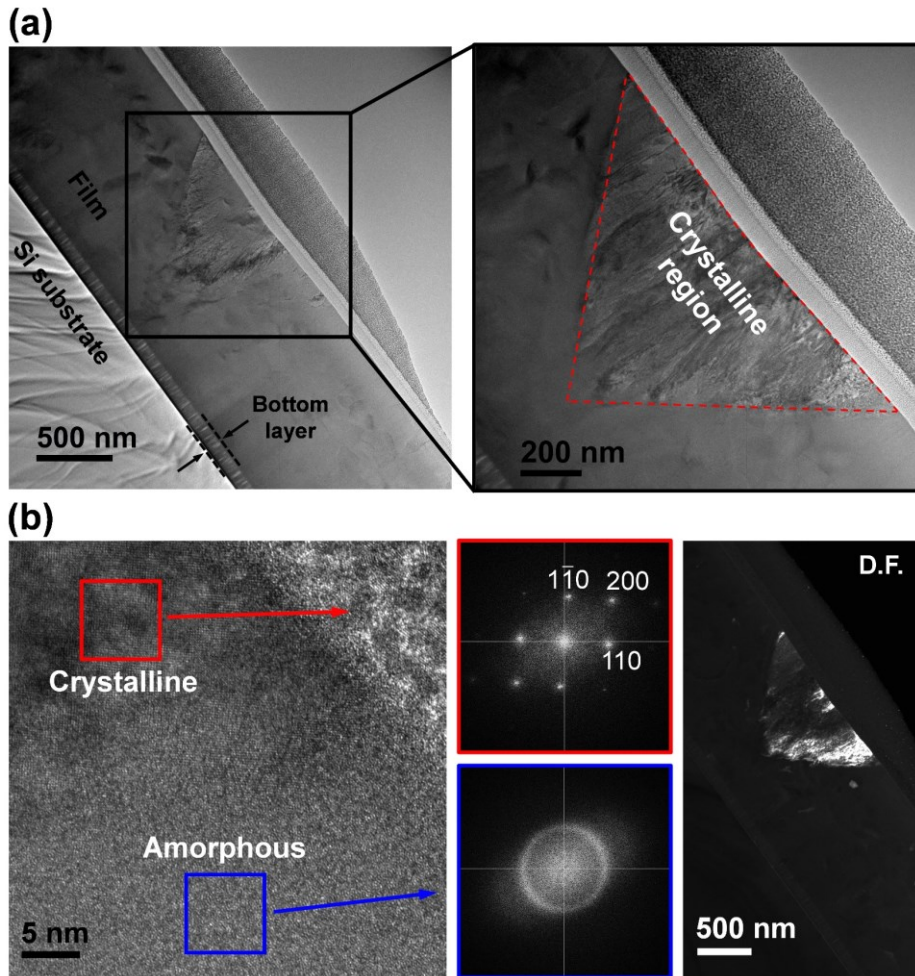
Figure 6.6. TEM analysis performed to the bi-layer film obtained at 61 at% Mo showing the crystalline/amorphous competitive growth phenomenon. (a) TEM image (left panel) and a zoom (right panel) showing the geometrical shape of the crystalline phase. (b) HRTEM image (left panel), FFT from the regions highlighted in the HRTEM image (middle panels), and dark field image (right panel) of the film.

films as a whole are polycrystalline. The typical lateral size of the columns observed in the film closest to the amorphous side (64 at% Mo) is less than 1 μm (coincident with SEM observations), much lower than that presented for the single-layer film of the same composition.

Besides the microstructural differences between the single and bi-layer films described above for compositions belonging to the crystalline side, the amorphous side presents also one important difference. For the composition closest to the transition to crystalline structure in single-layer film (61 at% Mo), the X-ray diffractogram shows that a mixture of the signal of crystalline bcc Mo and the wide diffraction signal corresponding to the amorphous phase is obtained in bi-layer film. This was not observed in the case of single-layer film and it is an

indication that the competitive growth between the crystalline and the amorphous phases (see Chapter 4) could be present at this composition. Effectively, the SEM top-view image (Figure 6.4(c)) shows the presence of regions with a rounded shape on the surface of the film. The TEM cross-sectional view shown in Figure 6.6(a) and the dark field image shown in Figure 6.6(b) reveal that they are conical inside the bulk of the film. In addition, the FFT analysis performed in this region and the region that surrounds it confirm their crystalline or amorphous character, respectively (see Figure 6.6(b)).

Thus, crystalline/amorphous competitive growth is also obtained at low argon pressure. The difference between working at 2 Pa or at 0.5 Pa is that at higher pressure the crystalline phase grows with a dome-like shape at the surface (see Chapter 4) while at lower pressure the crystalline phase exhibits a hollow-like shape at the surface (see Figure 6.6(a)). As already explained in Chapter 4, such difference can be understood considering that, decreasing the working pressure, the growth rate of the crystalline phase in the in-plane direction with reference to the vertical one increases due to an improved mobility of adatoms. Therefore, our results demonstrate that the geometrical shape of the crystalline phase when growing in competition with the amorphous one can be modified by changing the working pressure. The similarity between the results presented in Figure 6.6 and that reported in TiO_2 (see Figure 4.12(b)) demonstrates that in both cases the crystalline/amorphous competitive growth occurs, supporting that this phenomenon is more general and can be extended to other systems.

6.5 Discussion

Two particular structural features have been presented so far when working near the amorphous-to-crystalline transition. First, massive monocrystalline grains are obtained by approaching the transition from the crystalline side. Second, the crystalline/amorphous competitive growth phenomenon is obtained by approaching the transition from the amorphous side. In the following, the mechanism provoking the growth of the massive monocrystalline grains will be proposed. The double role of incorporating a bottom layer will also be addressed: on the one hand, it acts as an inhibitor of the growth of the massive monocrystalline grains and, on the other, it favors the crystalline/amorphous competitive growth phenomenon.

The increase in the width of monocrystalline columns as we approach to the amorphous transition indicates that the density of grains nucleated in the early growth stages (before coalescence) decreases with the incorporation of Zr atoms into the bcc structure of Mo. In fact, this is somehow expected taking in consideration that the destabilizing role of Zr atoms can inhibit the crystallization to the point that with sufficient Zr content the films become amorphous. Thus, at the edge of the amorphous transition, the nucleation is more difficult. Consequently, the density of grains in the early growth stages is lower, allowing them to reach larger size, such as that presented by the massive monocrystalline grains shown in Figure 6.3(c). We point out that this mechanism might be extrapolated to other systems in which a transition from a crystalline solid solution to an amorphous phase occurs. Nevertheless, as far as we know, there are no other reports on the synthesis of the massive monocrystalline grains presented here. We believe this is because two conditions are necessary to obtain this phenomenon. First, it is observed when working at compositions that are really close to the amorphous transition. For example, in the case of the Mo(Zr) solid solution, for compositions higher than 5 at% away from the transition, it is not observed. Second, besides the density of grains nucleated in the early stages of growth, the final size of the monocrystalline columns is determined also by the growth rate of these grains in the in-plane direction. Thus, even though the density of grains decreases as we approach to the amorphous transition, if the growth rate of these grains in the in-plane direction is too low, other grains may appear, inhibiting the growth of the former. In fact, in the case of the Mo(Zr) solid solution obtained at a higher working pressure (2 Pa), the massive monocrystalline grains do not appear. Precisely, this is because increasing the working pressure, the energy of the arriving adatoms decreases and, consequently, the growth rate in the in-plane direction also decreases.

Interestingly, the massive monocrystalline grains grow with a preferential [100] out-of-plane orientation. It is worth to note that in sputter-deposited Mo thin films, a [100] out-of-plane orientation has not been reported so far, even though this is the geometrically fastest growing direction in a bcc structure. This means that it should be the ultimate out-of-plane orientation after evolutionary selection if Mo films are obtained under zone T conditions [50]. However, the boundaries of the massive monocrystalline grains obtained here are straight and

perpendicular to the substrate, without evidence of a competitive growth. Thus, we can discard the evolutionary selection as the origin of the [100] out-of-plane orientation for the films obtained for compositions at the edge of the transition to the amorphous phase. At this point it is not clear why the [100] orientation is favored.

The incorporation of a bottom layer prior to the deposition of the top layer has two effects: first, the size reached by the monocrystalline columns decreases as we approach to the amorphous transition and, second, the crystalline/amorphous competitive growth phenomenon is observed. These results are pointing to the conclusion that the bottom layer is favoring the nucleation of the crystalline grains. Thus, for compositions deep in the crystalline side, the density of grains nucleated in the early growth stages of the top layer is greater than that presented by the single-layer films. Consequently, a smaller size of the monocrystalline columns is obtained in comparison with that obtained in single-layer films. Near the amorphous side, the crystalline/amorphous competitive growth phenomenon can be obtained in bi-layer films due to the role of the bottom layer as a trigger for nucleation of the crystalline phase.

The mechanism through which the bottom layer is favoring the nucleation could be the formation of a higher number of grain boundaries. Effectively, because this layer is deposited at a high working pressure, it possesses a high density of grain boundaries as can be seen in the TEM images of Figure 6.5 and Figure 6.6(a). As noted in previous chapters, the grain boundaries are important for the nucleation of the crystalline phase in the crystalline/amorphous competitive growth phenomenon. The lack of grain boundaries in the amorphous phase when films are deposited at low working pressure could be the reason why the crystalline/amorphous competitive growth phenomenon is not detected in single-layer films. However, by depositing the bottom layer first, the grain boundaries already created could propagate through the top layer, favoring the nucleation of the crystalline phase.

6.6 Chapter conclusions

In this chapter, we investigate the consequences of decreasing the working pressure on the structural evolution around the crystalline-to-amorphous transition in sputter-deposited Zr-Mo thin films. To this end, two series of depositions were performed. In series 1, single-layer films

were synthesized at a working argon pressure of 0.5 Pa and a nominal thickness of 1.1 μm. In series 2, bi-layer films were synthesized consisting of a first layer deposited at a high working argon pressure of 2 Pa with a nominal thickness of 100 nm and, consecutively, a second layer was deposited at 0.5 Pa and a nominal thickness of 1.1 μm. In both cases, for compositions higher than 64 at% Mo (crystalline side) the films showed the signature of the bcc structure of Mo with the peaks shifted due to the incorporation of Zr atoms, Mo(Zr) solid solution. For compositions lower than 61 at% Mo (amorphous side) a wide diffraction signal corresponding to the amorphous phase was detected, except for the case of bi-layer film with the composition closest to the crystalline transition (61 at% Mo). For this film, the X-ray diffractogram shows a mixture of the amorphous and the crystalline signals, indicating that competitive growth between the crystalline and the amorphous phases is occurring at this composition. In more details, the structural evolution of single and bi-layer films in the crystalline and amorphous sides can be summarized as follows:

Single-layer films: In the crystalline side, decreasing the Mo content, the out-of-plane orientation of the films can be divided in three stages. At 81 at% Mo, the film showed a preferential [110] out-of-plane orientation, from 77 to 69 at% Mo there is no clear preferential orientation and finally, at 65 and 64 at% Mo, just at the edge of the transition to amorphous structure, a marked preferential out-of-plane orientation in the [100] direction occurs. The films showed a columnar microstructure whose lateral size sharply increases when approaching to the amorphous transition. This happens to the point that at 64 at% Mo the film is constituted by massive monocrystalline grains with lateral size as large as 5 μm. In the amorphous side, the crystalline/amorphous competitive growth phenomenon was not detected.

Bi-layer films: In the crystalline side, decreasing the Mo content, the films evolve from a marked out-of-plane orientation in the [110] direction at 77 and 74 at% Mo to a quasi-random out-of-plane orientation from 68 to 64 at% Mo. The films showed a columnar microstructure whose lateral size also increases when approaching to the amorphous transition. Differently to single-layer films, the transition to the out-of-plane orientation in the [100] direction was not observed and the large lateral size of the columns do not reach the level reached in the first case.

Close to the amorphous side (61 at% Mo), the crystalline/amorphous competitive growth phenomenon was observed.

All the results presented above can be explained considering, first, that increasing the Zr content, the nucleation in the bcc structure of Mo becomes more difficult. Consequently, there are fewer crystalline grains and those that nucleate can grow wider. In the limit case, at the edge of the transition to amorphous phase, the crystalline grains reach their maximum size. On the other hand, growing a bottom layer before the top layer favors the nucleation and, consequently, smaller crystalline columns are obtained when working in the crystalline side. In the same way, the nucleation of crystalline phase is favored when working close to the amorphous side, allowing the crystalline/amorphous competitive growth phenomenon to occur.

Finally, our results demonstrate that the geometrical shape of the crystalline phase, when working at compositions in which the crystalline/amorphous competitive growth phenomenon occurs, can be modified by changing the working pressure. Thus, the similarity between the results presented here and those reported in TiO_2 [94] demonstrate that in both cases the crystalline/amorphous competitive growth occurs, supporting that this phenomenon is more general and can be extended to other systems.

General conclusions

The aim of this thesis was to investigate sputter-deposited Zr-based binary thin film alloys for their microstructure and functional properties. It is shown that different types of original microstructures can be obtained by working around the crystalline-to-amorphous transition in sputter-deposited Zr-Mo and Zr-W thin films.

A schematic showing the different microstructural features obtained in this thesis is presented in Figure I. In both studied systems, a transition from a crystalline solid solution of Zr into the bcc lattice of Mo (or W) to an amorphous structure was achieved by changing the film composition. We can distinguish what occurs depending on the deposition pressure, a parameter known to modify the mobility of adatoms and, thereby, the microstructure.

At high deposition pressure, corresponding to conditions prone to limit the mobility of adatoms, we showed that by working at compositions intermediate to those necessary to form single-phased amorphous and nanocrystalline films, a self-separation of the nanocrystalline and the amorphous phases occurs (see schematic in Figure I(a)). Hence, bi-phased films are formed in which amorphous and nanocrystalline phases grow in competition. This results in the possibility to tune the surface roughness. We developed a model in which Avrami nucleation is assumed, derived from the modular kinetic model for 2D transformations and capable of describing the kinetics of this competitive growth phenomenon. In particular, this model was applied to the Zr-W system. It allowed fitting experimental data on the evolution of the density of nuclei and surface coverage of the nanocrystalline phase as a function of the film thickness. Based on this model, a composition-thickness phase diagram was proposed showing that despite the occurrence of the nanocrystalline/amorphous competitive growth in a wide range of compositions, the dependency to the film thickness can easily hide the phenomenon in experiments.

At low deposition pressure the competitive growth phenomenon was not observed in the range of composition studied. However, its existence is not completely rule out. We believe that this regime can exist but in a very narrow composition range close to the amorphous-to-nanocrystalline transition. On the other hand, massive monocrystalline grains with lateral size
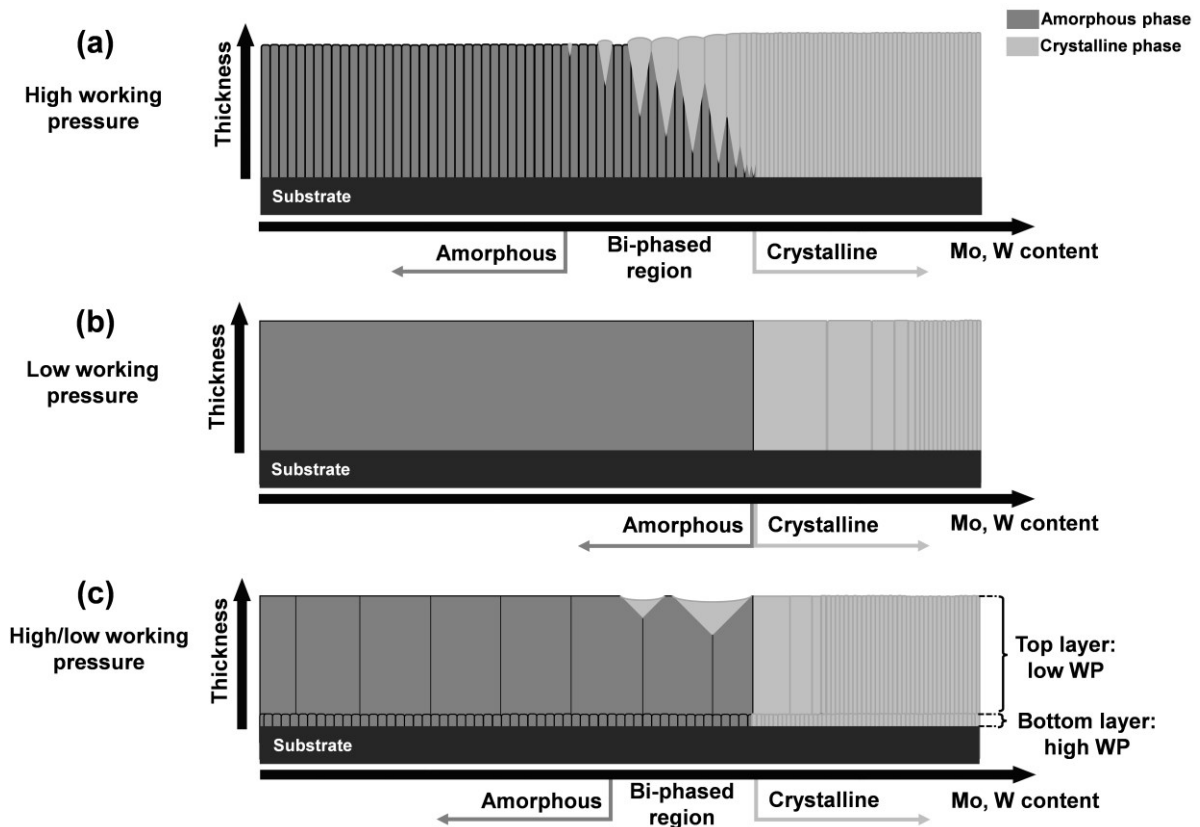
Figure I. Schematic of the different structural features obtained in this thesis.

larger than 1 μm were obtained near the crystalline-to-amorphous transition (see schematic in Figure I(b)). The formation of these massive monocrystalline grains was explained on the basis of the role of Zr as destabilizer of the nucleation process, which leads to a limited number of nucleation sites at the surface. Therefore, the growth of the nuclei is less limited by the presence of near neighbors, allowing the grains to grow wider.

The dynamic of the growth process al low pressure can be changed by incorporating a bottom layer deposited at higher pressure (see Figure I(c)), i.e. exhibiting a columnar structure. It is shown that this bottom layer triggers the nucleation process of the crystalline phase thanks to the presence of interfaces between columns. This has two main consequences. First, when approaching to the transition from the crystalline side, the grain size is reduced in comparison to the situation in absence of the columnar bottom layer and, as a consequence, the massive monocrystalline grains are not observed. Second, the crystalline/amorphous competitive growth appears, when approaching to the transition from the amorphous side. However, the geometry of the crystalline phase is different from that obtained at high working pressures. When working

at high pressure, the crystalline phase grows with a dome-like shape at the surface, while at lower pressure it exhibits a hollow-like shape, which is explained on the basis of different adatoms mobility at different working pressures.

Regarding the properties of the Zr-Mo thin films, it was shown that the films exhibit improved mechanical properties compared with bulk of Zr and Mo: higher hardness, higher *H/E* ratio and low friction coefficient. Moreover, the occurrence of the nanocrytalline/amorphous competitive growth phenomenon was exploited as a way to modulate the optical reflectance of the films to a large extent. Effectively, the particular geometry in which the nanocrystalline phase grows in competition with the amorphous one was used to control the surface roughness and, consequently, the film reflectance.

Perspectives

- We believe that the crystalline/amorphous competitive growth presented here for Zr-Mo and Zr-W thin films is a more general phenomenon that can be obtained in other binary alloys presenting a composition-driven transition and that can be extrapolated to other systems such as TiO_2. We could observe this phenomenon by carefully investigating the microstructure in a wide range of compositions but with small intervals and by varying the film thickness. As evidenced by the kinetic model we proposed, the transition can be easily hidden experimentally. It is likely that re-investigating other systems known to exhibit composition-driven crystalline-amorphous transition would enable to find the same behavior.

- The possibility to modulate the surface morphology at the biphased composition by changing the film thickness can be exploited to control the surface-related properties. For example, the wettability of a solid surface is dominated by both its surface free energy and its geometric structure (or surface roughness). Therefore, by selecting an adequate system (in which the competitive self-phase separation phenomenon occurs) and subsequently controlling the thickness of the film, both the free energy and the surface roughness could be modified and, hence, modulate the surface wettability.

- Another possible route to functionalize films that exhibit the competitive self-phase separation phenomenon is the ability to control the size and number of "grains" formed by the nanocrystalline regions. Thus, by changing the film thickness, the number of contact points with a reciprocating surface can be changed and, consequently, the friction behavior may be controlled.

- Provided the amorphous and crystalline phases present different properties, their competitive growth could be exploited to tune their relative contributions by simply changing the film thickness.

Appendix

Image processing: Extraction of surface coverage and nuclei density from SEM images

The surface coverage by the nanocrystalline phase (Chapter 4, section 4.3 and Chapter 5, section 5.4) and the density of nanocrystalline nuclei (Chapter 5, section 5.4) were determined by processing surface SEM images. The images were treated using the image-processing program Image J. In Figure AI are shown the different steps done in order to convert the original SEM image in a black and white image in which the black zones represent the nanocrystalline regions and the white zones represent the amorphous regions. First, a *Bandpass Filter* was applied to the SEM image, which allows better delimiting the nanocrystalline and amorphous phases. After, a carefully selection of a *Threshold* was done in order to convert the image in a black and white image. Then, the boundaries delimiting neighboring nanocrystalline nuclei in contact were manually marked. This permits to apply a *Fill Holes* function, yet keeping the nanocrystalline nuclei correctly separated. After that, the nuclei can be counted in a proper way and the surface coverage calculated straightforward by the program.
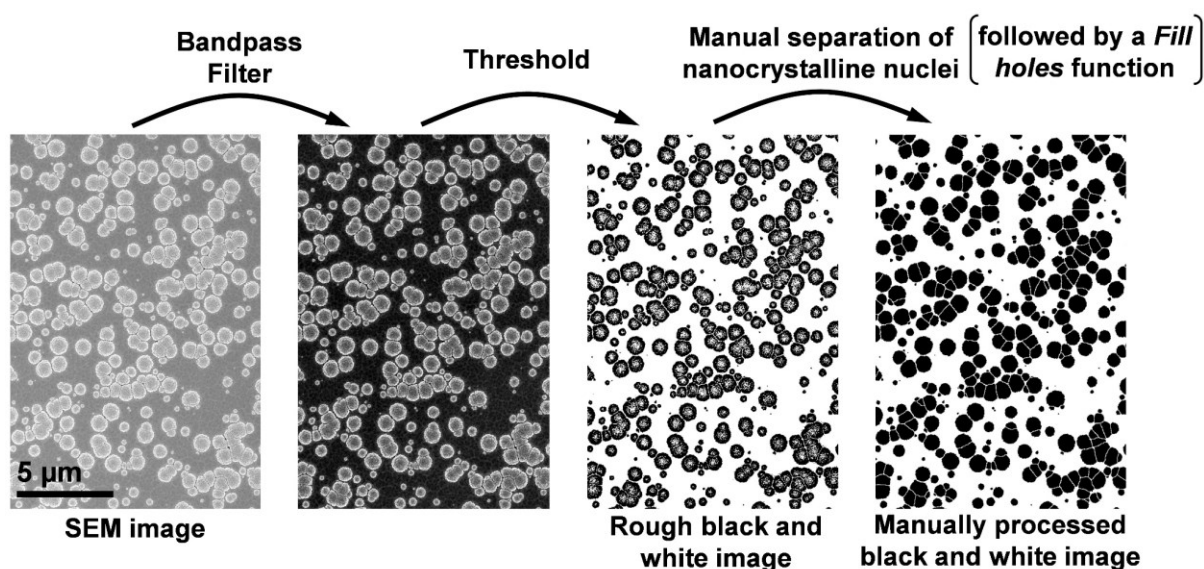

Figure AI. SEM image treatment to determine the surface coverage by the nanocrystalline phase and the density of nanocrystalline nuclei.

Bibliography

[1]   P.Y. Park, E. Akiyama, H. Habazaki, A. Kawashima, K. Asami, K. Hashimoto, The corrosion behavior of sputter-deposited amorphous Mo-Zr alloys in 12 M HCl, Corros. Sci. 37 (1995) 307–320. doi:10.1016/0010-938X(94)00139-W.

[2]   Z.Z. Tang, J.H. Hsieh, S.Y. Zhang, C. Li, Y.Q. Fu, Phase transition and microstructure change in Ta–Zr alloy films by co-sputtering, Surf. Coat. Technol. 198 (2005) 110–113. doi:10.1016/j.surfcoat.2004.10.019.

[3]   D. Horwat, M. Dehmas, E. Aubry, J. Zollinger, S. Migot, J.F. Pierson, Properties of nanocrystalline and nanocomposite W_xZr_{1-x} thin films deposited by co-sputtering, Intermetallics. 17 (2009) 421–426. doi:10.1016/j.intermet.2008.11.020.

[4]   P. Zeman, M. Zítek, Š. Zuzjaková, R. Čerstvý, Amorphous Zr-Cu thin-film alloys with metallic glass behavior, J. Alloys Compd. 696 (2017) 1298–1306. doi:10.1016/j.jallcom.2016.12.098.

[5]   K. Edalati, Z. Horita, Correlations between hardness and atomic bond parameters of pure metals and semi-metals after processing by high-pressure torsion, Scr. Mater. 64 (2011) 161–164. doi:10.1016/j.scriptamat.2010.09.034.

[6]   J.H. Rose, H.B. Shore, Valence of the Elemental Transition Metals, Aust. J. Phys. 53 (2000) 167. doi:10.1071/PH99039.

[7]   J. Bhattarai, E. Akiyama, H. Habazaki, A. Kawashima, K. Asami, K. Hashimoto, Electrochemical and xps studies of the corrosion behavior of sputter-deposited amorphous W-Zr alloys in 6 and 12 M HCl solutions, Corros. Sci. 39 (1997) 355–375. doi:10.1016/S0010-938X(97)83351-3.

[8]   D. Horwat, E. Jimenez-Pique, J.F. Pierson, S. Migot, M. Dehmas, M. Anglada, High hardness, low Young's modulus and low friction of nanocrystalline ZrW_2 Laves phase and $Zr_{1-x}W_x$ thin films, J. Phys. Chem. Solids. 73 (2012) 554–558. doi:10.1016/j.jpcs.2011.12.009.

[9]   R.F. Domagala, D.J. McPherson, M. Hansen, Systems Zirconium-Molybdenum and Zirconium-Wolfram, JOM. 5 (1953) 73–79. doi:10.1007/BF03397454.

[10]   S.P. Garg, R.J. Ackermann, The high temperature phase diagrams for zirconium-molybdenum and hafnium-molybdenum, Metall. Trans. A. 8 (1977) 239–244. doi:10.1007/BF02661635.

[11]   M. Zinkevich, N. Mattern, Thermodynamic assessment of the Mo-Zr system, J. Phase Equilibria. 23 (2002) 156–162. doi:10.1361/1054971023604242.

[12]   R. Jerlerud Pérez, B. Sundman, Thermodynamic assessment of the Mo–Zr binary phase diagram, Calphad. 27 (2003) 253–262. doi:10.1016/j.calphad.2003.09.003.

[13]   X.-K. Liu, W. Zhou, Z. Zheng, S.-M. Peng, The elastic and thermodynamic properties of $ZrMo_2$ from first principles calculations, J. Alloys Compd. 615 (2014) 975–982. doi:10.1016/j.jallcom.2014.07.063.

[14]   N. Turkdal, E. Deligoz, H. Ozisik, H.B. Ozisik, First-principles studies of the structural, elastic, and lattice dynamical properties of $ZrMo_2$ and $HfMo_2$, Phase Transit. 90 (2017) 598–609. doi:10.1080/01411594.2016.1252979.

[15]   L. Ma, Y. Duan, R. Li, Phase stability, anisotropic elastic properties and electronic structures of C15-type Laves phases ZrM_2 (M = Cr, Mo and W) from first-principles calculations, Philos. Mag. 97 (2017) 2406–2424. doi:10.1080/14786435.2017.1334135.

[16]   S.F. Pugh, XCII. Relations between the elastic moduli and the plastic properties of polycrystalline pure metals, Lond. Edinb. Dublin Philos. Mag. J. Sci. 45 (1954) 823–843. doi:10.1080/14786440808520496.

[17]   V. Sadagopan, E. Pollard, H.C. Gatos, Superconducting transition temperatures of $ZrMo_2$, HfV_2 and $PbAu_2$, Solid State Commun. 3 (1965) 97–98. doi:10.1016/0038-1098(65)90230-9.

[18]   Ö. Rapp, Superconductivity and lattice parameters in the zirconium-molybdenum, zirconium-tungsten, hafnium-molybdenum and hafnium-tungsten alloy systems, J. Common Met. 21 (1970) 27–44. doi:10.1016/0022-5088(70)90162-1.

[19]   K. Yasohama, T. Ogasawara, Specific Heat and Superconducting Properties of Zr-Mo Alloys, J. Phys. Soc. Jpn. 36 (1974) 1349–1355. doi:10.1143/JPSJ.36.1349.

[20]   Ö. Rapp, J. Invarsson, T. Claeson, Search for superconductivity in Laves phase compounds, Phys. Lett. A. 50 (1974) 159–160. doi:10.1016/0375-9601(74)90770-1.

[21]   V.L. Ginzburg, L.D. Landau, On the theory of superconductivity, J Exptl Theor. Phys USSR. 20 (1950) 1064.

[22]   V.L. Ginzburg, On superconductivity and superfluidity: a scientific autobiography, Springer-Verlag, Berlin, 2009.

[23]   J. Bardeen, L.N. Cooper, J.R. Schrieffer, Theory of Superconductivity, Phys. Rev. 108 (1957) 1175–1204. doi:10.1103/PhysRev.108.1175.

[24]   B.T. Matthias, T.H. Geballe, V.B. Compton, Superconductivity, Rev. Mod. Phys. 35 (1963) 1–22. doi:10.1103/RevModPhys.35.1.

[25]   Suyalatu, N. Nomura, K. Oya, Y. Tanaka, R. Kondo, H. Doi, Y. Tsutsumi, T. Hanawa, Microstructure and magnetic susceptibility of as-cast Zr–Mo alloys, Acta Biomater. 6 (2010) 1033–1038. doi:10.1016/j.actbio.2009.09.013.

[26]   Suyalatu, R. Kondo, Y. Tsutsumi, H. Doi, N. Nomura, T. Hanawa, Effects of phase constitution on magnetic susceptibility and mechanical properties of Zr-rich Zr–Mo alloys, Acta Biomater. 7 (2011) 4259–4266. doi:10.1016/j.actbio.2011.07.005.

[27]   F.Y. Zhou, B.L. Wang, K.J. Qiu, L. Li, J.P. Lin, H.F. Li, Y.F. Zheng, Microstructure, mechanical property, corrosion behavior, and in vitro biocompatibility of Zr–Mo alloys, J. Biomed. Mater. Res. B Appl. Biomater. 101B (2013) 237–246. doi:10.1002/jbm.b.32833.

[28]   F.Y. Zhou, K.J. Qiu, H.F. Li, T. Huang, B.L. Wang, L. Li, Y.F. Zheng, Screening on binary Zr–1X (X=Ti, Nb, Mo, Cu, Au, Pd, Ag, Ru, Hf and Bi) alloys with good in vitro cytocompatibility and magnetic resonance imaging compatibility, Acta Biomater. 9 (2013) 9578–9587. doi:10.1016/j.actbio.2013.07.035.

[29]   M. Ashida, T. Sugimoto, N. Nomura, Y. Tsutsumi, P. Chen, H. Doi, T. Hanawa, Microstructure and Mechanical Properties of Large-Scale Ingots of the Zr-1Mo Alloy, Mater. Trans. 56 (2015) 1544–1548. doi:10.2320/matertrans.M2015098.

[30]   X. Sun, W. Zhou, K. Kikuchi, N. Nomura, A. Kawasaki, H. Doi, Y. Tsutsumi, T. Hanawa, Fabrication and Characterization of a Low Magnetic Zr-1Mo Alloy by Powder Bed Fusion Using a Fiber Laser, Metals. 7 (2017) 501. doi:10.3390/met7110501.

[31]   A. Yamamoto, R. Honma, M. Sumita, Cytotoxicity evaluation of 43 metal salts using murine fibroblasts and osteoblastic cells, J. Biomed. Mater. Res. 39 (1998) 331–340. doi:10.1002/(SICI)1097-4636(199802)39:2<331::AID-JBM22>3.0.CO;2-E.

[32]   A. Mehjabeen, T. Song, W. Xu, H.P. Tang, M. Qian, Zirconium Alloys for Orthopaedic and Dental Applications, Adv. Eng. Mater. 20 (2018) 1800207. doi:10.1002/adem.201800207.

[33]   S.K. Sikka, Y.K. Vohra, R. Chidambaram, Omega phase in materials, Prog. Mater. Sci. 27 (1982) 245–310. doi:10.1016/0079-6425(82)90002-0.

[34]   R.F. Domagala, D.W. Levinson, D.J. McPherson, Transformation kinetics and mechanical properties of Zr-Mo alloys, JOM. 9 (1957) 1191–1196. doi:10.1007/BF03398287.

[35]   B. Heritier, J.J. Jonas, High temperature deformation of oxidized β-Zr-Mo alloys, Metall. Trans. A. 10 (1979) 557–567. doi:10.1007/BF02658318.

[36]   J. Fan, M. Lu, H. Cheng, J. Tian, B. Huang, Effect of alloying elements Ti, Zr on the property and microstructure of molybdenum, Int. J. Refract. Met. Hard Mater. 27 (2009) 78–82. doi:10.1016/j.ijrmhm.2008.03.006.

[37]   J. Becker, U. Betke, E. Wessel, M. Krüger, Alloying effects in Mo-5X (X=Zr, Ti,V) – Microstructural modifications and mechanical properties, Mater. Today Commun. 15 (2018) 314–321. doi:10.1016/j.mtcomm.2018.04.005.

[38]   J. Sakurai, S. Hata, R. Yamauchi, A. Shimokohbe, Evaluation of Mo-based Amorphous Alloy Thin Films Exhibiting High Crystallization Temperature, MRS Online Proc. Libr. Arch. 894 (2005). doi:10.1557/PROC-0894-LL03-07.

[39]   A. Borroto, S. Bruyère, N. Thurieau, C. Gendarme, E. Jimenez-Piqué, J.J. Roa, J.F. Pierson, F. Mücklich, D. Horwat, Structural and mechanical properties of $Zr_{1-x}Mo_x$ thin films: From the nano-crystalline to the amorphous state, J. Alloys Compd. 729 (2017) 137–143. doi:10.1016/j.jallcom.2017.09.153.

[40]   P. Zhou, Y. Peng, Y. Du, S. Wang, G. Wen, Thermodynamic modeling of the C–W–Zr system, Int. J. Refract. Met. Hard Mater. 50 (2015) 274–281. doi:10.1016/j.ijrmhm.2015.02.002.

[41]   N. Laegreid, G.K. Wehner, Sputtering Yields of Metals for Ar^+ and Ne^+ Ions with Energies from 50 to 600 ev, J. Appl. Phys. 32 (1961) 365–369. doi:10.1063/1.1736012.

[42]   K. Wasa, Sputtering Phenomena, in: Handb. Sputtering Technol., Elsevier, 2012: pp. 41–75. doi:10.1016/B978-1-4377-3483-6.00002-4.

[43]   A. Billard, F. Perry, Pulvérisation cathodique magnétron, Tech Ing Matér Métalliques. (2005).

[44]   R.D. Arnell, P.J. Kelly, Recent advances in magnetron sputtering, Surf. Coat. Technol. 112 (1999) 170–176. doi:10.1016/S0257-8972(98)00749-X.

[45]   P.J. Kelly, R.D. Arnell, Magnetron sputtering: a review of recent developments and applications, Vacuum. 56 (2000) 159–172. doi:10.1016/S0042-207X(99)00189-X.

[46]   G. Bräuer, B. Szyszka, M. Vergöhl, R. Bandorf, Magnetron sputtering – Milestones of 30 years, Vacuum. 84 (2010) 1354–1359. doi:10.1016/j.vacuum.2009.12.014.

[47]   D.A. Golosov, Balanced magnetic field in magnetron sputtering systems, Vacuum. 139 (2017) 109–116. doi:10.1016/j.vacuum.2017.02.018.

[48]   J.E. Greene, Chapter 12 - Thin Film Nucleation, Growth, and Microstructural Evolution: An Atomic Scale View, in: P.M. Martin (Ed.), Handb. Depos. Technol. Films Coat. Third Ed., William Andrew Publishing, Boston, 2010: pp. 554–620. doi:10.1016/B978-0-8155-2031-3.00012-0.

[49]   B.A. Movchan, A.V. Demchishin, Structure and properties of thick condensates of nickel, titanium, tungsten, aluminum oxides, and zirconium dioxide in vacuum, Fiz Met. Met. 28: 653-60 (1969). https://www.osti.gov/biblio/4181669.

[50]   S. Mahieu, P. Ghekiere, D. Depla, R. De Gryse, Biaxial alignment in sputter deposited thin films, Thin Solid Films. 515 (2006) 1229–1249. doi:10.1016/j.tsf.2006.06.027.

[51]   J.A. Thornton, Influence of apparatus geometry and deposition conditions on the structure and topography of thick sputtered coatings, J. Vac. Sci. Technol. 11 (1974) 666–670. doi:10.1116/1.1312732.

[52]   A. Anders, A structure zone diagram including plasma-based deposition and ion etching, Thin Solid Films. 518 (2010) 4087–4090. doi:10.1016/j.tsf.2009.10.145.

[53]   Bragg William Henry, Bragg William Lawrence, The reflection of X-rays by crystals, Proc. R. Soc. Lond. Ser. Contain. Pap. Math. Phys. Character. 88 (1913) 428–438. doi:10.1098/rspa.1913.0040.

[54]   S. Mahieu, P. Ghekiere, G. De Winter, S. Heirwegh, D. Depla, R. De Gryse, O.I. Lebedev, G. Van Tendeloo, Mechanism of preferential orientation in sputter deposited titanium nitride and yttria-stabilized zirconia layers, J. Cryst. Growth. 279 (2005) 100–109. doi:10.1016/j.jcrysgro.2005.02.014.

[55]   J.I. Langford, A.J.C. Wilson, Scherrer after sixty years: A survey and some new results in the determination of crystallite size, J. Appl. Crystallogr. 11 (1978) 102–113. doi:10.1107/S0021889878012844.

[56]   D.B. Williams, C.B. Carter, Transmission electron microscopy: a textbook for materials science, 2nd ed, Springer, New York, 2008.

[57]   G.G. Stoney, The Tension of Metallic Films Deposited by Electrolysis, Proc. R. Soc. Math. Phys. Eng. Sci. 82 (1909) 172–175. doi:10.1098/rspa.1909.0021.

[58]   G.C.A.M. Janssen, M.M. Abdalla, F. van Keulen, B.R. Pujada, B. van Venrooy, Celebrating the 100th anniversary of the Stoney equation for film stress: Developments from polycrystalline steel strips to single crystal silicon wafers, Thin Solid Films. 517 (2009) 1858–1867. doi:10.1016/j.tsf.2008.07.014.

[59]   H. Davies, The reflection of electromagnetic waves from a rough surface, Proc. IEE - Part IV Inst. Monogr. 101 (1954) 209–214. doi:10.1049/pi-4.1954.0025.

[60]   H.E. Bennett, J.O. Porteus, Relation Between Surface Roughness and Specular Reflectance at Normal Incidence, JOSA. 51 (1961) 123–129. doi:10.1364/JOSA.51.000123.

[61]   J.O. Porteus, Relation between the Height Distribution of a Rough Surface and the Reflectance at Normal Incidence, JOSA. 53 (1963) 1394–1402. doi:10.1364/JOSA.53.001394.

[62]   J.E. Harvey, N. Choi, S. Schroeder, A. Duparré, Total integrated scatter from surfaces with arbitrary roughness, correlation widths, and incident angles, Opt. Eng. 51 (2012) 013402. doi:10.1117/1.OE.51.1.013402.

[63]   W.C. Oliver, G.M. Pharr, An improved technique for determining hardness and elastic modulus using load and displacement sensing indentation experiments, J. Mater. Res. 7 (1992) 1564–1583. doi:10.1557/JMR.1992.1564.

[64]   G.M. Pharr, Measurement of mechanical properties by ultra-low load indentation, Mater. Sci. Eng. A. 253 (1998) 151–159. doi:10.1016/S0921-5093(98)00724-2.

[65]   W.C. Oliver, G.M. Pharr, Measurement of hardness and elastic modulus by instrumented indentation: Advances in understanding and refinements to methodology, J. Mater. Res. 19 (2004) 3–20. doi:10.1557/jmr.2004.19.1.3.

[66]   A. Leyland, A. Matthews, On the significance of the H/E ratio in wear control: a nanocomposite coating approach to optimised tribological behaviour, Wear. 246 (2000) 1–11. doi:10.1016/S0043-1648(00)00488-9.

[67]   B.R. Braeckman, D. Depla, On the amorphous nature of sputtered thin film alloys, Acta Mater. 109 (2016) 323–329. doi:10.1016/j.actamat.2016.02.035.

[68]   A. Takeuchi, A. Inoue, Classification of Bulk Metallic Glasses by Atomic Size Difference, Heat of Mixing and Period of Constituent Elements and Its Application to Characterization of the Main Alloying Element, Mater. Trans. 46 (2005) 2817–2829. doi:10.2320/matertrans.46.2817.

[69]   D.B. Miracle, A structural model for metallic glasses, Nat. Mater. 3 (2004) 697–702. doi:10.1038/nmat1219.

[70]   D.B. Miracle, The efficient cluster packing model – An atomic structural model for metallic glasses, Acta Mater. 54 (2006) 4317–4336. doi:10.1016/j.actamat.2006.06.002.

[71]   H.W. Sheng, W.K. Luo, F.M. Alamgir, J.M. Bai, E. Ma, Atomic packing and short-to-medium-range order in metallic glasses, Nature. 439 (2006) 419–425. doi:10.1038/nature04421.

[72]   D. Ma, A.D. Stoica, X.-L. Wang, Power-law scaling and fractal nature of medium-range order in metallic glasses, Nat. Mater. 8 (2009) 30–34. doi:10.1038/nmat2340.

[73]   Y.Q. Cheng, E. Ma, Atomic-level structure and structure–property relationship in metallic glasses, Prog. Mater. Sci. 56 (2011) 379–473. doi:10.1016/j.pmatsci.2010.12.002.

[74]   G.L. Chen, X.J. Liu, X.D. Hui, H.Y. Hou, K.F. Yao, C.T. Liu, J. Wadsworth, Molecular dynamic simulations and atomic structures of amorphous materials, Appl. Phys. Lett. 88 (2006) 203115. doi:10.1063/1.2198015.

[75]   A. Hirata, Y. Hirotsu, T.G. Nieh, T. Ohkubo, N. Tanaka, Direct imaging of local atomic ordering in a Pd–Ni–P bulk metallic glass using Cs-corrected transmission electron microscopy, Ultramicroscopy. 107 (2007) 116–123. doi:10.1016/j.ultramic.2006.06.002.

[76]   X.J. Liu, Y. Xu, X. Hui, Z.P. Lu, F. Li, G.L. Chen, J. Lu, C.T. Liu, Metallic Liquids and Glasses: Atomic Order and Global Packing, Phys. Rev. Lett. 105 (2010). doi:10.1103/PhysRevLett.105.155501.

[77]   Z. Fan, P. Tsakiropoulos, P.A. Smith, A.P. Miodownik, Extension of the Hall-Petch relation to two-ductile-phase alloys, Philos. Mag. A. 67 (1993) 515–531. doi:10.1080/01418619308207175.

[78]   J. Ding, S. Patinet, M.L. Falk, Y. Cheng, E. Ma, Soft spots and their structural signature in a metallic glass, Proc. Natl. Acad. Sci. 111 (2014) 14052–14056. doi:10.1073/pnas.1412095111.

[79]   E. Ma, Tuning order in disorder, Nat. Mater. 14 (2015) 6.

[80]   K.-W. Park, J. Jang, M. Wakeda, Y. Shibutani, J.-C. Lee, Atomic packing density and its influence on the properties of Cu–Zr amorphous alloys, Scr. Mater. 57 (2007) 805–808. doi:10.1016/j.scriptamat.2007.07.019.

[81]   M. Geissler, Y. Xia, Patterning: Principles and Some New Developments, Adv. Mater. 16 (2004) 1249–1269. doi:10.1002/adma.200400835.

[82]   A.F. Lasagni, Laser interference patterning methods: Possibilities for high-throughput fabrication of periodic surface patterns, Adv. Opt. Technol. 6 (2017). doi:10.1515/aot-2017-0016.

[83]   E. Hutli, M. Nedeljkovic, A. Bonyár, Controlled modification of the surface morphology and roughness of stainless steel 316 by a high speed submerged cavitating water jet, Appl. Surf. Sci. 458 (2018) 293–304. doi:10.1016/j.apsusc.2018.07.007.

[84]   W.-Z. Qiu, H.-C. Yang, Z.-K. Xu, Dopamine-assisted co-deposition: An emerging and promising strategy for surface modification, Adv. Colloid Interface Sci. 256 (2018) 111–125. doi:10.1016/j.cis.2018.04.011.

[85]   M. Ma, R.M. Hill, Superhydrophobic surfaces, Curr. Opin. Colloid Interface Sci. 11 (2006) 193–202. doi:10.1016/j.cocis.2006.06.002.

[86]   R. Estevam-Alves, D. Günther, S. Dani, S. Eckhardt, T. Roch, C.R. Mendonca, I.N. Cestari, A.F. Lasagni, UV Direct Laser Interference Patterning of polyurethane substrates as

tool for tuning its surface wettability, Appl. Surf. Sci. 374 (2016) 222–228. doi:10.1016/j.apsusc.2015.11.119.

[87]   A. Bekmurzayeva, W.J. Duncanson, H.S. Azevedo, D. Kanayeva, Surface modification of stainless steel for biomedical applications: Revisiting a century-old material, Mater. Sci. Eng. C. (2018). doi:10.1016/j.msec.2018.08.049.

[88]   L. Müller-Meskamp, Y.H. Kim, T. Roch, S. Hofmann, R. Scholz, S. Eckardt, K. Leo, A.F. Lasagni, Efficiency Enhancement of Organic Solar Cells by Fabricating Periodic Surface Textures using Direct Laser Interference Patterning, Adv. Mater. 24 (2012) 906–910. doi:10.1002/adma.201104331.

[89]   H. Rinnert, M. Vergnat, A. Burneau, Evidence of light-emitting amorphous silicon clusters confined in a silicon oxide matrix, J. Appl. Phys. 89 (2001) 237–243. doi:10.1063/1.1330557.

[90]   W. Chamorro, J. Ghanbaja, Y. Battie, A.E. Naciri, F. Soldera, F. Mücklich, D. Horwat, Local Structure-Driven Localized Surface Plasmon Absorption and Enhanced Photoluminescence in ZnO-Au Thin Films, J. Phys. Chem. C. 120 (2016) 29405–29413. doi:10.1021/acs.jpcc.6b09974.

[91]   J.L. MacManus-Driscoll, P. Zerrer, H. Wang, H. Yang, J. Yoon, A. Fouchet, R. Yu, M.G. Blamire, Q. Jia, Strain control and spontaneous phase ordering in vertical nanocomposite heteroepitaxial thin films, Nat. Mater. 7 (2008) 314–320. doi:10.1038/nmat2124.

[92]   N. Ghafoor, L.J.S. Johnson, D.O. Klenov, J. Demeulemeester, P. Desjardins, I. Petrov, L. Hultman, M. Odén, Nanolabyrinthine ZrAlN thin films by self-organization of interwoven single-crystal cubic and hexagonal phases, APL Mater. 1 (2013) 022105. doi:10.1063/1.4818170.

[93]   Y. Wang, J. Ghanbaja, S. Bruyère, F. Soldera, D. Horwat, F. Mücklich, J.F. Pierson, Room temperature self-assembled growth of vertically aligned columnar copper oxide nanocomposite thin films on unmatched substrates, Sci. Rep. 7 (2017) 11122. doi:10.1038/s41598-017-10540-6.

[94]   R. Gago, M. Vinnichenko, A. Redondo-Cubero, Z. Czigány, L. Vázquez, Surface Morphology of Heterogeneous Nanocrystalline Rutile/Amorphous Anatase TiO_2 Films Grown

by Reactive Pulsed Magnetron Sputtering, Plasma Process. Polym. 7 (2010) 813–823. doi:10.1002/ppap.200900182.

[95]   J.F. Pierson, M. Baija, D. Horwat, Silver islands formed after air annealing of amorphous Ag–Cu–Mn–O sputtered films, J. Cryst. Growth. 311 (2009) 349–354. doi:10.1016/j.jcrysgro.2008.10.028.

[96]   A. Fillon, G. Abadias, A. Michel, C. Jaouen, P. Villechaise, Influence of Phase Transformation on Stress Evolution during Growth of Metal Thin Films on Silicon, Phys. Rev. Lett. 104 (2010). doi:10.1103/PhysRevLett.104.096101.

[97]   B. Krause, G. Abadias, A. Michel, P. Wochner, S. Ibrahimkutty, T. Baumbach, Direct Observation of the Thickness-Induced Crystallization and Stress Build-Up during Sputter-Deposition of Nanoscale Silicide Films, ACS Appl. Mater. Interfaces. 8 (2016) 34888–34895. doi:10.1021/acsami.6b12413.

[98]   E. Chason, B.W. Sheldon, L.B. Freund, J.A. Floro, S.J. Hearne, Origin of Compressive Residual Stress in Polycrystalline Thin Films, Phys. Rev. Lett. 88 (2002). doi:10.1103/PhysRevLett.88.156103.

[99]   E. Chason, A kinetic analysis of residual stress evolution in polycrystalline thin films, Thin Solid Films. 526 (2012) 1–14. doi:10.1016/j.tsf.2012.11.001.

[100]   E. Chason, J.W. Shin, S.J. Hearne, L.B. Freund, Kinetic model for dependence of thin film stress on growth rate, temperature, and microstructure, J. Appl. Phys. 111 (2012) 083520. doi:10.1063/1.4704683.

[101]   A.M. Engwall, Z. Rao, E. Chason, Origins of residual stress in thin films: Interaction between microstructure and growth kinetics, Mater. Des. 110 (2016) 616–623. doi:10.1016/j.matdes.2016.07.089.

[102]   B. Fu, G.B. Thompson, Compositional dependent thin film stress states, J. Appl. Phys. 108 (2010) 043506. doi:10.1063/1.3462431.

[103]   T.M. Kaub, P. Felfer, J.M. Cairney, G.B. Thompson, Influence of Ni Solute segregation on the intrinsic growth stresses in Cu(Ni) thin films, Scr. Mater. 113 (2016) 131–134. doi:10.1016/j.scriptamat.2015.10.010.

[104] W.D. Nix, B.M. Clemens, Crystallite coalescence: A mechanism for intrinsic tensile stresses in thin films, J. Mater. Res. 14 (1999) 3467–3473. doi:10.1557/JMR.1999.0468.

[105] R.C. Cammarata, T.M. Trimble, D.J. Srolovitz, Surface stress model for intrinsic stresses in thin films, J. Mater. Res. 15 (2000) 2468–2474. doi:10.1557/JMR.2000.0354.

[106] D. Depla, B.R. Braeckman, Quantitative correlation between intrinsic stress and microstructure of thin films, Thin Solid Films. 604 (2016) 90–93. doi:10.1016/j.tsf.2016.03.039.

[107] Z. Lu, J. Li, Correlation between average melting temperature and glass transition temperature in metallic glasses, Appl. Phys. Lett. 94 (2009) 061913. doi:10.1063/1.3081028.

[108] E. Hecht, Optics, Addison-Wesley, 2002.

[109] P.B. Barna, M. Adamik, Fundamental structure forming phenomena of polycrystalline films and the structure zone models, Thin Solid Films. 317 (1998) 27–33. doi:10.1016/S0040-6090(97)00503-8.

[110] I. Petrov, P.B. Barna, L. Hultman, J.E. Greene, Microstructural evolution during film growth, J. Vac. Sci. Technol. Vac. Surf. Films. 21 (2003) S117–S128. doi:10.1116/1.1601610.

[111] A. van der Drift, Evolutionary selection, a principle governing growth orientation in vapour-deposited layers, Philips Res Rep. 22 (1967) 267.

[112] A.N. Kolmogorov, On the statistical theory of the crystallization of metals, Bull Acad Sci USSR Math Ser. 1 (1937) 355.

[113] W.A. Johnson, R.F. Mehl, Reaction kinetics in processes of nucleation and growth, Trans Am Inst Min Eng. 135 (1939) 416.

[114] M. Avrami, Kinetics of Phase Change. I General Theory, J. Chem. Phys. 7 (1939) 1103–1112. doi:10.1063/1.1750380.

[115] M. Avrami, Kinetics of Phase Change. II Transformation-Time Relations for Random Distribution of Nuclei, J. Chem. Phys. 8 (1940) 212–224. doi:10.1063/1.1750631.

[116] M. Avrami, Granulation, Phase Change, and Microstructure Kinetics of Phase Change. III, J. Chem. Phys. 9 (1941) 177–184. doi:10.1063/1.1750872.

[117] A.T.W. Kempen, F. Sommer, E.J. Mittemeijer, Determination and interpretation of isothermal and non-isothermal transformation kinetics; the effective activation energies in

terms of nucleation and growth, J. Mater. Sci. 37 (2002) 1321–1332. doi:10.1023/A:1014556109351.

[118] E.J. Mittemeijer, F. Sommer, Solid state phase transformation kinetics: a modular transformation model, Z. Für Met. 93 (2002) 352–361. doi:10.3139/146.020352.

[119] F. Liu, F. Sommer, C. Bos, E.J. Mittemeijer, Analysis of solid state phase transformation kinetics: models and recipes, Int. Mater. Rev. 52 (2007) 193–212. doi:10.1179/174328007X160308.

[120] E.A. Jägle, E.J. Mittemeijer, The kinetics of grain-boundary nucleated phase transformations: Simulations and modelling, Acta Mater. 59 (2011) 5775–5786. doi:10.1016/j.actamat.2011.05.054.

[121] E. Vasco, C. Polop, Intrinsic Compressive Stress in Polycrystalline Films is Localized at Edges of the Grain Boundaries, Phys. Rev. Lett. 119 (2017). doi:10.1103/PhysRevLett.119.256102.

[122] T. Karabacak, J.J. Senkevich, G.-C. Wang, T.-M. Lu, Stress reduction in sputter deposited films using nanostructured compliant layers by high working-gas pressures, J. Vac. Sci. Technol. A. 23 (2005) 986–990. doi:10.1116/1.1861940.

[123] E. Citirik, T. Demirkan, T. Karabacak, Residual stress modeling of density modulated silicon thin films using finite element analysis, J. Vac. Sci. Technol. Vac. Surf. Films. 33 (2015) 021503. doi:10.1116/1.4902953.

[124] F. Klabunde, M. Löhmann, J. Bläsing, T. Drüsedau, The influence of argon pressure on the structure of sputtered molybdenum: From porous amorphous to a new type of highly textured film, J. Appl. Phys. 80 (1996) 6266–6273. doi:10.1063/1.363702.

[125] G. Gordillo, M. Grizález, L.C. Hernandez, Structural and electrical properties of DC sputtered molybdenum films, Sol. Energy Mater. Sol. Cells. 51 (1998) 327–337. doi:10.1016/S0927-0248(97)00236-5.

[126] R. Krishnan, M. Riley, S. Lee, T.-M. Lu, Formation of biaxially textured molybdenum thin films under the influence of recrystallization conditions, Thin Solid Films. 519 (2011) 5429–5432. doi:10.1016/j.tsf.2011.02.048.

[127] H.-M. Wu, S.-C. Liang, Y.-L. Lin, C.-Y. Ni, H.-Y. Bor, D.-C. Tsai, F.-S. Shieu, Structure and electrical properties of Mo back contact for Cu(In, Ga)Se$_2$ solar cells, Vacuum. 86 (2012) 1916–1919. doi:10.1016/j.vacuum.2012.04.036.

[128] L. Chen, T.-M. Lu, G.-C. Wang, Incident flux angle induced crystal texture transformation in nanostructured molybdenum films, J. Appl. Phys. 112 (2012) 024303. doi:10.1063/1.4737403.

[129] L. Chen, P. Shimpi, T.-M. Lu, G.-C. Wang, Fiber texture of sputter deposited molybdenum films and structural zone model, Mater. Chem. Phys. 145 (2014) 288–296. doi:10.1016/j.matchemphys.2014.02.010.

[130] A.M. Hofer, J. Schlacher, J. Keckes, J. Winkler, C. Mitterer, Sputtered molybdenum films: Structure and property evolution with film thickness, Vacuum. 99 (2014) 149–152. doi:10.1016/j.vacuum.2013.05.018.

[131] P. Chelvanathan, Z. Zakaria, Y. Yusoff, M. Akhtaruzzaman, M.M. Alam, M.A. Alghoul, K. Sopian, N. Amin, Annealing effect in structural and electrical properties of sputtered Mo thin film, Appl. Surf. Sci. 334 (2015) 129–137. doi:10.1016/j.apsusc.2014.08.154.

[132] J.G. Che, C.T. Chan, W.-E. Jian, T.C. Leung, Surface atomic structures, surface energies, and equilibrium crystal shape of molybdenum, Phys. Rev. B. 57 (1998) 1875–1880. doi:10.1103/PhysRevB.57.1875.